CWP-494
November 2004

An investigation of sealing and episodic pulsing of fluids at a minibasin-bounding growth fault from seismic reflection images

Matthew M. Haney

— Doctoral Thesis —
Geophysics

Defended on November 29, 2004

Committee Chair:	Prof. Bruce Trudgill
Advisor:	Prof. Roel K. Snieder
Committee members:	Prof. Kenneth L. Larner
	Prof. Paul Martin
	Prof. Jonathan Sheiman
	Prof. Terry Young

Center for Wave Phenomena
Colorado School of Mines
Golden, Colorado 80401
(1) 303 273-3557

Abstract

That faults are of fundamental importance in petroleum systems cannot be stressed enough. The role the faults play, however, is complicated by their dual nature as fluid seals and conduits. Understanding a fault's behavior demands extensive knowledge of its past geologic history, core samples, pressure measurements, and well logs. Further complicating matters, the sealing capacity of a fault usually varies directionally and the along-fault permeability episodically increases in response to slip.

Seismic reflection images offer an attractive means to measure the internal properties of fault zones remotely; for instance, direct evidence of faults (e.g., fault-plane reflections) occasionally shows up on migrated seismic data. We describe three basic models that give rise to fault-plane reflections: juxtaposition (e.g., sand/shale) contacts, effective linear-slip behavior at the fault, and large pore pressure jumps across the fault. From the point of view of fault properties, the first of these three models, juxtaposition contacts, is the least interesting. Reflectivity from a fault originating from one of the other two models directly relates to the sealing and conducting behavior of the fault. To enhance the information on the sealing and conducting properties of a fault, we propose a seismic data processing technique to attenuate the reflectivity due to juxtaposition contacts and layer boundaries. Utilizing a 2D spectral-element implementation of the elastic wave equation, we model examples and combinations of these three basic models and their imprint on reflected waves.

A 3D seismic survey from Blocks 314, 315, 330, and 331 of the South Eugene Island field, offshore Louisiana, contains reflections from a major growth fault system. We find that differences in pore pressure across a fault known as the A-fault give rise to reflections from the fault-plane. Thus, the presence of the reflections point to the fault providing a significant seal. The ability of the reflected waves to sense the sharp onsets of overpressure, or pore pressure in excess of hydrostatic, has implications for the prediction of potential drilling hazards. Along another fault known as the B-fault, we study the possibility of geologically fast, pressure-driven fluid flow along the fault. We observe the first evidence from seismic reflection images of a fluid pulse, or "fault burp", propagating up the B-fault. In reflection images from 1985 and 1992, areas of high reflectivity systematically move up the fault 1 km, for an average speed of 140m/yr. The average pulse speed can be explained with a model of a permeable fault zone connecting the shallow, normally pressured sediments to a deep, overpressured compartment. The presence of geologically fast fluid movement along growth faults sheds light on hydrocarbon migration mechanisms and the rate of reservoir recharge at South Eugene Island.

to Suzanne, my grandpa Bob, and Lela

"A musician, if he is a messenger, is like a child who hasn't been handled too many times by man, hasn't had too many fingerprints across his brain. That's why music is so much heavier than anything you ever felt."
Jimi Hendrix, to an interviewer, April 1969

"Pressure, pushing down on you, pressing down on me."
David Bowie, lyrics to *Under Pressure*, 1981

Table of Contents

Acknowledgments

First of all, I wish to thank everyone that I've crossed paths with here at the School of Mines over the past five years of graduate school and the four years of undergraduate studies before that. This place will always be home to me. To think back to when I arrived here as an 18 year-old in 1995 - I can't believe that I got to meet so many outstanding people and work with such world-class scientists.

Foremost among those world-class scientists and outstanding people is Roel Snieder. Thank you for taking me under your wing and showing me the excitement that comes with scientific discovery. Also, thanks for all those bad jokes and for actively encouraging the nasty sort of research that comprises this thesis. Working with Roel, I have begun to see how science fits into the bigger picture.

I owe a lot to Jon Sheiman for showing me the ropes at Shell and providing the environment necessary for me to do research. At times Jon says something that takes me months to figure out; he challenges me to meet him halfway. In the process, I learn more than had he just simply told me the answer. Thanks Jon for lending me your guitar whenever I came to Houston. And I would be remiss in not thanking my brother Andrew and his wife Jackie for letting me stay at their house in Houston during those trips to Shell.

I am particularly grateful to John Scales for first getting me excited about doing research when I was an undergrad. Never lose the passion you bring to everything you do. All the best goes out to Ken Larner for encouraging me to join the Center for Wave Phenomena and for leading this amazing and diverse group of researchers with such a caring hand. The same guiding touch comes from Terry over this whole tight-knit department.

Speaking of this cool group of researchers, I want to single out Huub for being a great listener and playing incredible tunes, Carlos for turning into a pro-bowler, Kasper for the excellent collaborations, Debashish for always giving me a laugh, and Justin Hedley for lightening things up at the end. And all the best to Alex, Alison, Albena, Pawan, Yaping, Greg, and Xiaoxia; it's a privilege to have been one of your colleagues.

Special thanks to the non-geophysicists on my committee, Bruce and Paul, for your interest and invaluable input into this piece of work. And Bruce, that trip to Utah changed the way I think about geophysics. I am grateful to Andrey Bakulin and Scott Wilkins at Shell for their feedback on faults. Also, thanks to Hany and Berk for the hospitality at Shell. Final thanks go out to Ronny Hofmann for guiding me through the fundamentals of rock physics, Jean-Paul Ampuero for his code and the week of instruction on how to use it, and Steven Losh for his collaboration and words of encouragement.

And most of all, thanks to Suzanne for always being there for me. This document would not exist without your emotional support. All the walks we took with Molly helped me to relax and stay sane.

Chapter 1

Introduction: faults, pore fluid pressure, and material properties

Interest in the properties of fault zones spans many different aspects of Earth science. Miners pursue economic deposits of minerals in veins that form along faults due to past fluid flow. In fact, most of the terminology associated with faults (e.g., hangingwall, footwall) originates from mining (Hickman *et al.*, 1995). Earthquake seismologists study the mechanics of failure along faults to better understand the source of their seismic signals and the danger facing large populations in seismically active areas. Petroleum geoscientists look for hydrocarbons in structural traps formed by faulting while simultaneously implicating fault zones as fluid migration pathways. Drillers attempt to avoid intersecting faults because of the uncertainties associated with their strength and fluid pressure regimes nearby. Adams & Kuhlman (1994) warn that "a connection of two or more faults via an intersecting wellbore creates a situation conducive to an underground blowout." In the petroleum industry, blowouts have caused the abandonment of several multi-million dollar wells (Hatchell, 2000). One of the most dangerous scenarios encountered while tunneling occurs when a perched water table, sealed by an impermeable fault, is breached (Domenico & Schwartz, 1990).

With all this talk of how important and pervasive faults are, it is fair to ask "what makes fault zones unique?". Besides the fact that seismicity originates at faults and that faults are usually associated with a high heat flux, one of the hallmarks of faults is how they interact with fluids. Flow tests conducted in fault zones reveal that, because of high fracturing, the permeability of fault rock varies strongly as a function of pore pressure (Anderson *et al.*, 1995; Fisher *et al.*, 1996). This leads to a nonlinear fluid flow equation (Rice, 1992) that I discuss in the final chapter of this thesis. Faults also show evidence for anisotropic permeability (Zhang & Tullis, 1998) by virtue of their split personality as both lateral fluid seals and vertical conduits. Moreover, there appears to be a generic permeability structure associated with faults: a central cataclastic zone, or fault gouge layer, surrounded by a damage, or process, zone (Scholz & Anders, 1994). Contact forces along faults, which are responsible for the formation of cataclasite, can mechanically undo the rock compaction process by crushing the rocks into a powder. As a result, thin layers, known as deformation bands that are virtually impermeable, sometimes form near faults. Deformation bands serve to compartmentalize a reservoir, forcing the need for precise placement of multiple producing wells to efficiently tap the hydrocarbons that are present. At the least, deformation bands act as baffles and severely hinder fluid flow.

Seeing how faults distinguish themselves, I decided the title of my thesis should emphasize the role of fluids and settled on, “An investigation of sealing and episodic pulsing of fluids at a minibasin-bounding growth fault from seismic reflection images.” I have chosen to describe the thesis as an investigation after seeing a presentation by Malcolm Sambridge of ANU during the summer of 2004. In it, he quipped that every scientific endeavor has a bit of Sherlock Holmes in it. Looking back at my research on faults, I get the feeling that it has been a bit of an interrogation of the subject. From the title, there is also a hint of the dual behavior of faults as seals and, occasionally, significant fluid conduits. The specific type of fault that I study is prominently mentioned. This is done since there are as many types of faults as there are rocks in the subsurface. Needham & Yielding (1996) and Yielding *et al.* (1991) have demonstrated that there exists an inverse power-law scaling between the number and size of faults, with the spatial range extending from small fractures all the way to large, plate-boundary faults. The faults discussed in this thesis fall well between these two extremes. Finally, the tool I use to draw information about the faults comes from seismic reflection images.

The thesis is organized with technical chapters coming first and interpretation chapters at the end.

1. Introduction: faults, pore fluid pressure, and material properties
2. Seismic data processing in the stationary phase approximation
3. Finite element modeling of slip-discontinuities in layered media
4. Spectral element modeling of fault-plane reflections
5. Fault-plane reflections as a diagnostic of pressure differences in reservoirs: a case study
6. Seismic detection of a spatially-limited fluid pulse ascending a growth fault

In Chapter 2, I analyze the entire “standard” seismic data processing sequence using the stationary phase approximation. Though state-of-the-art seismic data processing no longer relies on such an approximation, a thorough knowledge of the subject is a must for quantitative interpreters of seismic data. In particular, the nature of the errors in seismic reflection images has an impact on subsequent interpretations of fault-plane reflections.

In Chapter 3, I present the nuts and bolts of a finite element implementation of the elastic wave equation in a layered medium. The exercise is instructive, especially in the 1D setting where the complicating aspects of meshing and assembly of the mass and stiffness matrices are unnecessary. The concepts introduced in this section directly pertain to the following section on spectral elements. In addition, a wave propagation code has come out of this research that should be a useful tool for others involved in seismic related research. For my own purposes, I use the code to do simple modeling of well logs in later chapters of this thesis.

In Chapter 4, I model the full elastic wavefield via the spectral-element method and process the simulated data to construct images. With this tool, I primarily focus on fault-plane reflections and the underlying causes of seismic reflectivity at faults. I find that fault-related pore-pressure contrasts above a certain threshold can be detected in the presence of reflections from bed terminations at the fault. I also use empirical relationships between elastic properties (e.g., density, P-wave velocity) and pore pressure to relate a slipping fault to a pressurized fault zone.

In Chapter 5, I interpret fault-plane reflections from a large, minibasin-bounding growth fault at the South Eugene Island field. A dip-filter processing scheme acts to highlight fault-plane reflections in seismic data obtained in a line shot in the direction of a system of growth faults. I find that over large portions of the fault, the fault-plane reflections arise from contrasts in pore pressure across the fault.

In Chapter 6, I extend the work begun in Chapter 5 and push the methodology into a study of fault-hosted vertical fluid flow at the South Eugene Island field. Fluid flow along faults is a poorly understood topic that sits at the crossroads of many fields of geoscience. I begin by describing an unusually high-amplitude fault-plane reflection that, from well data taken at South Eugene Island, correlates with a portion of a growth fault where other scientists had previously speculated about the possibility of a fluid pulse ascending the fault. By comparing 1985 and 1992 data, I observe that areas of high reflectivity at the B-fault move systematically up the fault plane 1 km, for an average speed of 140 m/yr.

Finally, after the discussion on fault burps, I make conclusions about the main outcomes of my research on faults and future paths to take. During the course of my thesis work, I also had time to do research in the field of incoherent multiple wave scattering (Haney *et al.*, 2003a; Van Wijk *et al.*, 2004; Haney *et al.*, 2005). Though unrelated to the topic of fault zones, the projects on multiple wave scattering taught me how to do scientific research in general. In addition, I produced two original pieces of research in exploration magnetics (Haney & Li, 2002; Haney *et al.*, 2003b) and contributed to another (Li *et al.*, 2004).

In this introductory section, I discuss empirical relationships between pore pressure and three basic rock properties - porosity, density, and sonic velocity. The data for this analysis come from wells drilled at the South Eugene Island field, offshore Louisiana. The fact that pore pressure largely controls rock matrix properties in compacting sedimentary basins allows methods for imaging seismic reflections to indirectly measure spatially varying pore pressure distributions. I use the evidence presented in this chapter as a springboard to do precisely that with seismic data taken at the South Eugene Island field. The variation of the three rock properties with effective stress reveals a fundamental hysteretic type of behavior in the sediments. Evidence for both plastic (irreversible) and elastic (reversible) deformation exists in the available well data and pressure tests. These two regimes point to different underlying causes of overpressure (Hart *et al.*, 1995). For these dual deformation mechanisms, I construct two empirical relationships between each rock property and pore pressure - one valid for each regime. Before I begin, I would like to cite Ronny Hofmann of the Center for Rock Abuse at the Colorado School of Mines for his help and patience in enhancing my understanding of overpressure mechanisms. The work in this chapter was done in collaboration with him.

1.1 Vertical effective stress

Pore pressures that exceed the hydrostatic pressure, or overpressures, lead to a lowering of density and seismic velocity and, as discussed in Chapters 5 and 6, significantly contribute to the reflectivity of faults. Pennebaker (1968) was among the first geoscientists to demonstrate the ability of seismic stacking velocities to detect fluid pressures in the subsurface. Terzaghi (1943), however, had previously discussed the basic principle, that of an effective stress acting on the rock frame. According to his principle, it is the effective stress that determines rock properties, in particular sonic velocity. Terzaghi denoted the effective stress as the difference between the confining stress, σ_v, and the pore pressure p:

$$\sigma_d = \sigma_v - p. \tag{1.1}$$

The subscript v stands for *vertical* since, in extensional regimes, the maximum stress is in the vertical direction (the weight of the overburden). The quantity σ_d is also called the differential stress. Equation (1.1) states that rocks of similar composition but at different confining stress and pore pressure have the same velocity so long as the difference between the confining stress and pore pressure is the same. Hence, high pore pressure, which lowers effective stress, leads to lower seismic velocities. The work in this thesis draws heavily upon Terzaghi's principle to relate the seismic signatures of fault zones to local pore-pressure variations at the fault.

Following the work of Terzaghi, rock physicists began to postulate that the effective stress governing rock properties is not simply the difference between the confining stress and the pore pressure (Wang, 2000a). Today, the most general effective-stress law is instead

$$\sigma_e = \sigma_v - np, \tag{1.2}$$

where the parameter n is called the *effective stress coefficient.* Carcione & Tinivella (2001) state that the value of n can differ for each physical quantity (e.g., permeability, compressibility, or shear modulus), and that it depends linearly on the differential stress of equation (1.1). Currently, the effective-stress coefficient is a controversial topic that is still being sorted out by the rock physics community. For the remainder of this thesis, we do not distinguish between differential stress, σ_d, and effective stress, σ_e; that is, we take $n = 1$ in equation (1.2).

1.2 Porosity versus depth

As suggested by its name, compaction acts to reduce the porosity of sediments as they are buried; however, this process can continue only as long as fluids in the diminishing pore space are allowed to be expelled. Such would be the case in normal pressured, hydrostatic sediments in which the fluids are in communication up to the seafloor. Once the movement of the fluids out of the pore space is opposed, as in a compartment sealed-off by low permeability or high capillary-entry-pressure shales or fault gouge, the porosity remains constant with burial depth if the fluid is more or less incompressible. This situation is called *under-*

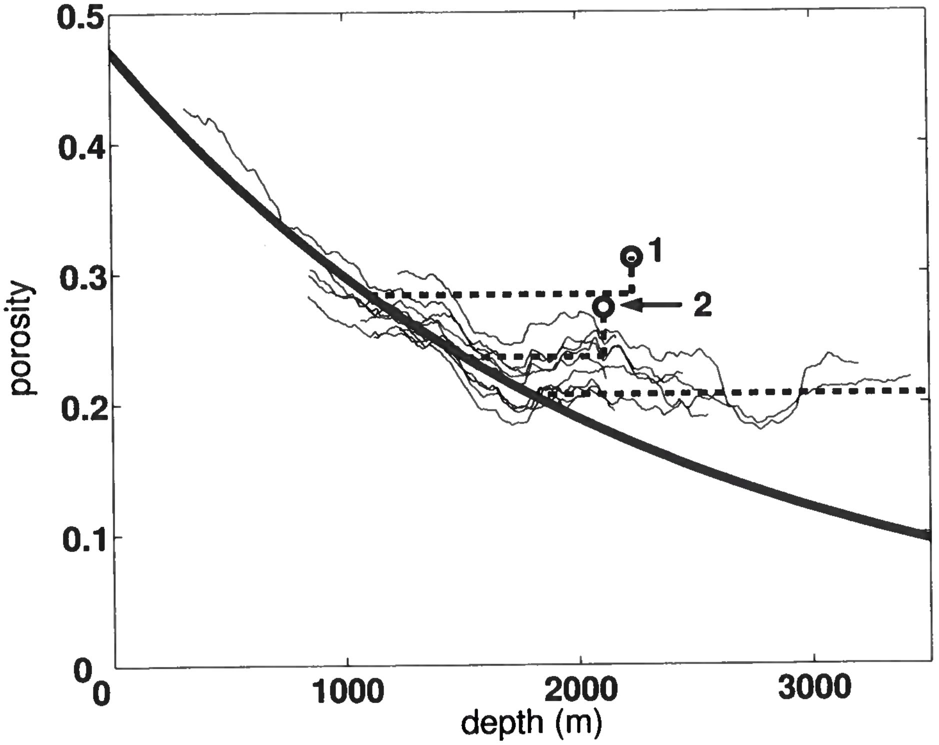

Figure 1.1. Porosity versus depth at South Eugene Island. The thick, solid line is the best-fit normal compaction trend using Athy's Law (Athy, 1930). The faint solid lines are density-derived porosity values from 11 wells at South Eugene Island. To obtain the porosity, we assume that the solid grains have a density of 2650 kg/m^3 and the fluid has a density of 1000 kg/m^3, as in Revil & Cathles (2002). There is a clear break from the shallow, exponentially decreasing porosity trend at a depth of 1800 m, at which point the porosity remains constant with increasing depth, as shown by the flat dashed line. The two circles are density-derived porosities from the upthrown block to the north of the minibasin at South Eugene Island. The dashed lines connecting the circles to the main compaction trend are the interpreted porosity histories of the samples. They show a period of undercompaction, depicted as a horizontal line deviating from the normal compaction trend, followed by a vertical unloading path due to a late-stage pore-pressure increase.

compaction (Huffman, 2002). Undercompaction means the sediments are "frozen" in time and are simply buried in their unchanging earlier compaction state (Bowers, 1995). To compound the situation, if fluid from outside the undercompacted sediments is pumped into the pore space, or if hydrocarbons are generated from within the undercompacted sediments, a process called *unloading* occurs (Huffman, 2002). Whereas undercompaction can only cease the reduction of porosity (Bowers, 1995), unloading can actually reverse the trend and increase porosity. Although unloading can reverse the trend, it cannot reclaim all of the previously lost porosity. This is because the compaction process has a large *irreversible* component. In contrast, unloading and loading of sediments by pumping fluid into and then depressurizing the pore space is a reversible process, insofar as the fluid does not cause hydrofracturing.

We have studied wireline data taken in wells at the South Eugene Island field, offshore Louisiana, for indicators of overpressure, such as constant porosity as a function of depth. Previous work by Hart *et al.* (1995) shows the crossover from hydrostatic to overpressured conditions in porosities derived from sonic velocities. We take a slightly different, more straightforward approach here based on the density log. The South Eugene Island field is a Plio-Pleistocene minibasin formed by salt withdrawal and has yielded more than 300 million barrels of oil in its lifetime. A cartoon depiction of the subsurface at South Eugene Island is displayed in Figure 1.2. The main part of the field is a vertical stack of interbedded sand and mostly shale layers bounded by two large growth faults to the north and south. In Chapters 5 and 6, we discuss 3D seismic data volumes acquired at South Eugene Island in 1985, 1988, and 1992.

Figure 1.1 shows porosity derived from density logs taken in the following wells: A13, A20ST, A14OH, A15, A23, A6, B10, B1, B2, B7, and B8. Because the geology in the minibasin is essentially horizontally layered, we ignore the fact that some wells may be miles away from each other and simply look at the depth variation of their porosity. In all the well logs shown in this chapter, we have done significant smoothing with depth to remove any short-range lithologic influences (e.g., sand versus shale) on the density and velocity. To obtain the porosity from the density log, we take the solid grains to have a density of 2650 kg/m^3 and the fluid to have a density of 1000 kg/m^3, as in Revil & Cathles (2002). There is a clear break from the shallow, decreasing porosity trend at a depth of 1800 m. Based on the work of Stump *et al.* (1998), we assume that this is the onset of overpressures in the sedimentary section, beneath a shale bed located above a layer called the JD-sand. We fit an exponential trend to the porosity values above 1800 m, known as Athy's Law (Athy, 1930), to get the normal compaction trend in the hydrostatically pressured sediments

$$\phi^c(z) = 0.47\ e^{-0.00046\ z}, \tag{1.3}$$

where, in this equation, the depth z is in meters. The superscript c in equation (1.3) refers to the fact that this functional relationship characterizes normal compaction. In the porosity-versus-depth plot of Figure 1.1, this relationship holds for any movement towards the right on the normal compaction curve and any purely right-going horizontal deviations from the normal compaction curve. For purely right-going horizontal deviations, the depth z used in equation (1.3) is equal to the depth at which the horizontal deviation started.

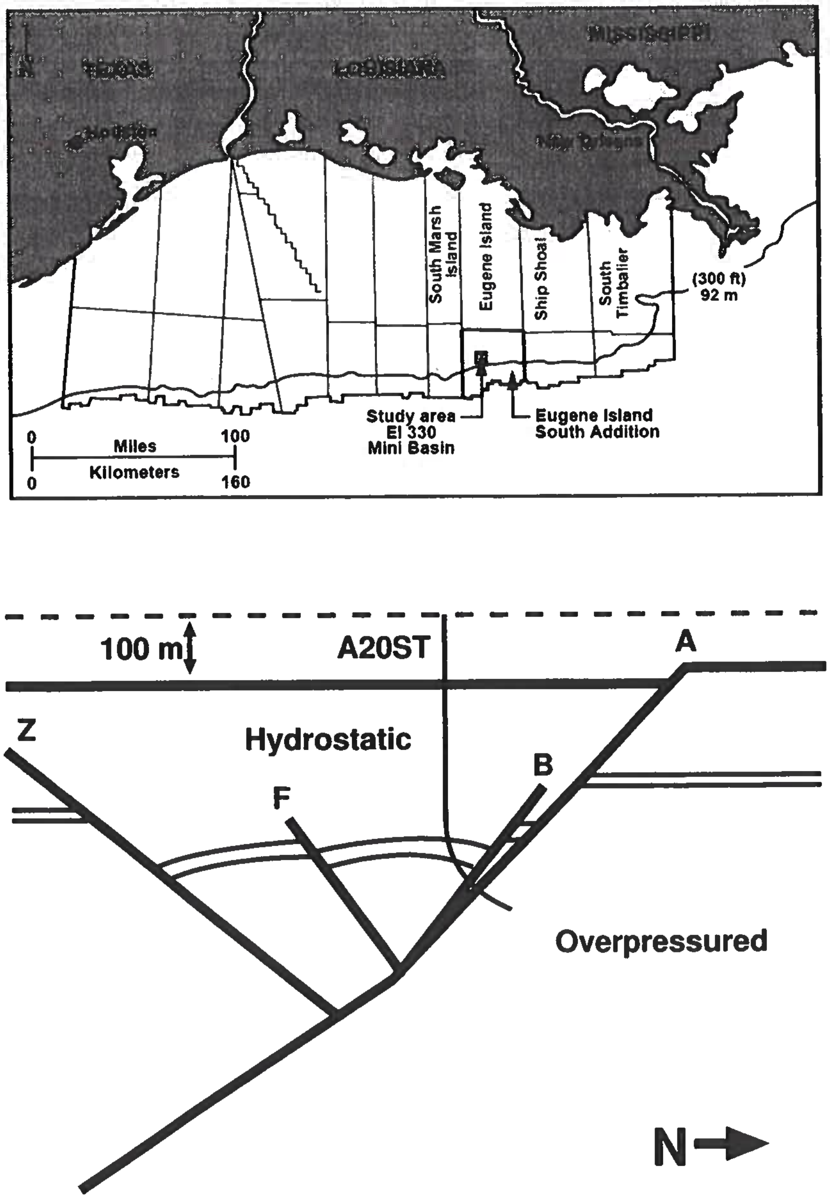

Figure 1.2. Regional map (top), from Anderson *et al.* (1995), and cartoon depth section (bottom) of the subsurface at South Eugene Island. The four main faults discussed in this thesis are shown in the bottom panel as the A, B, F, and Z faults. Throw across the faults is depicted by the layer running from left to right. Most of the wells at South Eugene Island were drilled into the shallow, hydrostatic section; the A20ST well was unusual in that it was continued through the A-fault system and into the deep overpressured compartment.

The two circles in Figure 1.1, represent samples taken in the A20ST well and are connected to the normal compaction curve by both horizontal and vertical lines. The vertical lines show the departure of the samples from the normal compaction trend. I return to these in the next section.

The sediments deeper than 1800 m in Figure 1.1 maintain a nearly constant porosity of around 0.2 during subsequent burial (a horizontal deviation from the compaction trend). Though the depth of the sediments increases with burial, the effective stress experienced by the sediments does not seem to change. Hence, the additional weight of the overburden with increasing depth is borne by the fluids trapped in the pore space. As a result, the pore pressure increases with the vertical gradient of the overburden stress and is said to have a *lithostatic gradient.* This point is illustrated graphically in Figure 1.3. In this plot, we make the crude approximation that the lithostatic gradient (or total weight density), ρg, is twice as large as the hydrostatic gradient (or fluid weight density), $\rho_f g$, with g the acceleration of gravity. Since $\rho g = 2\rho_f g$, the effective stress is equal to the hydrostatic stress down to 1800 m. At that point, the effective stress stays constant with depth due to undercompaction; therefore, the pore pressure must increase at the rate of the lithostatic stress in order to satisfy Terzaghi's law, equation (1.1). In doing so, overpressure, or pore pressure in excess of hydrostatic, is created below 1800 m.

1.3 Density versus vertical effective stress

Since density is a parameter widely used in the field of seismic wave propagation, we study the variability of the bulk density in this section. By looking at bulk density, we also avoid the assumption concerning the solid and fluid densities needed to obtain the porosity. In contrast to the preceding section, we want to see how density changes with effective stress, instead of depth. To accomplish this, we take only the measurements that are shallower than 1800 m, where the pore pressure is, by all indications, hydrostatic. Therefore we know the pore pressure and can calculate the effective stress. In overpressured compartments, since the pore pressure is unknown, direct measurements by Repeat Formation Tests (RFTs) are necessary to calculate the effective stress.

We rewrite equation (1.3) in terms of density and effective stress using the relationships

$$\rho = \rho_s(1-\phi) + \phi\rho_f, \tag{1.4}$$

and

$$\sigma_d = \rho_f g z, \tag{1.5}$$

where ρ is the bulk density and ρ_s and ρ_f are the densities of the solid and fluid components. Note that the relationship for σ_d holds only under hydrostatic conditions. From these relationships and equation (1.3), we obtain the normal compaction curve for density

$$\rho^c(\sigma_d) = \rho_s - 0.47\ (\rho_s - \rho_f)\ e^{-0.0003\sigma_d}, \tag{1.6}$$

where ρ_s and ρ_f are the densities of the solid and fluid components, taken as 2650 kg/m^3

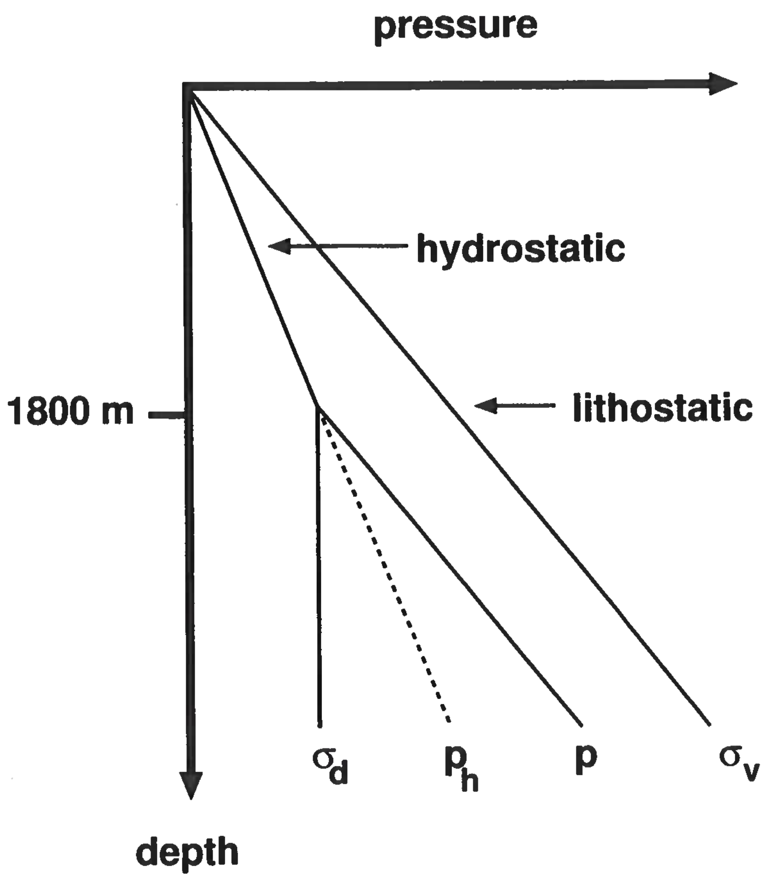

Figure 1.3. A depth section of the pressure regime for pure undercompaction. The symbols are as follows: σ_d is the effective stress, P_h is the hydrostatic pressure, P is the pore pressure, and σ_v is the overburden, or lithostatic, stress. Note that, before 1800 m, the effective stress stays constant, as seen from the porosity versus-depth-plot in Figure 1.1, and the pore pressure increases at a rate equal to that of the overburden stress.

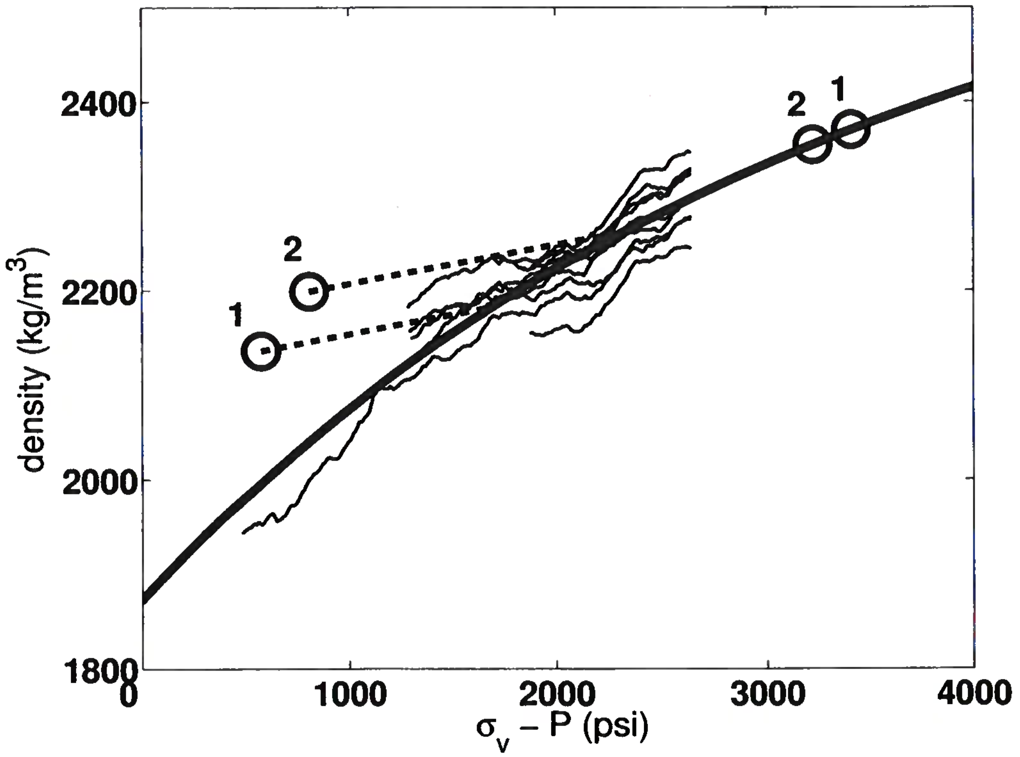

Figure 1.4. Density versus effective stress at South Eugene Island. The thick solid line is the same normal compaction trend shown in Figure 1.1, except transformed into density and effective stress. The faint solid lines are also the same as in Figure 1.1, except that they are now limited to the hydrostatic depths down to 1800 m. The circles represent two pressure measurements, labeled 1 and 2, which were made in the overpressured upthrown block where a density log also existed. For each pressure measurement, we plot the data point twice - one where it should lie on the normal compaction curve were it to have been normally pressured, and the other where it actually does plot because of severe overpressure. Note that sample 1 is from a greater depth than sample 2.

and 1000 kg/m^3 respectively, and σ_d is in psi. We plot this normal compaction curve in Figure 1.4 together with the density measurements. Also, in Figure 1.4, we show as circles two data points obtained from RFT pressure measurements and density log measurements in the overpressured upthrown block. We show the circles in two locations - one on the normal compaction trend where they would plot if the measurements were at hydrostatically pressured locations, and the other where they actually plot because of severe overpressures being present in the upthrown block.

At this point, we don't know exactly how the samples taken in the upthrown block came to be off the normal compaction trend. Using a laboratory measurement of the unloading coefficient by Elliott (1999) on a core sample taken near the locations of samples 1 and 2, the path that these samples took to their present locations can be estimated. Elliott (1999) characterized the unloading, or elastic swelling, for the porosity of the core samples to be

$$\phi^u(\sigma_d) = \phi_0 \left(1 - \beta\sigma_d\right), \tag{1.7}$$

where ϕ_0 and β characterize the deviation of the unloading path from the normal compaction trend. Note the superscript u, in contrast to equation (1.3), indicating the unloading path instead of the normal compaction trend. Elliott (1999) found that $\phi_0 = 0.37$ and $\beta = 0.98 \times 10^{-8}$ Pa^{-1} for the unloading path. Though these parameters describe the porosity, we use them to find the slope of the unloading path for density using the relationships between porosity and density described earlier. After finding this slope, we can construct the unloading path for the density from equation (1.6) and the slope

$$\rho^u(\sigma_d) = 0.04\ (\sigma_d - \sigma_{max}) + \rho_s - 0.47\ (\rho_s - \rho_f)\ e^{-0.0003\sigma_{max}}. \tag{1.8}$$

This expression contains an extra parameter σ_{max} that refers to the value of the effective stress when the sample began to be unloaded. We do not know σ_{max} for samples 1 and 2, but we do know that σ_{max} must lie on the main compaction trend. Hence, we can construct linear unloading paths for the density, as shown by the dashed lines in Figure 1.4. With these unloading paths, we can then find the value for the maximum past effective stress σ_{max}. It is worth mentioning that the maximum past effective stress for sample 1 comes out to be $\sim$ 1500 psi by our approach of using Elliott's experimental results. In an independent measurement, Stump & Flemings (2002) performed uniaxial strain tests on a core sample taken from the same location as sample 1 to find the maximum past effective stress. Stump & Flemings (2002) report a value of 1248 psi for this sample, close to our estimate of $\sim$ 1500 psi; visually, the discrepancy lies within the error bars of the normal compaction curve's fit to the density log data.

With the estimate of the maximum past effective stress, we can also return to Figure 1.1 and find the depth at which samples 1 and 2 left the normal compaction trend, since in the hydrostatic zone the depth is a linearly scaled version of the effective stress. These depths correspond to a slightly lower porosity than that of samples 1 and 2. We interpret this as being the result of a late stage porosity increase and represent it as a vertical unloading path for samples 1 and 2 in Figure 1.1.

1.4 Sonic velocity versus vertical effective stress

For the purposes of modeling faults and to make inferences about the distribution of pore pressure from seismic interval velocity inversions, accurate pore-pressure-versus-velocity relationships are critical Dutta (1997). In general, sonic velocity has a normal compaction curve and unloading paths as a function of effective stress that are similar to those we just described for the density well log data. To obtain these relationships, we proceed as for the density logs: 1) We take 12 shallow wells to make up a data set of sonic velocity versus effective stress. 2) We select the depth range with hydrostatic pressures and plot the sonic velocity versus effective stress. 3) We fit this with a power law relation for the normal compaction trend. 4) We then look at where the two samples from the overpressured upthrown block lie and construct unloading curves using the estimate for the maximum past effective stress that we obtained in the previous section on density. The wells we use for characterizing the sonic velocity come from A20ST, A14OH, A23, A6, B10, B1, B2, B7, B8, A1, B14, and B20.

In Figure 1.5, we plot the normal compaction trend for sonic velocity as a thick solid line described by the power law equation (Bowers, 1995)

$$v_p^c(\sigma_d) = 1500 + 2.3\ \sigma_d^{0.77}, \tag{1.9}$$

where v_p is in m/s and σ_d is in psi. Note again the superscript c for the normal compaction relation. We also construct the unloading curve for v_p following the relationship first suggested by Bowers (1995)

$$v_p^u(\sigma_d) = 1500 + 2.3\ \left[\sigma_{max}\left(\frac{\sigma_d}{\sigma_{max}}\right)^{1/6.2}\right]^{0.77}, \tag{1.10}$$

where σ_d and σ_{max} are in psi and v_p is again in m/s.

To model elastic waves, one other parameter is needed in addition to ρ and V_P; for instance, a seismologist would naturally want the shear velocity. In the absence of information on the shear wave velocity v_s and pressure in the shallow, hydrostatic sediments, we assume that

$$v_s(\sigma_d) = v_p(\sigma_d) - 1500, \tag{1.11}$$

where this relationship holds on both the normal compaction curve and the unloading path. The data presented by Zimmer *et al.* (2002) for unconsolidated sands supports this assumption, in that the dependence they found for v_s on effective stress is essentially a down-shifted version of the v_p curve. An additional piece of supporting evidence comes from the only v_s data available at South Eugene Island, a shear log from the A20ST well, where samples 1 and 2 were taken. There, the ratio of v_p/v_s from the sonic and shear logs falls between 3 to 3.5 in the overpressured upthrown block. Inserting the values for v_p at samples 1 and 2 into equation (1.11) to get v_s and finding the corresponding ratio of v_p/v_s, we get $v_p/v_s = 3.48$ at sample 1 and $v_p/v_s = 2.96$ at sample 2, within the range of the ratios observed in the sonic and shear logs.

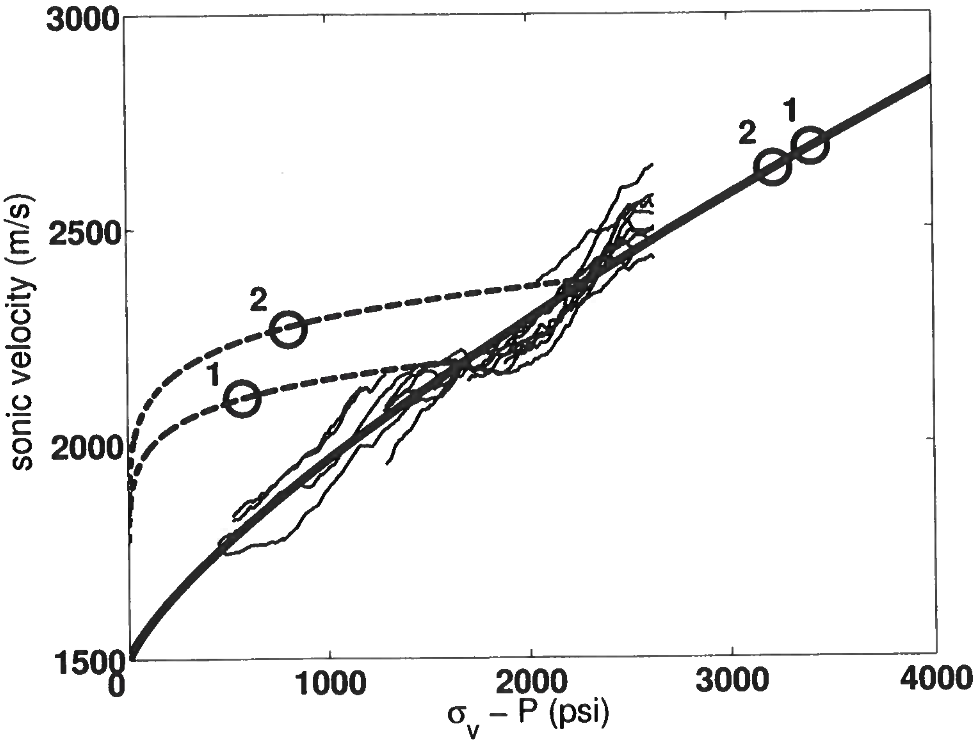

Figure 1.5. Sonic velocity versus effective stress at South Eugene Island. The thick solid line represents the normal compaction curve fitted to the shallow well data, shown in the faint solid lines. We also plot samples 1 and 2 both where they should fall on the normal compaction trend, were they to be normally pressured, and where they actually plot due to the severe overpressure where they were obtained. Using the estimate for past maximum effective stress from the density plot and the Bowers-type relation (Bowers, 1995) shown in equation (1.10), we are able to construct the velocity unloading curves, shown as dashed lines.

1.5 Discussion

We have established two empirical relationships between each of three basic rock properties and pore pressure at the South Eugene Island field. Most important for subsequent numerical modeling of wave propagation, we have found relationships for the density ρ and the sonic velocity v_p on both the normal compaction and unloading paths. Without shallow information on the shear velocity v_s, we must make the assumption that it is a down-shifted version of the $v_p(\sigma_d)$ relationship. From looking at the density-derived porosity-versus-depth-relationship, we are able to conclude that the deep, overpressured sediments below the JD-sand are predominately overpressured because of compaction disequilibrium, since their porosity did not change appreciably with depth. In contrast, both compaction disequilibrium and unloading have contributed to the current overpressured state of the sediments on the upthrown side. The latter conclusion is in agreement with a previous study by Hart *et al.* (1995) on porosity and pressure at South Eugene Island.

Chapter 2

Seismic data processing in the stationary phase approximation

2.1 Summary

To gain insight into the pitfalls involved in interpreting, for instance, amplitudes on post-stack time-migrated data, we describe a simple theory for gauging the amplitude and phase errors in the complete seismic data processing sequence resulting from stacking and migration velocity errors. Here, following Black *et al.* (1993), we take the standard sequence to be: 1) geometrical spreading correction, 2) normal-moveout correction (NMO), 3) dip moveout correction (DMO), and 4) zero-offset migration of stacked data. This is essentially the sequence followed in the processing of the South Eugene Island data that are analyzed in Chapters 5 and 6. After first deriving the amplitude and phase response of stacking to errors in stacking velocity for the case of a horizontal reflector, we numerically model post-stack time-migrated waveforms with stacking and migration errors using the spectral element method (SEM) to generate synthetic seismograms over a simple normal fault model. The SEM modeling code is presented and discussed fully in Chapter 4. We apply the theoretical results for amplitude and phase errors to study reflections from horizontal layers and then examine the changes in fault-plane reflectivity due to incorrect stacking velocities. We observe that the fault-plane reflections are relatively less sensitive to the presence of stacking velocity errors than are the associated layer reflections. Having completed the analysis for the stack response, we turn to the zero-offset migration response. With the same approach as for stacking, we are able to confirm the various correction factors that must be applied to the result of simple diffraction summation in order to recover the original waveform. We finish this chapter by examining the more complicated DMO response and derive the correction factors necessary for a diffraction summation type of DMO. From analysis of the DMO response, we are able to generalize the previous result for the stacking response in the presence of dipping layers, such as fault-plane reflections.[1]

2.2 Introduction

An understanding of the filtering action of stacking is necessary to gauge the reliability of amplitudes and phases in a post-stack time-migrated image. Haney *et al.* (2004) have

---

[1] Accepted as a technical comment in *First Break*, 2005

shown that the amplitudes of post-stack time-migrated fault-plane reflections qualitatively correspond to a section of a growth fault in the Gulf of Mexico that seals (see also Chapter 5). Furthermore, in Chapter 6, we demonstrate that a strongly reflecting section of a growth fault in the same minibasin (South Eugene Island Block 330) coincides with a the location of a postulated fluid pulse caught in the act of ascending the fault (Losh *et al.*, 1999; Revil & Cathles, 2002). The most significant source of error in the amplitudes and phases of these post-stack time-migrated images, besides the neglect of ray-bending and anisotropy, likely arises from mis-stacking. Errors in the migration velocities should mainly result in mis-positioning of the reflections. This problem is ameliorated the data examples in Chapters 5 and 6 by the use of a dip-filter that locally searches for the maximum coherence direction before filtering and manual picking of the fault-plane reflections, whether these lie at the correct spatial position (bed terminations) or not. In the first section of this chapter, we examine the errors due to incorrect stacking velocities. The same array-theory-based methods we use to study the amplitude degradation and phase shifts caused by mis-stacking are applied in later sections of this chapter to find the degradation attributable to errors in migration velocities and the response of zero-offset migration and DMO. Before starting, thanks go out to Jon Sheiman for sparking interest in this subject, Roel Snieder for making the connection between the array-based approach and the method of stationary phase, and Xiaoxia Xu for her copy of Lu (1993), which got the research started in the right direction.

2.3 The stack response

In a recent technical article in *First Break*, Gausland (2004) made the case that the result of stacking is not limited to the often quoted factor of $1/\sqrt{n}$ reduction in noise where n is the fold of a CMP-gather. Through his figures and illustrations, Gausland showed that stacking also acts as a frequency and wavenumber filter. Although the intentions of the article were not to, as Gausland put it, "give methods or formulae" and that a "simplified analysis can be made using simulation" instead of mathematics, we could not help but see a connection between his main points and the method of stationary phase (Born & Wolf, 1980). In this comment, we give an interpretation of Gausland's results within the language of stationary phase. All of Gausland's conclusions are supported by the stationary phase analysis, save for some details concerning the time-delay induced by mis-stacking. In addition, we find other factors affecting the stacking response that were not pointed out by Gausland. The issues on fold versus spreadlength brought up by Gausland cannot be addressed explicitly within the stationary phase analysis; we return to them at the end of this section. Arguments based on stationary phase have been used extensively in the literature on imaging and migration (Bleistein *et al.*, 2001). Hence, a result of this mathematical excursion is a clear connection between stacking and migration, which Gausland alluded to briefly when he stated that "a further analysis of the similarities between ... stacking and migration is necessary for a full understanding of these important aspects of seismic data processing ...". This connection is further developed in the later sections of this chapter on zero-offset migration and DMO.

Suppose that in a CMP-gather there is a single event, with a zero-offset waveform

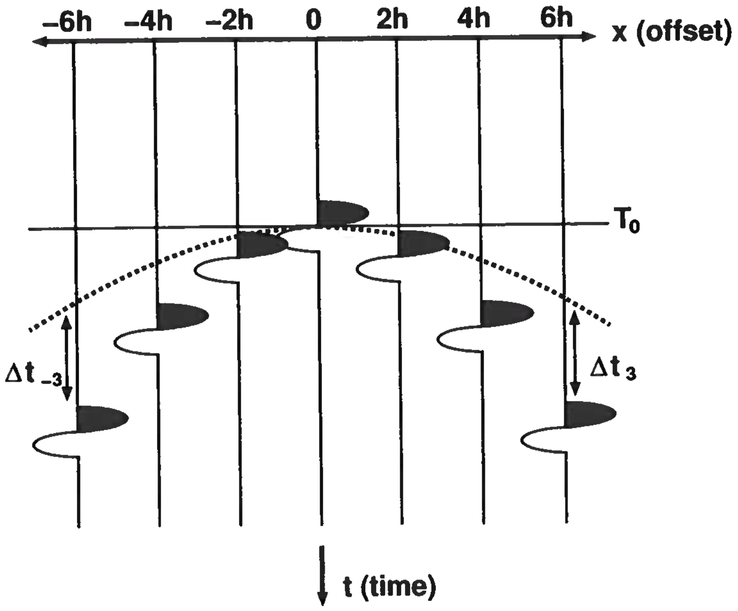

Figure 2.1. A CMP-gather containing an event at zero-offset two-way-time T_0. The horizontal axis is offset, with h representing the half-offset spacing. The event is mis-stacked because the moveout curve uses too high a stacking velocity, shown as a dashed line. The mis-stacking induces a time shift between the moveout curve and the event, Δt.

$f(t)$ at zero-offset two-way-time T_0, that has hyperbolic moveout with NMO-velocity v and a wavelet that does not change with offset (see Figure 2.1). The event is stacked with a hyperbola whose apex is at T_0 using a stacking velocity v_{st} not necessarily equal to v. When v_{st} does not equal v, a time shift Δt_k occurs at the k-th offset trace before stacking. Hence, the normalized stacking response, neglecting NMO-stretch, is

$$\begin{aligned} g(t) &= \frac{1}{2n+1}\left[f(t-\Delta t_{-n})+\cdots+f(t-\Delta t_{-1})+\right. \\ &\quad \left. f(t)+f(t-\Delta t_1)+\cdots+f(t-\Delta t_n)\right], \end{aligned} \tag{2.1}$$

where $2n+1$ is the total number of traces in the CMP-gather. In equation (2.1), we have included a trace at zero offset, though this would not occur in practice. We have also assumed that the traces have been corrected for geometrical spreading. For hyperbolic moveout and hyperbolic stacking, the time delays are (Yilmaz, 1987)

$$\Delta t_k = \sqrt{T_0^2 + \frac{4k^2h^2}{v^2} - \frac{4k^2h^2}{v_{st}^2}} - T_0, \tag{2.2}$$

where h is the half-offset spacing (assumed to be regular) and the subscript k represents the k-th trace from zero-offset (see Figure 2.1). Note that the time delays vanish when $v_{st} = v$ (perfect stacking). Denoting the Fourier transforms of $f(t)$ and $g(t)$ as $F(\omega)$ and $G(\omega)$, the transform of equation (2.1) may be written

$$G(\omega) = F(\omega)K(\omega), \tag{2.3}$$

where the transfer function, K, is

$$K(\omega) = \frac{1}{2n+1}\sum_{k=-n}^{n} e^{i\omega\Delta t_k}. \tag{2.4}$$

At this point, since we are in the frequency domain, NMO-stretch could be included as an amplitude and dilation factors in the exponentials in the series (Yilmaz, 1987); however, in the interest of simplicity, we do not account for it here. For the particular case of linear moveout ($T_0 = 0$), the series in equation (2.4) is a geometric series and can be evaluated exactly (Lu, 1993). This case is presented in chapter 4 in the section on dip-filtering. The reference to a "familiar array equation" by Gausland (2004) comes from this geometric series approach. The series is geometric because the respective time delays are regularly spaced ($\Delta t_k = k\Delta t_1$). When the moveout is nonlinear, for instance hyperbolic, the time delays are not regularly spaced and the series in equation (2.4) cannot be evaluated exactly. To obtain his results, Gausland (2004) chose some values for T_0, n, ω, h, and v and numerically calculated $K(\omega)$ with equation (2.4).

We proceed by approximating equation (2.4) with an integral and evaluating it by the method of stationary phase (Born & Wolf, 1980; Bleistein *et al.*, 2001). First, note that the fold of the CMP-gather, $2n+1$, is related to the spreadlength, L_s, and the half-offset spacing, h

$$2n+1=\frac{L_s+h}{h}. \tag{2.5}$$

Using the definition from equation (2.5), the finite series of equation (2.4) may be rewritten as

$$K(\omega)=\frac{1}{L_s+h}\sum_{k=-n}^{n} e^{i\omega\Delta t_k}h. \tag{2.6}$$

The finite series in equation (2.6) looks like a discretized integral (Riemann sum) over offset. Taking the limit of continuous sources and receivers, $n \rightarrow \infty$ and $h \rightarrow 0$, and allowing the discrete variable $2kh$ to become the continuous variable x results in

$$K(\omega)=\frac{1}{L_s}\int_{-\frac{L_s}{2}}^{\frac{L_s}{2}} \exp\left[i\omega\left(\sqrt{T_0^2+x^2\left(\frac{1}{v^2}-\frac{1}{v_{st}^2}\right)}-T_0\right)\right]dx. \tag{2.7}$$

We simplify the evaluation of the integral in equation (2.7) by letting the spreadlength go to infinity, $L_s \rightarrow \infty$. This simplification avoids accounting for Cornu's spiral (Born & Wolf, 1980). Denoting $I(\omega)=K(\omega)L_s$ as a scaled version of the transfer function gives

$$I(\omega)=\int_{-\infty}^{\infty} \exp\left[i\omega\left(\sqrt{T_0^2+x^2\left(\frac{1}{v^2}-\frac{1}{v_{st}^2}\right)}-T_0\right)\right]dx. \tag{2.8}$$

This type of integral can be approximately evaluated by the method of stationary phase (Born & Wolf, 1980; Bleistein *et al.*, 2001). Within this approximation, $I(\omega)$ is given by

$$I(\omega)=\sqrt{2\pi}e^{i\pi/4}\left[\frac{\partial^2\phi}{\partial x^2}\right]_{x=x_{st}}^{-1/2} e^{i\phi(x_{st})}, \tag{2.9}$$

with x_{st} the stationary point of the phase function $\phi(x)$ of equation (2.8) where

$$\phi(x)=\omega\left(\sqrt{T_0^2+x^2\left(\frac{1}{v^2}-\frac{1}{v_{st}^2}\right)}-T_0\right). \tag{2.10}$$

In equation (2.9), the subscript $x=x_{st}$ indicates the quantity is to be evaluated at the stationary point. To find the stationary point, we set the x-derivative of $\phi(x)$ to zero and identify the stationary point $x_{st}=0$, where the moveout curve and the stacking curve are tangent (see Figure 2.1).

After calculating the second x-derivative of the phase function and evaluating it at the stationary point, the scaled transfer function $I(\omega)$ can be expressed, in the stationary phase approximation, as

$$I(\omega)=v_{st}\sqrt{\frac{2\pi T_0}{\omega}}\frac{\exp(i\ \mathrm{sgn}(v_{st}-v)\pi/4)}{\mid\sqrt{1-(v_{st}/v)^2}\mid}, \tag{2.11}$$

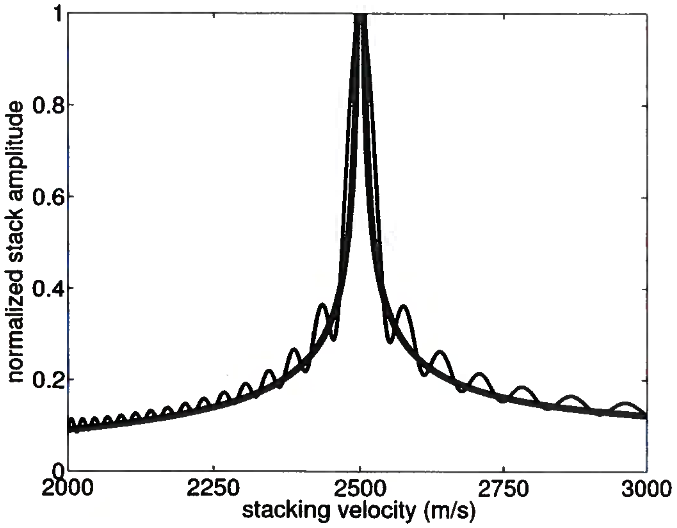

Figure 2.2. Amplitude of the stacking response in the stationary phase approximation (thick, black line) and the exact solution (thin, blue line) for the acquisition parameters: $T_0 = 2$ s, $\omega = 25$ Hz, $v = 2500$ m/s, $n = 48$, and $L_s = 4800$ m.

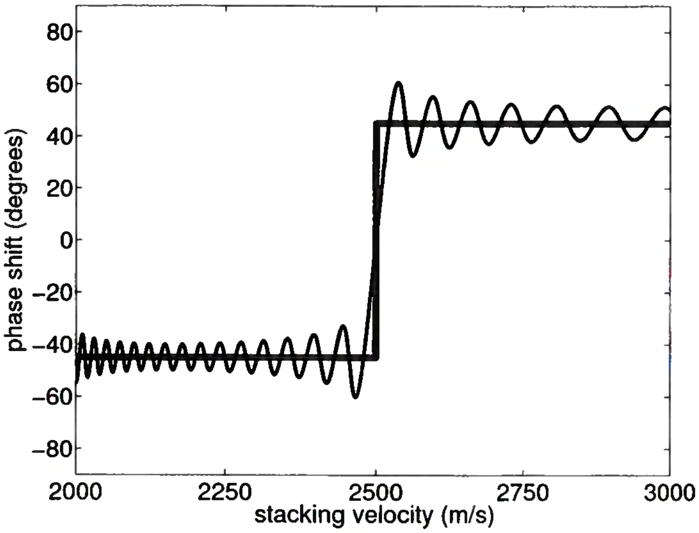

Figure 2.3. Phase of the stacking response in the stationary phase approximation (thick, black line) and the exact solution (thin, blue line) for the acquisition parameters: $T_0 = 2$ s, $\omega = 25$ Hz, $v = 2500$ m/s, $n = 48$, and $L_s = 4800$ m.

where

$$\operatorname{sgn}(x) = \begin{cases} +1 & \text{when } x > 0 \\ -1 & \text{when } x < 0 \end{cases} \tag{2.12}$$

Note that the stationary phase approximation is an asymptotic series - it is valid in the limit of $\omega \rightarrow \infty$. The limiting quantity can be expressed in terms of a dimensionless number instead of ω (Bleistein *et al.*, 2001; p. 131). In this way, the accuracy of the stationary phase approximation depends on ω being large relative to another quantity. Equation (2.11) states that, when an event is stacked with a velocity that is not the true velocity, a phase shift of ±45° results depending on whether the stacking velocity is higher or lower than the true velocity. The amplitude of $I(\omega)$ scales with $\sqrt{T_0}$ and $\mid \sqrt{1-(v_{st}/v)^2} \mid^{-1}$ as a function of stacking velocity. It is worth noting that the amplitude of the scaled transfer function $I(\omega)$ "blows up" when $v_{st} = v$. This is due to the fact that the stationary phase approximation is not valid for $v_{st} = v$; in that case, the entire moveout curve is tangent to the stacking curve. The stationary phase approximation is therefore meaningful only when $v_{st} \neq v$. From equation (2.11), the amplitude response is inversely proportional to $\sqrt{\omega}$. Hence, stacking errors cause the stacked waveform to be enriched in lower frequencies - an effect identical to stacking NMO-stretched waveforms. This low-pass filtering of the waveforms due to stacking errors has been mentioned previously by Bleistein *et al.* (2001). On page 15, the authors state that "the high frequencies of the data may be suppressed by stacking. This is because the arrivals may not be exactly aligned before stacking, causing the stacking process to sum higher frequency components out of phase". Through figures showing the amplitude and time delay of the stacking response as a function of stacking velocity, Gausland (2004) limited his discussion of the stacking response to the amplitude decay term, $\mid \sqrt{1-(v_{st}/v)^2} \mid^{-1}$, and the phase shift, $\operatorname{sgn}(v_{st} - v)\pi/4$.

In Figures 2.2 and 2.3, we plot the amplitude and phase as a function of stacking velocity for the acquisition parameters used by Gausland ($T_0 = 2$ s, $\omega = 25$ Hz, $v = 2500$ m/s, $n = 48$, and $L_s = 4800$ m) and for the scaled transfer function in the stationary phase approximation, equation (2.11). The trend of the exact solution agrees with the stationary phase approximation. Note that, in his article, Gausland (2004) plotted the phase shift θ, shown in Figure 2.3, as a time-delay by using $t_{delay} = \theta/\omega$. With this relationship between time-delay and phase shift, Gausland claimed that the time-delay "... is frequency dependent, and will be inversely proportional to frequency ...". However, as seen in equation (2.11), the effect of mis-stacking is not purely amplitude decay and phase-shift as a function of stacking velocity. There is the factor of $1/\sqrt{\omega}$, which, when coupled with the ±45° phase-shifts, acts to half-integrate a waveform in the process of mis-stacking. This effect can be thought of as both a time-delay and blurring.

If an event had an infinite moveout velocity ($v \rightarrow \infty$) and was stacked in the offset domain with a finite stacking velocity, an analogy would exist between the stacking response, equation (2.11), and migration by diffraction summation. This analogy exists because an event with an infinite moveout velocity in the offset domain looks like a horizontal reflector in the midpoint domain, as shown in Figure 2.4. To pursue this further, as $v \rightarrow \infty$,

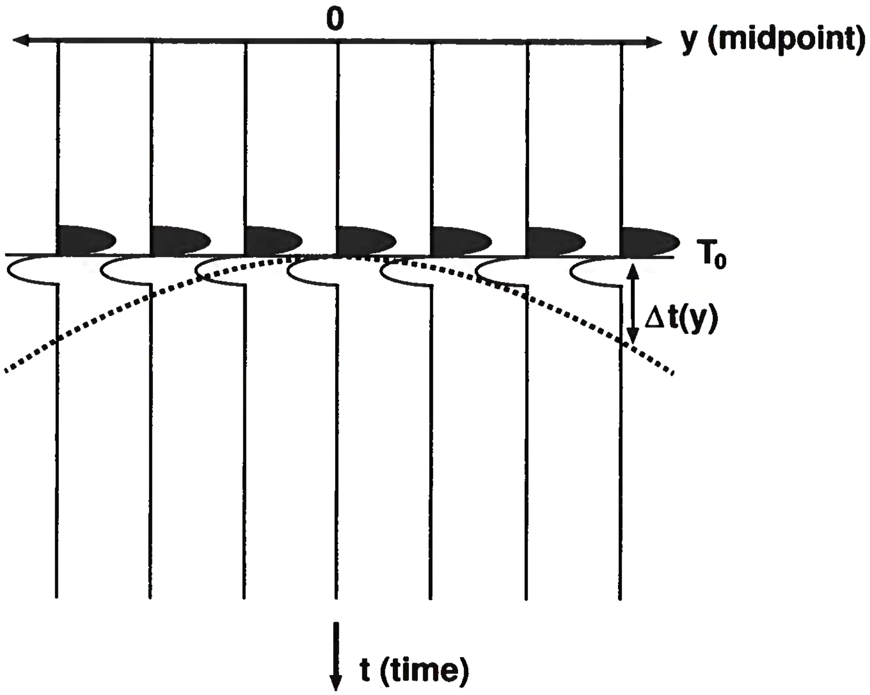

Figure 2.4. Migration of a horizontal reflector by diffraction summation in the midpoint domain. Stacking an event with infinite moveout velocity would look the same as in this plot, except that it would be in the offset domain (compare with Figure 2.1). Hence, an analogy exists between migration and stacking in this case.

equation (2.11) becomes

$$I(\omega) = v_{st}\sqrt{\frac{2\pi T_0}{\omega}}\exp(-i\pi/4). \tag{2.13}$$

Two of the three corrections made to simple diffraction summation for Kirchhoff migration are shown in equation (2.13). The factor $v_{st}\sqrt{T_0}$ requires multiplying the result of diffraction summation by $1/v_{st}\sqrt{T_0}$ to recover the true waveform after diffraction summation. Yilmaz (1987) calls this the *2D geometrical spreading factor.* Furthermore, recovery of the true waveform after diffraction summation also requires multiplying by $\exp(i\pi/4)\sqrt{\omega}$, the half-derivative. This correction is called the *wavelet shaping factor* (Yilmaz, 1987). The final correction to diffraction summation, known as the *obliquity factor* (Yilmaz, 1987), does not appear in this analogy since the reflector we study here is horizontal. The obliquity factor is only relevant for dipping reflectors. In a later section of this chapter, we derive the migration response for a generally dipping reflector and recover the obliquity factor.

Finally, we come back to the issue why the important parameter for the stack response is the spreadlength and not the fold. Gausland (2004) nicely made this observation in his discussion of the stack as an array; where does the fold versus spreadlength issue appear in our stationary phase analysis? Since we (a) took the sources and receivers to be continuously distributed in equation (2.7) and (b) let the spreadlength be infinite in equation (2.8), the result of the stationary phase analysis, equation (2.11), does not contain either the fold or the spreadlength. Hence, equation (2.11) says nothing about the fold versus spreadlength issue. Knowing the assumptions that brought the derivation to the point of applying the stationary phase approximation, though, we can see why the spreadlength is the parameter which governs the stack response and not the fold. The fold issue has to do with our allowing the sources and receivers to be continuously distributed. Having a finite number of sources and receivers instead is identical to approximating an integral of a curve with a finite number of rectangles underneath the curve. This is why we invoked continuous receivers in moving from a series to an integral in equation (2.7). Therefore, differences in fold translate into differences in sampling of the integrand of equation (2.7). As long as the sampling is sufficient to avoiding aliasing, the series quickly approaches the integral. This fact is evident in Gausland's third figure wherein the seemingly random "chatter" at low stacking velocities, or steep moveouts, disappears when moving from a fold of 12 to a fold of 48. As long as aliasing is not a problem, the issue of fold is purely one of sampling. Regarding spreadlength, we earlier mentioned, prior to equation (2.8), that taking the spreadlength to be infinite meant not accounting for Cornu's spiral. Cornu's spiral is a parametric plot (see Figure 2.5) of the Fresnel cosine and sine integrals as their upper limit (the spreadlength) goes to ∞ (Born & Wolf, 1980). These integrals are central in the development of the stationary phase approximation. As the spreadlength gets larger and larger, the two integrals approach the same value, as seen in Figure 2.5. At this limiting point, the angle they make with the x-axis is 45°; this is an indication of the 45° phase shifts appearing in the stationary phase approximation, equation (2.11). Away from this limiting point, the two integrals spiral around; this gives rise to the "wobble" seen in the phase shift versus stacking velocity plot in Figure 2.3. The spiraling also gives rise to the "wobble" seen in the amplitude versus stacking velocity plot in Figure 2.2. As seen in Figure 2.2 and

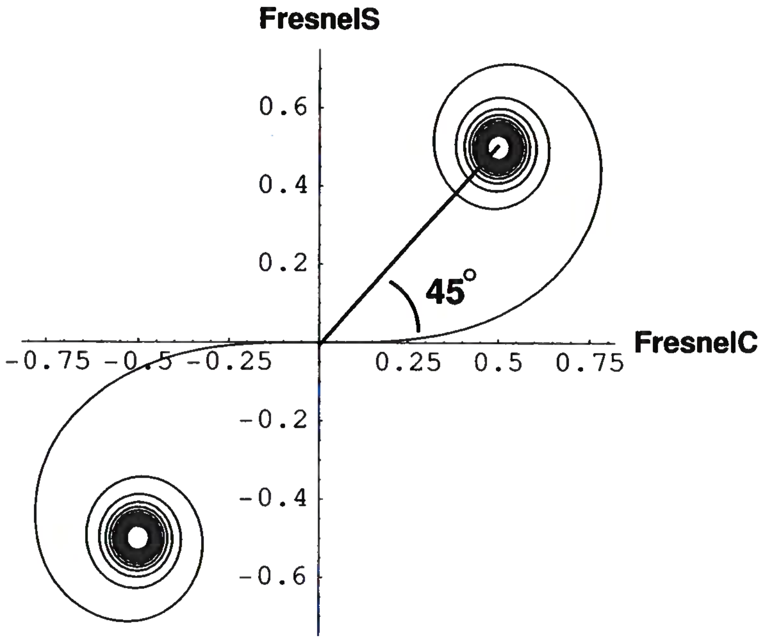

Figure 2.5. Cornu's spiral; adapted from Born & Wolf (1980). The x-axis is the Fresnel cosine integral (FresnelC) and the y-axis is the Fresnel sine integral (FresnelS). This is a parametric plot where the Fresnel cosine and sine integrals are plotted as a function of their upper limit, with their lower limit at zero. When the upper limit is zero, the curve is at the origin. As the upper limit $\to \infty$, the curve spirals in toward the point (0.5,0.5). Similarly, as the upper limit $\to -\infty$, the curve spirals in toward the point (-0.5,-0.5). The fact that the Fresnel cosine and sine integrals have equal values at their limiting point is an indication of the 45° phase shift that comes from the stationary phase approximation, equation (2.9).

survey parameter	value
offset spacing, $2h$	400 m
fold, $2n+1$	5
true NMO velocity, v_{tr}	2000 m/s
erroneous stacking velocity, v_{st}	1800 m/s
zero-offset two-way-traveltime, T_0	0.9 s
dominant frequency	20 Hz

Table 2.1. Parameters for studying stacking errors

Gausland's fourth figure, the length scale of the "wobble" is directly related to the width of the main lobe. Hence, the main factor of importance to the stack response, as long as aliasing is not an issue, is the spreadlength, as witnessed by its role in Cornu's spiral.

2.4 Numerical test of mis-stacking horizontal-interface and fault-plane reflections

We illustrate the impact of stacking velocity errors on a post-stack migrated image with a numerical example, using the spectral-element method (SEM) code discussed in Chapter 4. The SEM code has been developed by researchers (Komatitsch & Tromp, 2003; Komatitsch & Vilotte, 1998; Ampuero, 2002) over the past 5-10 years in the global seismology community. The example does not satisfy the approximations that we made above to obtain analytic results for the stack response; it has finite spreadlength, discrete receivers, and finite frequency. To evaluate the stack response, we numerically calculate the exact transfer function $K(\omega)$ - the finite series appearing in equation (2.4). Table 2.1 summarizes the parameters from the numerical survey that are necessary to evaluate the exact transfer function. Note that the offset spacing is twice the shot spacing (see Figure 2.6) and that the velocity of layer 1 serves as the true NMO velocity. We generate two tests for the stacking velocity - one with the true NMO velocity (2000 m/s) and another with a -10% error (1800 m/s). The material properties for the model investigated here are shown in Table 2.2, with the geometry depicted in Figure 2.6.

We first simulated the stack response exactly from equation (2.4). Both the amplitude and phase of the stacked waveform are displayed in Figure 2.7 as a function of error in stacking velocity. When $v_{st} = v_{tr}$, the stacked amplitude is maximized and the phase shift is zero. Away from the true velocity, though, significant amplitude degradation and phase error occur. We highlight with circles in Figure 2.7 the amplitude and phase at an erroneous value of $v_{st} = 1800$ m/s. For such a -10% error in stacking velocity, the stacked amplitude of a horizontal reflector should be reduced by a factor of ~ 0.6 relative to the amplitude at the correct stacking velocity and have acquired a phase shift of $\sim 65°$. For these survey parameters, it is evident that the geometrical optics limit, in which the phase shifts away

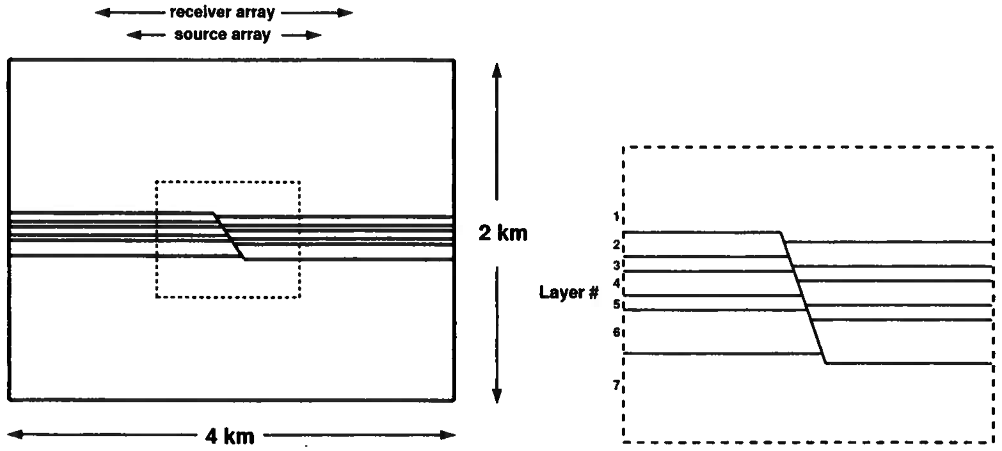

Figure 2.6. The entire numerical model with a zoom-in of the normal fault. The zoom area is shown on the entire numerical model with a dashed rectangle. The lengths of the source and receiver arrays are shown by extended arrows. Eleven sources are evenly-spaced over 2000 m (200-m shot interval), and 241 receivers span 3000 m (12.5-m receiver interval). In the zoom, the layers are labeled with numbers 1-7 corresponding to the material properties for models listed in Table 2.2.

Layer	Thickness (m)	v_p (m/s)	ρ (kg/m^3)
1	900	2000	2000
2	50	2350	2080
3	30	2000	2000
4	50	2350	2080
5	30	2000	2000
6	90	2350	2080
7	850	2000	2000

Table 2.2. The model for the SEM examples in this chapter. $v_s = v_p/\sqrt{3}$, where v_s and v_p refer to the S-wave and P-wave speeds. The symbol ρ refers to density.

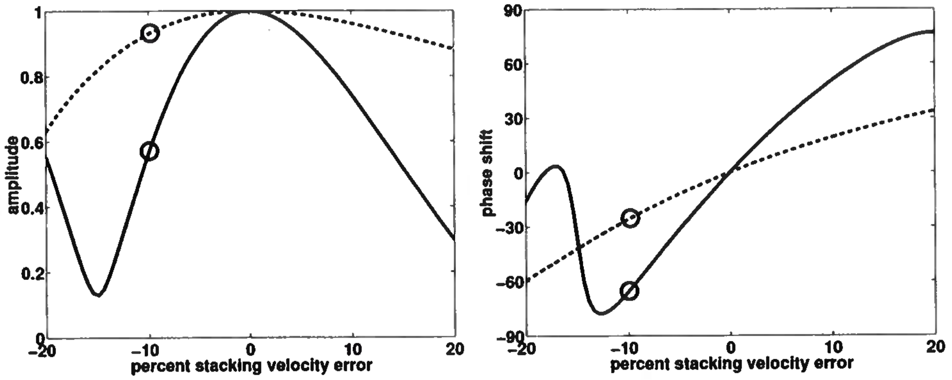

Figure 2.7. Amplitude and phase of the stack response as a function of percent error in stacking velocity for the survey parameters in Table 2.1. These plots are for a frequency of 20 Hz; the amplitude and phase behavior is thus a good approximation of what would happen for a wavelet with a peak frequency of 20 Hz. The solid line is for a horizontal reflector, and the dashed line is for a flat reflector with 45° dip. The curve for the horizontal reflector is calculated from equation (2.4) using the time delays in equation (2.2). The curve for the dipping reflector is calculated from the time delays in equation (2.66), derived in a later section of this chapter. The values for a -10% error in stacking velocity are highlighted by circles, since this case is presented in subsequent figures. Due to a later zero-offset traveltime, the dipping event is less sensitive to amplitude and phase errors.

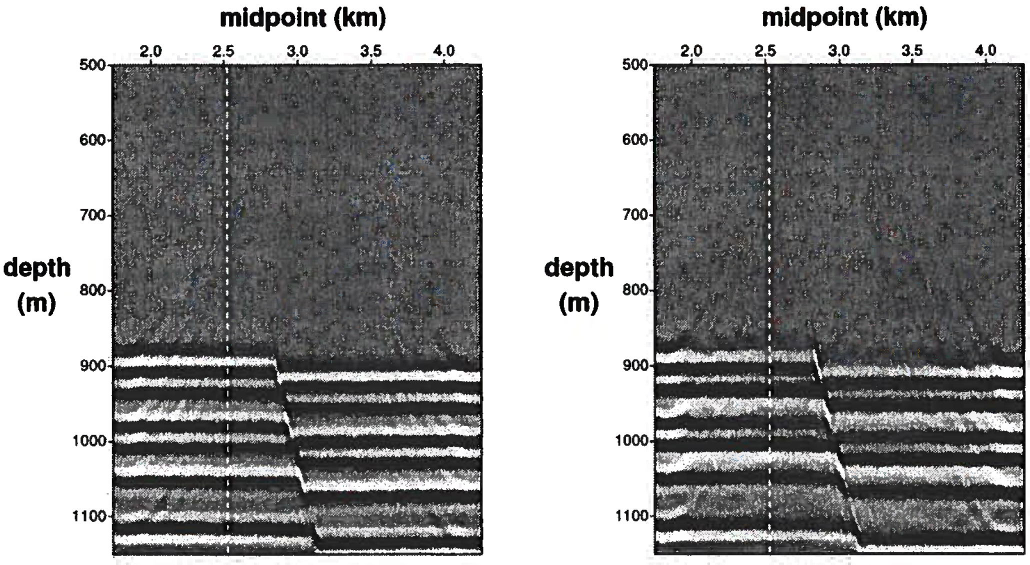

Figure 2.8. Two migrated images for the model described in Table 2.2: on the left is the image for the correct stacking velocity and on the right is the image for a -10% error in stacking velocity. The -10% error occurs for all reflections. The image for -10% error has been degraded. The vertical white dashed lines indicate slices from the migrated image and are analyzed in subsequent figures.

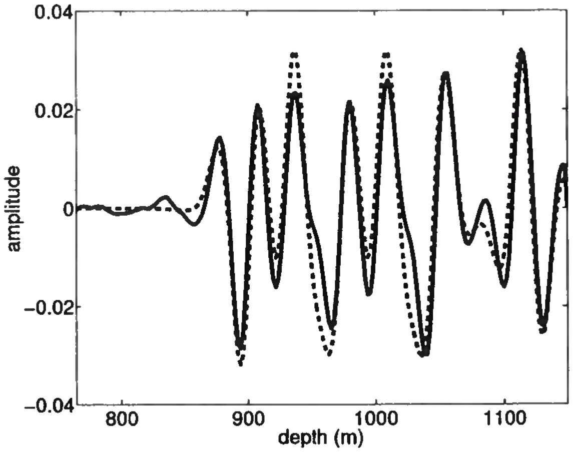

Figure 2.9. Overlap of the trace migrated with the correct stacking velocity (solid) and the convolutional model (dashed) along the white, dashed line of Figure 2.8.

from the true stacking velocity should be ± 45°, has not been reached. This demonstrates that, away from the geometrical optics limit, the errors caused by stacking-velocity errors are determined in large part by the specifics of the survey and acquisition geometry.

To test the array-based theory for stacking-velocity errors presented in the previous section, we performed a complete sequence of full-waveform SEM modeling and processing with Seismic Unx (SU) code (Stockwell, 1997) and formed migrated images both with and without stacking-velocity errors. The full-waveform SEM modeling utilizes a Ricker source wavelet with a peak frequency of 20 Hz. This value of peak frequency is the same value as the frequency used in Figure 2.7. The migration velocity for the following examples is kept as the correct migration velocity. Two migrated images are displayed in Figure 2.8. In comparing the migration without stacking errors to the migration with them, the degradation of the image with errors is noticeable. In order to quantify the error in the images, we first took a trace from the migrated image shown by the white dashed lines in Figure 2.8. This trace is shown as a solid line in Figure 2.9. Also plotted in Figure 2.9 is the convolutional model (i.e., the model without multiples) obtained from the far-field P-waveform (Ricker) and the known reflectivity series. Good agreement exists between the zero-offset migration of the stacked data and the convolutional model, as there should be. The agreement is not exact since both interbed and intrabed multiples are ignored in the convolutional model.

In the left panel of Figure 2.10, we plot the same convolutional model as in Figure 2.9, but now show the slice of the migration with incorrect stacking velocity in the solid line. As discussed before, amplitude degradation and phase shift is evident between the convolutional model and the migration with erroneous stacking velocity. As a further check if the array-based theory for stacking errors accurately describes the migrated waveform in the top panel of Figure 2.10, we multiplied the far-field P-waveform by 0.6, phase-shifted it by 65°, and recomputed the convolutional model. These factors come from the circles at -10%

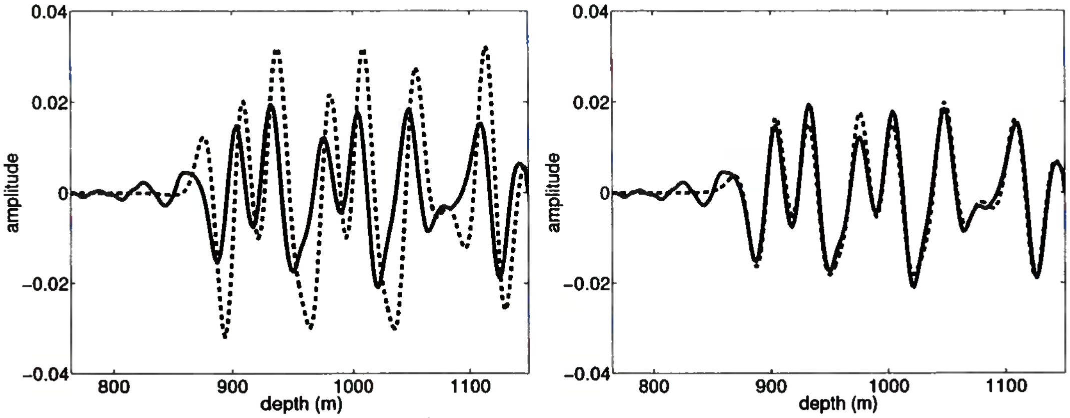

Figure 2.10. Left: an overlap of the incorrect stacking-velocity migration (solid) and the correct convolutional model (dashed) along the white, dashed line of Figure 2.8. Note the disparity in the amplitudes and phases of the two plots. Right: an overlap of the incorrect stacking-velocity migration (solid) and the incorrect convolutional model (dashed) calculated by dampening and phase shifting the far-field P-waveform by the factors predicted in Figure 2.7.

error in Figure 2.7 for the horizontal reflector. The damped and shifted version of the convolutional model is plotted in the right panel of Figure 2.10 together with the migration with erroneous stacking velocities. Indeed, by virtue of the excellent match of the two curves in the bottom plot of Figure 2.10, incorrect stacking velocities have caused the amplitude and phase response of the migrated waveform to be as predicted by the exact array-based theory (not in the geometrical optics limit) applied at the dominant frequency of the wavelet.

We now turn to the influence of the stacking velocity errors on the fault-plane reflections instead of the horizontal ones. Shown in Figure 2.11 are dip-filtered versions of the migrations both with and without the errors in stacking velocity. We dip filter the images in order to isolate the reflection from the fault plane, as in Haney *et al.* (2004). The dip-filter we use is applied in the frequency-wavenumber domain as described in Chapter 4. Note that, because of the migration, the correct direction to slice the fault-plane reflections is perpendicular to the fault, as shown in Figure 2.11 by the white arrows.

In Figure 2.12, we show the slices taken from the dip-filtered fault-plane reflections for both cases of stacking velocity error and no error and compare them to the same wavelet. Compared to the horizontal layer reflections examined previously, the fault-plane reflection is relatively insensitive to a stacking velocity error of -10%, as predicted by considering their stack responses in Figure 2.7. This phenomenon is discussed in a later section of this chapter on DMO. It can be understood by the fact that the fault-plane reflection has a larger zero-offset traveltime than does a horizontal reflector at the same depth. The larger zero-offset traveltime means that an erroneous moveout curve for a fault-plane reflection has a larger region of tangency with the stacking curve near its stationary point than for

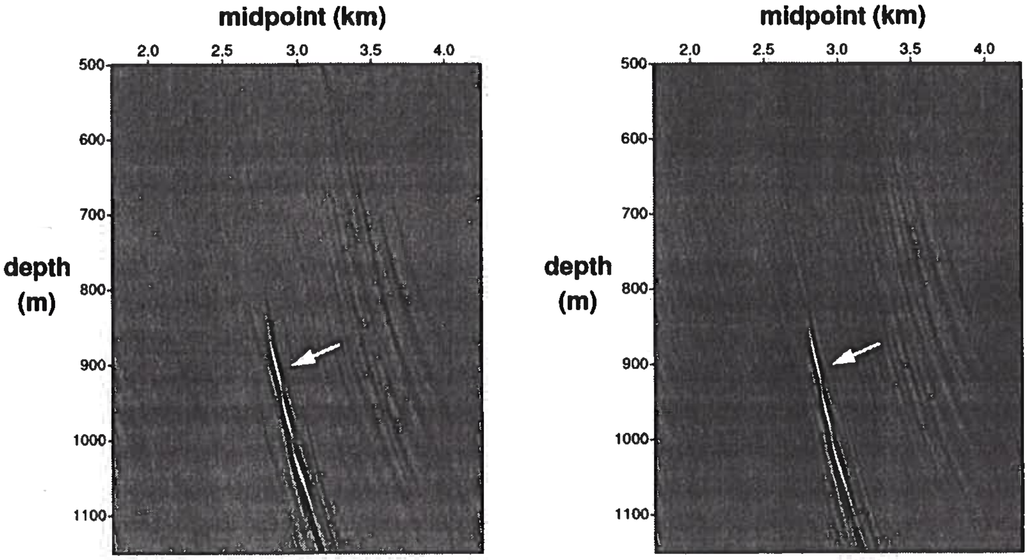

Figure 2.11. Dip-filtered versions of the images in Fig. 2.8; on the left is the image for the correct stacking velocity after dip-filtering and on the right is the image for a -10% error in stacking velocity after dip-filtering. The *f*-*k* dip-filtering highlights the reflections from the fault plane. In order to study the reconstructed waveform, we take slices of the migrated image perpendicular to the fault, as indicated by the white arrows.

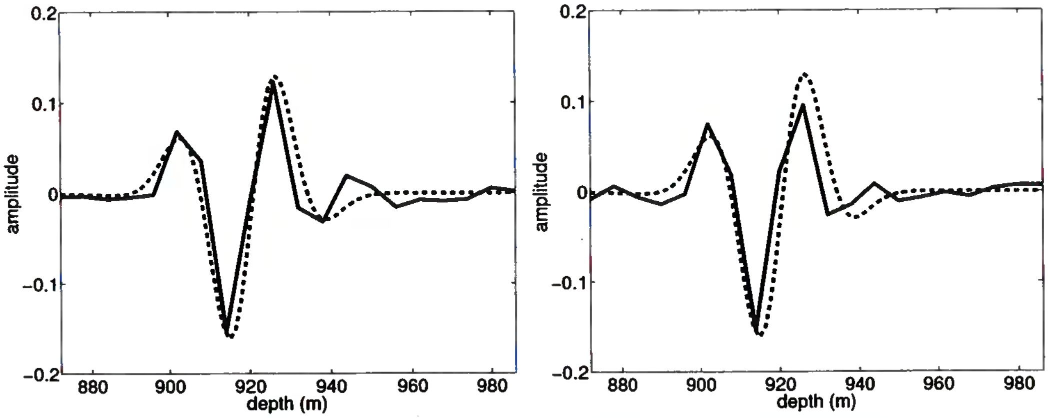

Figure 2.12. Slices perpendicular to the dip-filtered fault-plane reflections for the case of no stacking velocity error (left) and -10% error (right). The slices are shown as solid lines and the P-waveform by a dashed line. Though a small amount of amplitude degradation or phase shift may be seen in the right panel, for the most part the fault-plane reflections are relatively insensitive when compared to the severe amplitude and phase distortions experienced by the horizontal reflections.

a horizontal reflector. Fault-plane reflections may be more difficult to process in non-ideal acquisition geometries (for instance, when the more poorly sampled cross-line direction is in the dip-direction of the fault), but once their reflection has been captured, their imaged waveform is relatively robust in shape and amplitude. It can at least be said that fault-plane reflections are no more sensitive to stacking velocity errors than are horizontal reflectors.

2.5 The migration response

We have already touched on the filtering action of migration in the discussion on the stack response, specifically with equation (2.13). In the remainder of this section, we generalize the above connection with migration for the case of a dipping reflector and recover the obliquity factor, which was not present for a flat reflector. Moreover, I am able to confirm the fact that the amplitudes and phases of post-stack time-migrated waveforms from planar features are virtually insensitive to migration velocity errors. The same cannot be said for diffractions, which can contain errors because of incorrect migration velocities just as stacked waveforms contained errors due to mis-stacking.

Let us study the phase and amplitude distortion of a waveform at x_{in}, t_{in} (in the zero-offset section) after it is migrated to an output point x_{out}, t_{out}. Suppose a zero-offset (stacked) section contains a single dipping event, in an otherwise homogeneous medium, with a time dip

$$p = 2\ \sin\theta / v, \tag{2.14}$$

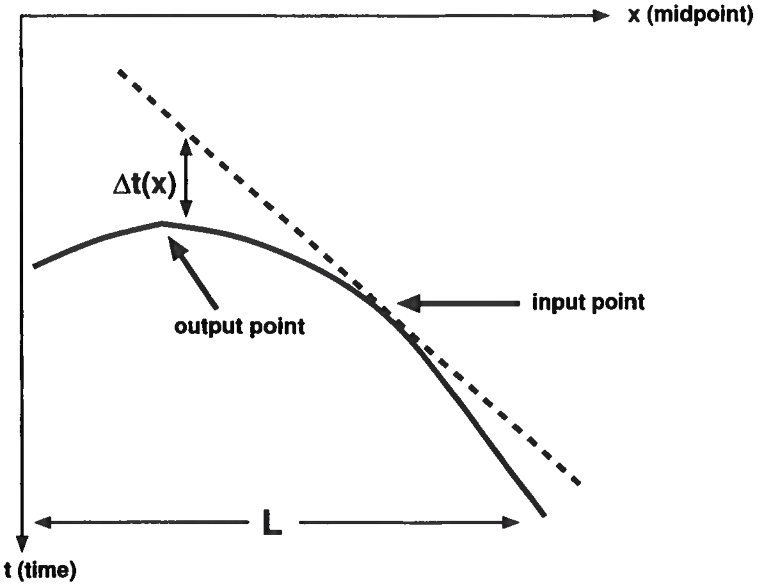

Figure 2.13. Zero-offset section showing a sloping reflection (dashed) and the migration hyperbola (solid). The input and output points are also highlighted. The time-delay between the sloping reflection and the migration hyperbola is shown by $\Delta t(x)$, and the migration aperture is denoted L.

where θ is the (geologic) dip and v is the velocity of the medium. Figure 2.13 shows the geometry of the sloping reflection. The equation describing the arrival time of the sloping reflection as a function of midpoint, x, in the zero-offset section is

$$t_{ref}(x) = px + t_{in} - px_{in}. \tag{2.15}$$

Note that the dipping reflector is a line in the zero-offset section and that it contains the input point (x_{in},t_{in}).

The dipping event is migrated with a hyperbola whose apex is at the output point (x_{out},t_{out})

$$t_{hyp}(x) = \sqrt{t_{out}^2 + \frac{4(x - x_{out})^2}{v_m^2}}, \tag{2.16}$$

with a migration velocity v_m not necessarily equal to v, the velocity of the medium. Setting the equations (2.15) and (2.16) and their x-derivatives equal to each other at the input point, $(x_{in},t_{in,})$, gives the conditions relating the input and output points:

$$t_{out} = t_{in}\sqrt{1 - p^2 v_m^2/4}, \tag{2.17}$$

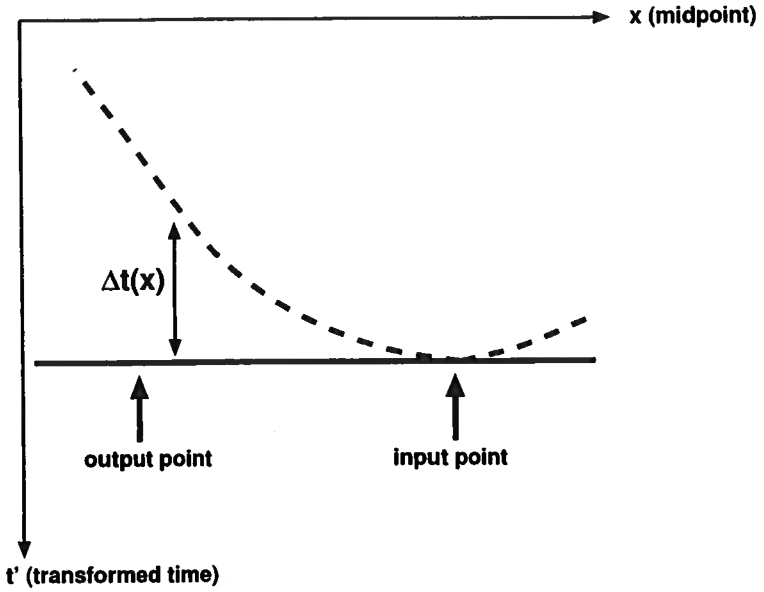

Figure 2.14. Zero-offset section whose time axis has been transformed in such a way that the hyperbola of Figure 2.13 is a horizontal line (solid) and the dipping reflector is concave upward (dashed). Migration can be thought of as horizontal stacking after this time transformation and extraction of the stacked value along the solid line. The time delay, $\Delta t(x)$, between the dipping reflector and the hyperbola governs the migration response.

$$x_{out} = x_{in} - pv_m^2 t_{in}/4. \tag{2.18}$$

These two equations explicitly show the spatial and temporal transformation of migration; the use of them to migrate is sometimes called *map migration.* The migration hyperbola is shown in Figure 2.13, along with the input and output points.

Migration by diffraction summation forms an image by summing along the hyperbolic trajectory. This can be visualized as is shown in Figure 2.14, where the same zero-offset section is shown in a coordinate system whose time axis has been transformed. The transformation makes the hyperbola of Figure 2.13 horizontal and, as a result, the dipping reflector is concave upward. The exact form of this transformation is not important; what is important is that the hyperbolic summation can now be visualized as a simple horizontal stack. The response of this stacking depends on the time differences between the two curves, shown as $\Delta t(x)$ in Figure 2.14.

In real seismic data, the zero-offset section consists of discrete seismic traces, which we depict in Figure 2.15 by having zero offset wavelets centered on the curve for the sloping reflection. Suppose that the zero-offset wavelet is $f(t)$ and that geometric spreading has been corrected for in the zero-offset section (hence the wavelet has the same amplitude at all midpoints). Then, the result of summing along the hyperbola, or the migration response

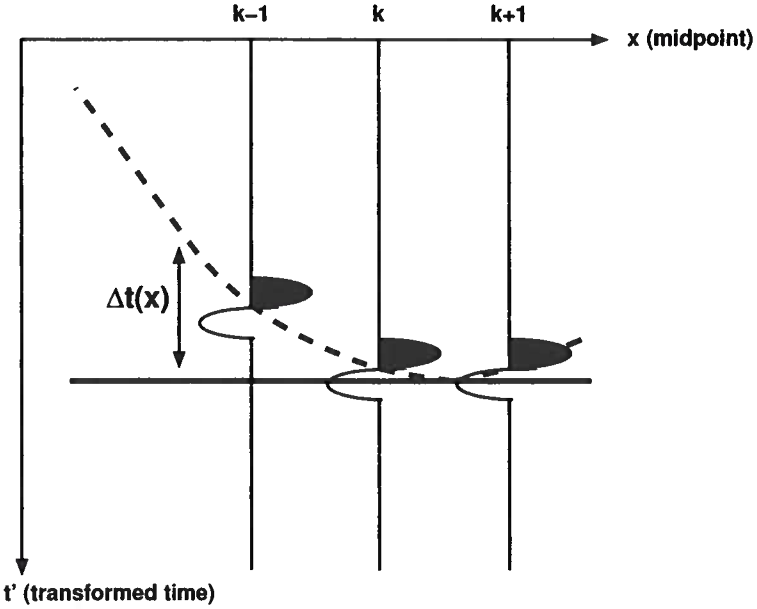

Figure 2.15. As in Figure 2.14, a zero-offset section whose time axis has been transformed in such a way that the hyperbola of Figure 2.13 is a horizontal line (solid) and the sloping reflection is concave upward (dashed). Here, discrete spatial sampling is depicted with the input traces labeled k-1, k, k+1, etc.

$g(t)$, is similar to the stack response of the previous section

$$\begin{aligned} g(t) &= \frac{1}{N}\left[f(t-\Delta t_1)+\cdots+f(t-\Delta t_{k-1})+\right. \\ &\left. f(t-\Delta t_k)+f(t-\Delta t_{k+1})+\cdots+f(t-\Delta t_N)\right], \end{aligned} \tag{2.19}$$

where N is the total number of traces within the migration aperture, L (see Figure 2.13), and Δt_k represents the time delay at the k-th midpoint trace. The factor $1/N$ is included as a normalization. Note that if N is the total number of traces within the migration aperture, L, and the midpoints are equally spaced, then the midpoint spacing, h, is related by

$$N = \frac{L+h}{h}, \tag{2.20}$$

or, if $L \gg h$, $N = L/h$. The time delays, $\Delta \mathrm{t}(x)$, are needed in equation (2.19). Since we know the forms of the curves for the dipping reflector and the migration hyperbola in the zero-offset section, t_{ref} and t_{hyp} in equations (2.15) and (2.16), the delays are simply

$$\Delta t_k = t_{ref}(kh) - t_{hyp}(kh), \tag{2.21}$$

where the midpoint location x has been discretized by kh (the trace number times the trace spacing).

When we use the expression for the time delays at each midpoint, the migration response, equation (2.19), can be most easily evaluated in the frequency domain, just as for the case of stacking. Denoting the Fourier transforms of $f(t)$ and $g(t)$ as $F(\omega)$ and $G(\omega)$, the transform of equation (2.19) may be written

$$G(\omega) = F(\omega)K(\omega), \tag{2.22}$$

where the transfer function, K, is

$$K(\omega) = \frac{1}{N}\sum_{k=1}^{N} e^{i\omega\Delta t_k}. \tag{2.23}$$

Since the time delays, Δt_k, are not linear in the midpoint trace number k, this summation cannot be done analytically. We proceed as in the previous section on stacking by transforming the series into an integral and evaluating it by stationary phase (Born & Wolf, 1980). We skip the details of this transformation since it mirrors closely the case for stacking.

Denoting $I(\omega) = K(\omega)L$ as a scaled version of the transfer function gives

$$I(\omega) = \int_{-\infty}^{\infty} e^{i\omega\Delta t(x)}dx, \tag{2.24}$$

where

$$\Delta t(x) = t_{ref}(x) - t_{hyp}(x). \tag{2.25}$$

Note that, since $L \to \infty$ and $I(\omega) = K(\omega)L$, there should be some issues with amplitude density in this approximation (for instance, does $I(\omega) \to \infty$?). The type of integral in equation (2.24) can be approximately evaluated by the method of stationary phase (Born & Wolf, 1980). In this limit, $I(\omega)$ is given by

$$I(\omega) = \sqrt{2\pi} e^{i\pi/4} \left[\frac{\partial^2 \phi}{\partial x^2} \right]^{-1/2}_{x=x_{st}} e^{i\phi(x_{st})}, \tag{2.26}$$

where x_{st} is the stationary point of the phase function $\phi(x)$ of equation (2.24) given by

$$\phi(x) = \omega \Delta t(x). \tag{2.27}$$

In equation (2.26), the subscript $x = x_{st}$ indicates the quantity is to be evaluated at the stationary point. For the case of diffraction summation considered here, the stationary point is the input point ($x_{st} = x_{in}$) - where the values and x-derivatives of the hyperbola and the curve for the sloping reflection are the same (see Figure 2.14).

Using equation (2.25) and equations (2.15) and (2.16), iwe can write the phase function of equation (2.27) as

$$\phi(x) = \omega \left(px + t_{in} - px_{in} - \sqrt{t_{out}^2 + \frac{4(x - x_{out})^2}{v_m^2}} \right). \tag{2.28}$$

Since the second x-derivative of $\phi(x)$ is to be evaluated at the stationary point, (x_{in},t_{in}), it is best to use equations (2.17) and (2.18) to recast equation (2.28) in terms of the input point only (i.e., substitute for the output points)

$$\phi(x) = \omega \left(px + t_{in} - px_{in} - \sqrt{t_{in}^2(1 - p^2 v_m^2/4) + \frac{4(x - x_{in} + p v_m^2 t_{in}/4)^2}{v_m^2}} \right). \tag{2.29}$$

Before calculating the second x-derivative of equation (2.29), take note of the two important properties of $\phi(x)$. First, the value of $\phi(x)$ is zero at the input point, that is $\phi(x_{in}) = 0$. Second, by taking the derivative of equation (2.29) with respect to x and evaluating it at the input point, it can be verified that $\partial\phi/\partial x = 0$ at x_{in}. This is because the migration hyperbola is tangent to the sloping reflection in the zero-offset section at the input point.

Taking the second x-derivative of equation (2.29) yields

$$\frac{\partial^2 \phi}{\partial x^2} = \frac{-4\omega v_m t_{in}^2 (1 - p^2 v_m^2/4)}{\left(v_m^2 t_{in}^2 (1 - p^2 v_m^2/4) + 4(x - x_{in} + p v_m^2 t_{in}/4)^2\right)^{3/2}}. \tag{2.30}$$

Equation (2.26) states that the second x-derivative of $\phi(x)$ is to be evaluated at x_{in}. Substituting x_{in} for x in equation (2.30) results in

$$\frac{\partial^2 \phi}{\partial x^2}|_{x=x_{in}} = \frac{-4\omega t_{in}^2 (1 - p^2 v_m^2/4)}{v_m^2 t_{in}^3}. \tag{2.31}$$

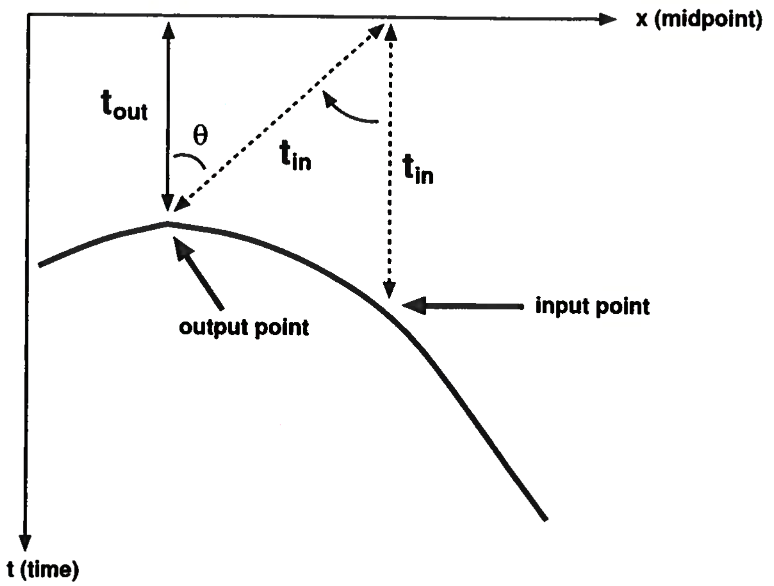

Figure 2.16. Geometric argument used to relate the obliquity factor to the cosine of an angle. Since the impulse response of zero-offset migration is a circle, the input time t_{in} can be rotated to the output point, thereby defining a right triangle with a hypotenuse of length t_{in}.

Substituting this expression into equation (2.26) gives the scaled migration response in the stationary phase approximation

$$I(\omega) = \sqrt{2\pi} e^{i\pi/4} \left[\frac{-4\omega t_{in}^2 (1 - p^2 v_m^2/4)}{v_m^2 t_{in}^3} \right]^{-1/2}, \tag{2.32}$$

where it is also noted again, with respect to equation (2.26), that $\phi(x_{st} = x_{in}) = 0$.

In equation (2.32) is a term $t_{in}^2(1 - p^2 v_m^2/4)$ appearing under the inverse square root. From equation (2.17), this term is equal to t_{out}^2, the square of the time of the output point. Using this and the fact that $1/\sqrt{-1} = \exp(-i\pi/2)$, we can write equation (2.32) as

$$I(\omega) = \frac{\sqrt{2\pi}}{2} \frac{\exp(-i\pi/4)}{\sqrt{\omega}} \frac{t_{in}}{t_{out}} v_m \sqrt{t_{in}}. \tag{2.33}$$

This expression is the filter applied to the zero-offset waveform by simple diffraction summation. Usually, seismic data processors would like to undo this filter so that the waveform resulting from diffraction summation is equal to the waveform in the zero-offset section. From equation (2.33), the result of the diffraction stack must be multiplied (in the frequency domain) by the half-derivative $\exp(i\pi/4)\sqrt{\omega}$, or the wavelet shaping factor (Yilmaz, 1987), and divided by $v\sqrt{t_{in}}$, or the 2D geometric spreading factor (Yilmaz, 1987), to give

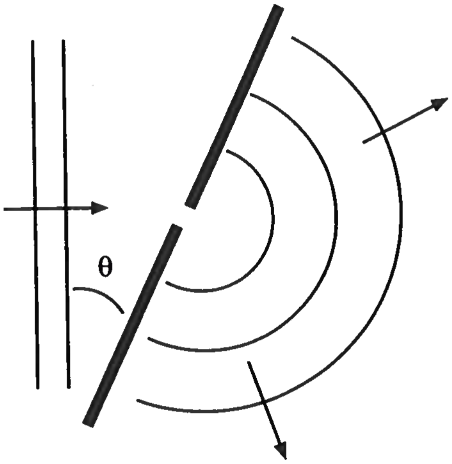

Figure 2.17. Diffraction of a plane wave by a tilted slit

the original waveform. In addition, for a dipping reflector, the factor of t_{in}/t_{out} appearing in equation (2.33) must be removed by multiplying by t_{out}/t_{in}. This is the obliquity factor (Yilmaz, 1987), whose effect is to dampen the amplitude of the diffraction stack for dipping reflectors, such as fault-plane reflections. For horizontal reflectors, the obliquity factor is unity.

In Figure 2.16 a common geometric argument is shown relating the obliquity factor t_{out}/t_{in} to the cosine of an angle θ. As a final note, the obliquity factor physically means that the amplitude of a wave diffracted from a slit depends on that angle of the barrier defining the slit and the propagation direction of the plane wave being diffracted, as shown in Figure 2.17.

Note that nowhere in equation (2.33) does the time dip, p, and therefore the true migration velocity, v appear. This demonstrates the insensitivity of the amplitude and phase of the migrated waveform to departures of the migration velocity v_m from the true velocity v. Comparing the stacking response, equation (2.11), and the diffraction stack response, equation (2.33), the diffraction stack for a reflection is essentially one side of the stacking response. By "one-side", we mean that, for stacking, the filter, equation (2.11), has ±45° phase-shifts, depending on whether or not the stacking velocity is higher or lower than the true velocity. For migration, only a 45° phase shift is needed, irrespective of migration velocity. However, in the case of a diffraction in the zero-offset section instead of a reflection, the response of the diffraction stack to migration velocity errors is identical to the case of mis-stacking. Since, as observed in the numerical modeling of fault-plane reflections earlier, both diffractions and dipping reflections occur at a fault-plane, caution should be taken in interpreting post-stack time-migrated amplitudes originating from a fault plane if it is unclear whether they are diffractions or reflections. Access of the interpreter to an unmigrated section, showing the fault-related diffractions, could help to diagnose areas of less certainty.

2.6 Fault-plane reflections and dip moveout

The formalism outlined above for evaluating the inverse filters for stacking and migration can be extended to another component in the typical seismic data-processing sequence called *dip-moveout* or DMO (Hale, 1991). Whereas stacking operated in the common-midpoint domain, dip-moveout operates in the common-offset domain. The purpose of a traditional DMO is to alter NMO-corrected nonzero offset data in such a way that they become zero-offset. Hence, DMO improves the stack for dipping reflectors that are incorrectly treated by NMO-correction (because of its horizontal-layer assumption). We derive the inverse filter for a diffraction-summation style DMO and then comment on the stacking errors for dipping reflectors after DMO.

In contrast to the previous sections on stacking and zero-offset migration, let's not start analyzing the DMO response from the point of having a discrete number of traces. Instead begin from the stationary phase approximation of the resulting integral, equations (2.9) and (2.10); that is, we do not go through the previous arguments about approximating the summation with an integral. It turns out that DMO is similar to migration: the parts of a common-offset section that fall along a curve (the DMO trajectory) are summed up and placed at the apex of this curve. From equation (2.25), all that is needed to approximate the response of the DMO integral are the time shifts

$$\Delta t(x) = t_{refn}(x) - t_{dmo}(x), \tag{2.34}$$

where the DMO trajectory, $t_{dmo}(x)$, is put in place of $t_{hyp}(x)$ in equation (2.25) and the equation of an NMO-corrected dipping reflector in a nonzero-offset section, $t_{refn}(x)$, is substituted for $t_{ref}(x)$ in equation (2.25). For the application of DMO, x is the midpoint location. We refer to the reflector curve as $t_{refn}(x)$ since the input to DMO is not the true reflector curve, but that curve after NMO-correction has been applied.

To begin studying the DMO response, we need $t_{dmo}(x)$ and $t_{refn}(x)$. The summation trajectory for DMO, $t_{dmo}(x)$, follows from the DMO ellipse (Hale, 1991)

$$\frac{T_0^2}{T_{nmo}^2} + \frac{x^2}{h^2} = 1, \tag{2.35}$$

where T_0 is the zero offset time (the output of DMO), T_{nmo} is the NMO corrected time (the input to DMO), x is the midpoint location, and h is the half-offset. Using the idea that the DMO trajectory is the locus of input points whose apex is the output point, $t_{dmo}(x)$ becomes, from equation (2.35)

$$t_{dmo}(x) = \frac{t_{out}}{\sqrt{1 - (x - x_{out})^2/h^2}} \tag{2.36}$$

with t_{out} the output time and x_{out} the output midpoint. The DMO trajectory, equa-

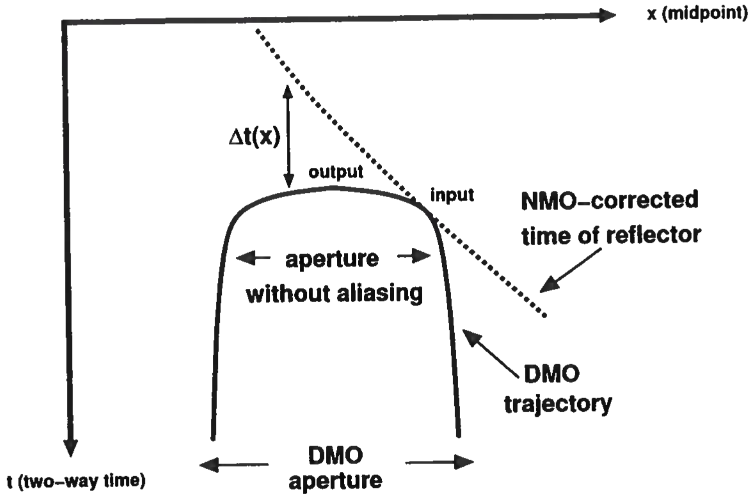

Figure 2.18. DMO by the diffraction-summation method in a common-offset gather

tion (2.36), is a thus curve extending over only a finite midpoint range of length $2h$ because its edges become vertical asymptotes. The trajectory is shown in Figure 2.18 with the input and output points labeled, in analogy with zero-offset migration. Because of the steepness of the curve as it approaches its ends, the DMO operator is typically cut-off to avoid aliasing. This is shown in Figure 2.18 by arrows marking a smaller aperture that avoids aliasing.

The equation for the traveltime of a generally dipping reflector embedded in a constant velocity medium is (Dunkin & Levin, 1973)

$$t_{ref}^2(x) = T_0^2 + \frac{4h^2}{v^2} - p^2h^2. \tag{2.37}$$

where p is the time dip of the reflection from equation (2.14) and v is the medium velocity. From equation (2.37), a dipping reflector has a moveout velocity v_{app} that differs from that for a horizontal reflector

$$v_{app} = \sqrt{\frac{v^2}{1 - p^2v^2/4}} = \frac{v}{\cos\theta}. \tag{2.38}$$

In equation (2.37), we parameterize the zero-offset time T_0 as

$$T_0 = px + C, \tag{2.39}$$

where C is a constant to be determined momentarily. Note that, for a horizontal reflector ($\theta = 0°$ and $p = 0$), equations (2.37) and (2.39) indicate that the reflector in a common-offset section is at a constant time. Also, because of the T_0^2 term in equation (2.37), the reflection from a planar dipping reflector has curvature in a common-offset section. Bear in mind also, since the ouput of DMO is a zero-offset section, $t_{out} = T_0$.

Building on equation (2.37), we obtain the equation for the reflection from a generally dipping reflector after NMO-correction, denoted $t_{refn}(x)$:

$$t_{refn}(x) = \sqrt{(px + C)^2 + \frac{4h^2}{v^2} - p^2h^2 - \frac{4h^2}{v_{st}^2}}. \tag{2.40}$$

Now, the constant C can be determined via the relationship $t_{refn}(x_{in}) = t_{in}$. This equality simply states that the input to the DMO process (the input points x_{in} and t_{in}) lie on the NMO-corrected reflection curve. Substituting $t_{refn}(x_{in}) = t_{in}$ into equation (2.40) and solving for C results in

$$C = \sqrt{t_{in}^2 + p^2h^2 + 4h^2\left(\frac{1}{v_{st}^2} - \frac{1}{v^2}\right)} - px_{in}. \tag{2.41}$$

Inserting this expression for C into equation (2.40), the NMO-corrected reflection time can be written in terms of the input points

$$t_{refn}(x) = \sqrt{\left(p(x - x_{in}) + \sqrt{t_{in}^2 + p^2h^2 + 4h^2\left[\frac{1}{v_{st}^2} - \frac{1}{v^2}\right]}\right)^2 - p^2h^2 - 4h^2\left[\frac{1}{v_{st}^2} - \frac{1}{v^2}\right]}. \tag{2.42}$$

With equations (2.36) and (2.42) in hand, the two map-DMO relations can be obtained by setting $t_{refn}(x) = t_{dmo}(x)$ and $\partial t_{refn}(x)/\partial x = \partial t_{dmo}(x)/\partial x$ at the input point $x = x_{in}$. By map-DMO, we mean to make an analogy to equations (2.17) and (2.18), which we referred to as the equations used for *map-migration.* In addition to these two relations, the time shifts necessary for a stationary phase evaluation of DMO, appearing in equation (2.34), are known. Actually, the two conditions $t_{refn}(x) = t_{dmo}(x)$ and $\partial t_{refn}(x)/\partial x = \partial t_{dmo}(x)/\partial x$ at $x = x_{in}$ follow from the fact that the input point is a stationary point. The stationary phase approximation, equation (2.9), requires the evaluation of the second derivatives, with respect to x, of $t_{refn}(x)$ and $t_{dmo}(x)$ at the stationary point, $x = x_{in}$.

The first condition, $t_{refn}(x) = t_{dmo}(x)$ at $x = x_{in}$, gives the DMO ellipse, equation (2.35), in the form

$$\frac{t_{out}^2}{t_{in}^2} + \frac{(x_{in} - x_{out})^2}{h^2} = 1. \tag{2.43}$$

From the second condition, $\partial t_{refn}(x)/\partial x = \partial t_{dmo}(x)/\partial x$ at at $x = x_{in}$, we get a new relation

$$x_{in} - x_{out} = \frac{\sqrt{t_{in}^2 + 4\tilde{p}^2h^2} - t_{in}}{2\tilde{p}}, \tag{2.44}$$

where $\tilde{p}$ is given by

$$\tilde{p} = p\frac{t_{out}}{t_{in}}. \tag{2.45}$$

The derivation of equations (2.44) and (2.45) is detailed in Appendix A. In addition, since the input to DMO is already NMO-corrected,

$$t_{in} = \sqrt{t_{out}^2 + 4h^2\left(\frac{1}{v^2} - \frac{1}{v_{st}^2}\right) - p^2h^2}, \tag{2.46}$$

where this relationship follows from equations (2.39) and (2.40) since $T_0 = t_{out}$ (the output of DMO is a zero-offset section) and $t_{refn}(x_{in}) = t_{in}$ (the input to DMO has been NMO-corrected). Equation (2.44) is a direct analogy to equation (2.18) for DMO instead of zero-offset migration. Substituting the DMO ellipse, equation (2.35), into equation (2.44) for $x_{in} - x_{out}$ gives the analogy to equation (2.17) for DMO

$$t_{out} = t_{in}\sqrt{\frac{t_{in}}{2\tilde{p}^2h^2}\left[\sqrt{t_{in}^2 + 4\tilde{p}^2h^2} - t_{in}\right]}. \tag{2.47}$$

The derivation of equation (2.47) is detailed in Appendix A. From equations (2.44) and (2.47), given x_{in} and t_{in}, x_{out} and t_{out} can be found. Hence, equations (2.44) and (2.47) summarize the mapping performed by DMO.

The stationary phase approximation is now in order. This type of analysis, when applied to DMO, yields the form of the inverse filter needed to reverse the wavelet-altering and amplitude-changing aspects of summation along the DMO-trajectory. Repeating the previous sections of this chapter, the DMO response $I(\omega)$ can be approximately given by

$$I(\omega) = \sqrt{2\pi}e^{i\pi/4}\left[\frac{\partial^2\phi}{\partial x^2}\right]_{x=x_{in}}^{-1/2} e^{i\phi(x_{in})}, \tag{2.48}$$

with x_{in} the stationary point of the phase function $\phi(x)$, which for DMO is

$$\phi(x) = \omega[t_{refn}(x) - t_{dmo}(x)]. \tag{2.49}$$

Note that, for this application (and the others in this chapter), $\phi(x_{in}) = 0$, so that the last exponential factor in equation (2.48) is unity.

From equations (2.48) and (2.49), the second derivatives of $t_{dmo}(x)$ and $t_{refn}(x)$ with respect to x are needed at $x = x_{in}$. From the expression for $t_{refn}(x)$, equation 2.42, I find that, when the stacking velocity is equal to the true velocity ($v_{st} = v$),

$$\frac{\partial^2 t_{refn}(x)}{\partial x^2}|_{x=x_{in}} = -\frac{p^4h^2}{t_{in}^3}. \tag{2.50}$$

The derivation of equation (2.50) is detailed in Appendix A. Equation (2.50) can be rewritten in terms of t_{in}, h, and t_{out} instead of t_{in}, h, and p with some albegraic manipulation. Using equation (2.45) to write the right-hand side of equation (2.47) in terms of t_{in}, h, t_{out}, and p, and then solving for p yields

$$p = \frac{t_{in}}{h}\sqrt{(t_{in}/t_{out})^2 - 1}. \tag{2.51}$$

The derivation of equation (2.51) is detailed in Appendix A. Putting this expression for p into equation (2.50) gives

$$\frac{\partial^2 t_{refn}(x)}{\partial x^2}|_{x=x_{in}} = -\frac{t_{in}}{h^2}\left[\left(\frac{t_{in}}{t_{out}}\right)^2 - 1\right]^2. \tag{2.52}$$

The derivation of equation (2.52) is detailed in Appendix A.

Turning now to the second derivative of $t_{dmo}(x)$, given in equation (2.36), we find that

$$\frac{\partial^2 t_{dmo}(x)}{\partial x^2}|_{x=x_{in}} = \left[1 - \frac{(x_{in} - x_{out})^2}{h^2}\right]^{-5/2} \frac{t_{out}}{h^2}\left(2\frac{(x_{in} - x_{out})^2}{h^2} + 1\right). \tag{2.53}$$

The derivation of equation (2.53) is detailed in Appendix A. Using the DMO ellipse, equation (2.43), to substitute for $(x_{in} - x_{out})$ in the above equation results in

$$\frac{\partial^2 t_{dmo}(x)}{\partial x^2}|_{x=x_{in}} = \frac{t_{in}}{h^2}\left(\frac{t_{in}}{t_{out}}\right)^2\left[3\left(\frac{t_{in}}{t_{out}}\right)^2 - 2\right]. \tag{2.54}$$

The derivation of equation (2.54) is detailed in Appendix A.

Since both expressions for the second derivatives of $t_{refn}(x)$ and $t_{dmo}(x)$ are now known at $x = x_{in}$, the second derivative of the phase function appearing in equation (2.48) can be computed. From equation (2.49),

$$\frac{\partial^2 \phi}{\partial x^2}|_{x=x_{in}} = \omega\left[\frac{d^2 t_{refn}(x)}{dx^2}|_{x=x_{in}} - \frac{d^2 t_{dmo}(x)}{dx^2}|_{x=x_{in}}\right]. \tag{2.55}$$

Using the results of equations (2.52) and (2.54),

$$\frac{\partial^2 \phi}{\partial x^2}|_{x=x_{in}} = -\omega\frac{t_{in}}{h^2}\left[2\left(\frac{t_{in}}{t_{out}}\right)^2 - 1\right]^2. \tag{2.56}$$

Substituting this expression into equation (2.48) gives the DMO response $I(\omega)$

$$I(\omega) = \sqrt{2\pi}e^{i\pi/4}\left[-\omega\frac{t_{in}}{h^2}\left[2\left(\frac{t_{in}}{t_{out}}\right)^2 - 1\right]^2\right]^{-1/2}. \tag{2.57}$$

This expression can be put in a more compact and understandable form:

$$I(\omega) = \frac{h}{2(t_{in}/t_{out})^2 - 1} \; \frac{\exp(-i\pi/4)}{\sqrt{\omega}} \; \sqrt{\frac{2\pi}{t_{in}}}. \tag{2.58}$$

By multiplying the result of the DMO summation by the inverse of equation (2.58) in the frequency domain, given by

$$I^{-1}(\omega) = \frac{2(t_{in}/t_{out})^2 - 1}{h} \; \sqrt{\omega}\, \exp(i\pi/4) \; \sqrt{\frac{t_{in}}{2\pi}}, \tag{2.59}$$

the artificial changes produced by DMO can be removed. This inverse filter contains three correction terms that, in analogy with the correction terms discussed for zero-offset migration, can be called the *DMO obliquity factor*, the *wavelet shaping factor*, and the *geometric spreading factor*, respectively. The DMO obliquity factor contains terms with t_{in}, t_{out}, and h. The wavelet shaping factor contains the square-root of frequency and a $\pi/4$ phase shift. The geometric spreading factor shows up as the square-root of t_{in}. Black *et al.* (1993) have previously derived this filter in their paper on DMO and true-amplitude imaging. The only difference between their filter shown in their equation 44 and the one we have derived here is that their geometric speading factor is $\sqrt{t_{out}}$ instead of $\sqrt{t_{in}}$ - it is in terms of the output point and not the input point. This is surprising since, recalling the geometric-spreading correction discussed in the previous section, it is given in terms of the input point in the case of zero-offset migration (Yilmaz, 1987). This discrepancy could arise because Black *et al.* (1993) derived their inverse filter in the context of impulse-response superposition instead of the diffraction-summation approach taken here (Yilmaz, 1987). Therefore, by analogy, the geometric spreading factor discussed in the section on zero-offset migration should be changed to the output point for migration by impulse-response superposition.

2.7 The stack response for a dipping reflector

With the results of the previous section on the DMO response, the stacking response discussed at the beginning of this chapter can be generalized to the case of a dipping reflector. Recall that the time delays, equation 2.34, were based on there being only an NMO correction applied to the data. In this section, we find the time delays from the combined application of NMO and DMO (see Figure 2.19). We then verify that the stacking response for a dipping reflector has the exact same form as encountered earlier in equation (2.13). The main difference, though, is that the zero-offset time T_0 appearing in equation (2.13) is larger by a factor of $1/\cos\theta$ for a reflector with a dip θ. Hence, the amplitude of the stacking response scales with $\sqrt{T_0} \sim \sqrt{\sec\theta}$, which becomes larger as a reflector dip increases. This scaling of stacked amplitude can be thought of as a *geometric spreading factor*, like that encountered in the corrections applied to zero-offset migration and DMO, which is not corrected for since the error in the stacking velocity is unknown.

To obtain the combined time shift caused by the application of both NMO and DMO, only the DMO time shift is missing since the NMO time shift has already been given in

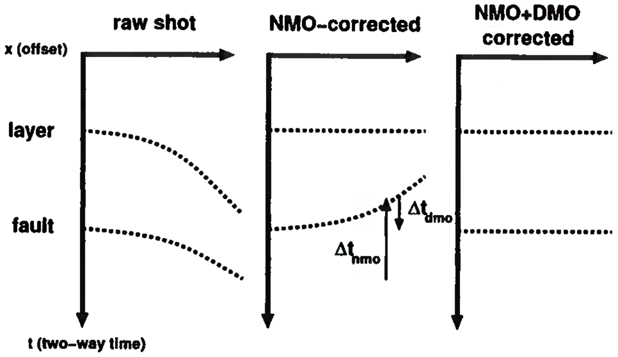

Figure 2.19. The NMO and DMO time shifts in a common-midpoint gather for a reflection from a horizontal interface and one from a dipping fault-plane reflection.

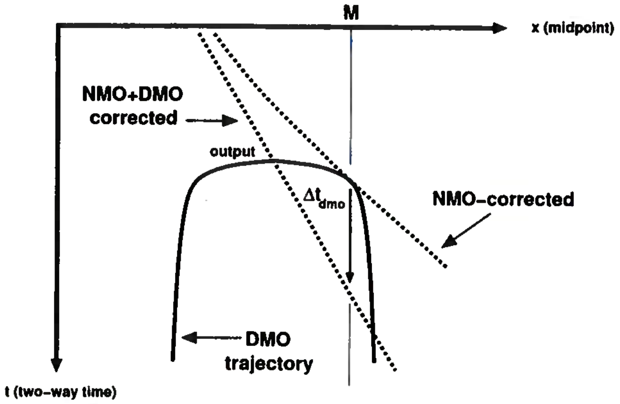

Figure 2.20. The DMO time shift in a common-offset gather. Like migration, DMO steepens dipping events, which causes an apparent time shift, Δt_{dmo}, at a particular midpoint location, here labeled M. Compare this figure to Figure 2.19.

the first section of this chapter, equation (2.2). The total time shift is given by the sum of the NMO and DMO time shifts $\Delta t(x) = \Delta t_{nmo} + \Delta t_{dmo}$. It turns out that the NMO and DMO time shifts are opposite in sign (see Figure 2.19). From equation (2.39), the curve for a dipping reflector in a zero-offset section is a straight line. Suppose that this line, $t_0(x)$, contains the output points, x_{out} and t_{out}, of a DMO process

$$t_0(x) = p(x - x_{out}) + t_{out}, \tag{2.60}$$

where again p is the time dip of the reflector. From the map-DMO equations of the previous section, equations (2.44) and (2.47), the output points can be expressed in terms of the input points

$$t_0(x) = p(x - x_{out}(x_{in}, t_{in})) + t_{out}(t_{in}). \tag{2.61}$$

To find the reflection time after DMO at a particular midpoint location in a common-offset gather, $t_0(x)$ should be evaluated at $x = x_{in}$, with x_{in} shown as M in Figure 2.20:

$$t_0(x_{in}) = p(x_{in} - x_{out}(x_{in}, t_{in})) + t_{out}(t_{in}). \tag{2.62}$$

Substituting the expressions for $(x_{in} - x_{out})$ and t_{out} given in equations (2.44) and (2.47) yields

$$t_0(x_{in}) = p\frac{\sqrt{t_{in}^2 + 4\tilde{p}^2h^2} - t_{in}}{2\tilde{p}} + t_{in}\sqrt{\frac{t_{in}}{2\tilde{p}^2h^2}\left[\sqrt{t_{in}^2 + 4\tilde{p}^2h^2} - t_{in}\right]}. \tag{2.63}$$

To get the time shift performed by DMO at this midpoint location, the input time needs to be subtracted from equation (2.63); this is the DMO time shift:

$$\Delta t_{dmo} = t_0(x_{in}) - t_{in} = p\frac{\sqrt{t_{in}^2 + 4\tilde{p}^2h^2} - t_{in}}{2\tilde{p}} + t_{in}\sqrt{\frac{t_{in}}{2\tilde{p}^2h^2}\left[\sqrt{t_{in}^2 + 4\tilde{p}^2h^2} - t_{in}\right]} - t_{in}. \tag{2.64}$$

Note that the DMO time shift depends on stacking velocity through the parameters t_{in} and $\tilde{p}$. This is in contrast to the notion that DMO is a velocity-independent process. Though the shape of the DMO ellipse and the DMO trajectory do not change with changing velocity, the time shift that DMO applies at a particular midpoint location is dependent on how much that sample has been NMO-corrected prior to application of DMO.

The total time shift is the sum of the NMO and DMO time shifts

$$\begin{aligned}\Delta t(x) = {} & \sqrt{T_0^2 + 4h^2\left(\frac{1}{v^2} - \frac{1}{v_{st}^2}\right) - p^2h^2} \quad - \quad T_0 + \\ & p\frac{\sqrt{t_{in}^2 + 4\tilde{p}^2h^2} - t_{in}}{2\tilde{p}} \quad + \quad t_{in}\sqrt{\frac{t_{in}}{2\tilde{p}^2h^2}\left[\sqrt{t_{in}^2 + 4\tilde{p}^2h^2} - t_{in}\right]} \quad - \quad t_{in},\end{aligned} \tag{2.65}$$

which can be simplified with the help of equation (2.46) to

$$\Delta t(x) = p\frac{\sqrt{t_{in}^2 + 4\tilde{p}^2 h^2} - t_{in}}{2\tilde{p}} \quad + \quad t_{in}\sqrt{\frac{t_{in}}{2\tilde{p}^2 h^2}\left[\sqrt{t_{in}^2 + 4\tilde{p}^2 h^2} - t_{in}\right]} \quad - \quad T_0. \tag{2.66}$$

This equation is the generalization of equation (2.2) for a dipping reflector. The stationary phase approximation can be applied to the time-shift function in equation (2.66) as was done in the earlier section of this chapter on stacking. The result for the stack response of a dipping reflector $I(\omega)$ looks superficially the same

$$I(\omega) = v_{st}\sqrt{\frac{2\pi T_0}{\omega}}\frac{\exp(i\ \mathrm{sgn}(v_{st} - v)\pi/4)}{\mid \sqrt{1 - (v_{st}/v)^2} \mid}, \tag{2.67}$$

except that the zero-offset time T_0 appearing here is for a dipping reflector. If T_{mig} is the migration (vertical) time, then $T_{mig} = T_0/\cos\theta$ where θ is the dip. The scaling of the amplitude response with $\sqrt{\sec\theta}$ explains the numerical observation that the amplitude of the fault-plane reflections is less sensitive to stacking velocity errors than for the horizontal reflections within the stationary phase approximation. A similar amplitude factor exists for prestack migration, reflecting the fact that the prestack diffraction curve becomes flatter at longer offsets and hence that the summation collects more energy during its time spent near the stationary point. The prestack migration response is discussed in Appendix B.

2.8 Discussion

The entire seismic processing sequence consisting of NMO, DMO, stack, and zero-offset migration has been analyzed with the tool of stationary phase. The issues concerning errors in imaging caused by errors in stacking and migration velocities should serve as a guide for interpretation of post-stack seismic images, in order to assess what can realistically be gleened from these images. With a numerical example, we find that the reflected waveform from the fault plane is less sensitive to stacking-velocity errors than that from the horizontal interfaces. This certainly holds true for the model, but perhaps even more generally, as indicated by the scaling of the amplitude response within the stationary phase approximation. Additional processing steps not covered in this chapter, such as muting, also influence the stack response. Since muting selects a larger offset range with increasing time and fault-plane reflections have a larger two-way reflection time than reflections from horizontal interfaces, a fault-plane reflection should have a larger pre-stack offset range than does the reflection from a horizontal interface at the same depth. Muting did not affect the numerical results in this chapter since the muting happened to be chosen in such a way that no new offsets arose in the CMP-gathers from the time of the horizontal interface reflection until that of the fault-plane reflection. Introducing more offsets into the stacked fault-plane reflections should make them more sensitive to stacking errors while making them more robust in the presence of random noise. At the least, it can be said that fault-plane reflections, when gathered in well-sampled dip lines, are not any more susceptible to stacking errors than are reflections from layer boundaries with gentle dip.

Chapter 3

Finite-element modeling of slip-discontinuities in layered media

3.1 Summary

Interfaces in elastic media need not be in welded contact. For instance, fractures allow a small amount of slip to occur along their surfaces during the passage of a seismic wave. By slip, we mean that the displacement across the interface can be discontinuous. Reflection and transmission of plane waves at plane boundaries in this case are frequency dependent.

Previous numerical studies have chosen the finite-difference method to simulate slip discontinuities. That approach suffers from difficulties in incorporating boundary conditions into the strong form of the equations of motion. We show that a method based on the weak-formulation, e.g., the finite-element method, can overcome these problems. Numerical examples illustrate the method for a P-wave incident at a non-normal angle of incidence.[1]

3.2 Introduction

Full-waveform forward modeling in seismology has traditionally been dominated by finite-difference methods. Perhaps the intuitive appeal of such methods has led to their popularity. Kelly & Marfurt (1990), in reviewing the numerical literature from the exploration geophysics community, cited at least four possible reasons for the relative neglect of other methods, specifically finite-elements. We complement their list by stating that finite-elements require additional numerical care for proper implementation. For instance, explicit finite-difference algorithms do not require the inversion of a matrix. In contrast, all finite-element methods eventually lead to a matrix equation that must be solved. Avoiding the solution of a matrix equation in a finite-element scheme requires a numerical trick called "mass-lumping" wherein the rows of the mass matrix are summed and placed on the diagonal (Zienkiewicz & Taylor, 2000).

Finite-elements offer more flexibility than do finite-differences with respect to the shape of the numerical mesh; however, it is less widely accepted that finite-elements are superior to finite-differences in the way they account for boundary conditions. Such an advantage can easily be seen in the formula for integration by parts: an integral is replaced by another integral *and* a term representing the values of the function at the boundaries. This basic

---

[1] To be submitted after being generalized to poroelastic media

fact shows up in the formulation of finite-elements since they approximate the integrated, or weak, equations of motion and thereby utilize integration by parts, or its higher-dimensional generalization, Green's Theorem.

Finite-differences, as approximations to the strong, or differential, form of the equations of motion, require *ad hoc* techniques to take into account, for instance, a welded boundary between two different elastic media. David Boore, one of the pioneers of the finite-difference method in seismology, summarized the problem by stating that in finite-difference schemes "the interface displacements must satisfy the continuity of displacement and stress, but are not explicitly required to satisfy the equation of motion" (Boore, 1970).

The motivation of this chapter is to explore the advantages of the finite-element method for the modeling of slip discontinuities. The slip discontinuity has been proposed by Schoenberg (1980) as an interface condition applicable to cracks. The boundary condition can be thought of as a generalized interface condition since it supplies a parameter, the compliance η, that, over its range of physical values, takes an elastic interface from a welded contact ($\eta = 0$) to a free surface ($\eta = \infty$). Mathematically, the boundary condition for an SH-wave incident on a slip discontinuity situated in the yz-plane is expressed as

$$u_y^+ - u_y^- = \eta\sigma_{yz}, \tag{3.1}$$

$$\sigma_{yz}^+ - \sigma_{yz}^- = 0, \tag{3.2}$$

where (-) refers to the side of the interface on which the wave is incident, (+) the other side of the interface, u_y refers to the displacement normal to the plane of propagation, and σ_{yz} is the shear stress. In this paper, a slip discontinuity extends infinitely; we do not consider crack-tips. Physically, boundary conditions (3.1) and (3.2) model the transmission and reflection of a thin, low-shear zone (Schoenberg, 1980). Faults generally fall within this category.

In this chapter, we demonstrate that:

1. Finite-element modeling can explicitly incorporate interface boundary conditions into the equations of motion.
2. The equations of motion for the numerical scheme can be the familiar second-order wave equation in u (displacement).
3. An explicit, conditionally stable time integration scheme can handle the zero-length elements needed to accurately model a slip discontinuity.

We conclude this discussion of the finite-element method with numerical examples of the reflection and transmission of plane P-waves at an elastic interface and a slip discontinuity.

3.3 A Finite-Element Scheme for the 1D Scalar Wave Equation

The beginning of any numerical study must be an analysis of the two limitations imposed on finite systems: numerical dispersion and stability. An understanding of these

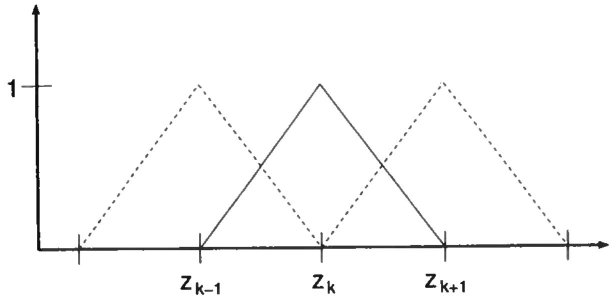

Figure 3.1. The basis functions we use for finite-elements

concepts should steer the subsequent implementation of a particular numerical scheme. Ideally, any numerical simulation should satisfy a stability criterion with the least amount of dispersion possible.

In this section, we present the most simple case: a finite-element implementation of the scalar wave equation in 1D. We choose this problem since, in 1D, the essence of the finite-element scheme is not complicated by mesh generation or subsequent *assembly* of the mass or stiffness matrix. Assembly of these matrices is directly related to the notion of wrapping up, or ordering, a higher-dimensional set of points into a 1D vector. In 1D, this is unnecessary.

Consider the 1D scalar wave equation with source term in a homogeneous medium

$$c^2\frac{\partial^2 u}{\partial z^2} - \frac{\partial^2 u}{\partial t^2} - s = 0, \tag{3.3}$$

where c is the wave speed (assumed constant), s is the source term, z is depth, and t is time. For this example, we assume Dirichlet (essential) boundary conditions at $z = 0$ and $z = L$. The displacement, u, is approximated by a finite series of spatial basis functions with coefficients that depend on time

$$u(z,t) = \sum_{K=1}^{N} \alpha_K(t)\phi_K(z). \tag{3.4}$$

In this paper, the nodal basis will always be used. For a spatial discretization step h and a uniform partition of the interval [0,L] into $N+1$ subintervals, these basis functions are mathematically defined as

$$\phi_K(z) = \begin{cases} (z - z_{K-1})/h & \text{if } z_{K-1} \le z \le z_K, \\ (z_{K+1} - z)/h & \text{if } z_K \le z \le z_{K+1}, \\ 0 & \text{otherwise.} \end{cases} \tag{3.5}$$

Figure 3.1 shows these piecewise linear functions graphically.

The Galerkin formulation of the finite-element method seeks to minimize the weighted average of the error in satisfying equation (3.3) induced by the incompleteness of the finite set of basis functions in equation (3.5). The essence of the Galerkin method is that it weights the errors with the same basis functions used in the approximation of the displacement, u (Marfurt, 1984)

$$\int_0^L \left[c^2 \frac{\partial^2}{\partial z^2} \sum_{K=1}^{N} \alpha_K(t)\phi_K(z) - \right.$$
$$\left. \frac{\partial^2}{\partial t^2} \sum_{K=1}^{N} \alpha_K(t)\phi_K(z) - s \right] \phi_J(z)dz = 0$$
$$\text{for } J=1,2,...,N. \tag{3.6}$$

Rearranging the order of the sums and integrals in this equation yields

$$0 = -c^2 \sum_{K=1}^{N} \alpha_K \left[\int_0^L \frac{\partial^2 \phi_K}{\partial z^2} \phi_J dz \right] +$$
$$\sum_{K=1}^{N} \frac{\partial^2 \alpha_K}{\partial t^2} \left[\int_0^L \phi_K \phi_J dz \right] + \int_0^L s\phi_J dz. \tag{3.7}$$

Since the basis functions are piecewise linear over their range, the first integral on the r.h.s. of equation (3.7), containing a second derivative of the basis function, must be altered (Haltiner & Williams, 1980). In altering this term by integrating by parts, boundary terms appear explicitly in the equation of motion

$$\int_0^L \frac{\partial^2 \phi_K}{\partial z^2} \phi_J dz = \left. \frac{\partial \phi_K}{\partial z} \phi_J \right|_0^L - \int_0^L \frac{\partial \phi_K}{\partial z} \frac{\partial \phi_J}{\partial z} dz. \tag{3.8}$$

To implement Dirichlet boundary conditions at $z = 0$ and $z = L$, the weighting function, ϕ_J, is set to zero at the boundaries (Wang, 2000b). Hence, the boundary term in equation (3.8) disappears and the elements ϕ are fixed to be zero on the boundaries. More complicated boundary conditions, such as absorbing boundary conditions, are discussed later.

Without the boundary term, inserting equation (3.8) into equation (3.7) yields the weak form of the scalar wave equation

$$0 = c^2 \sum_{K=1}^{N} \alpha_K \left[\int_0^L \frac{\partial \phi_K}{\partial z} \frac{\partial \phi_J}{\partial z} dz \right] +$$

$$\sum_{K=1}^{N} \frac{\partial^2 \alpha_K}{\partial t^2} \left[\int_0^L \phi_K \phi_J dz \right] + \int_0^L s \phi_J dz. \tag{3.9}$$

The bracketed terms in equation (3.9) can be represented as matrices multiplying the vectors $\vec{\alpha}$ and $\partial^2 \vec{\alpha}/\partial t^2$. The matrix multiplying the second time derivative, $\partial^2 \vec{\alpha}/\partial t^2$, is called the *mass matrix*, M, and the matrix acting on $\vec{\alpha}$ is referred to as the *stiffness matrix*, S. From equation (3.5), the entries of these matrices can be calculated exactly. For the mass matrix, $M_{K,J}$, the nonzero entries are

$$\int_0^L \phi_K \phi_J dz = 2h/3 \qquad \text{for } K = J \tag{3.10}$$

$$\int_0^L \phi_K \phi_J dz = h/6 \qquad \text{for } K = J+1, J-1. \tag{3.11}$$

Thus, M is symmetric and tridiagonal. Similarly, the stiffness matrix, $S_{K,J}$, is also symmetric tridiagonal, with nonzero entries

$$\int_0^L \frac{\partial \phi_K}{\partial z} \frac{\partial \phi_J}{\partial z} dz = 2/h \qquad \text{for } K = J \tag{3.12}$$

$$\int_0^L \frac{\partial \phi_K}{\partial z} \frac{\partial \phi_J}{\partial z} dz = -1/h \qquad \text{for } K = J+1, J-1. \tag{3.13}$$

The finite-element scheme can now be written in matrix form

$$0 = c^2 S \vec{\alpha} + M \frac{\partial^2 \vec{\alpha}}{\partial t^2}. \tag{3.14}$$

Note that the source term has been omitted in equation (3.14). To include a source term, s has to be approximated in the nodal basis

$$s(z,t) = \sum_{K=1}^{N} s_K(t) \phi_K(z). \tag{3.15}$$

Substituting this into equation (3.9), it can be verified that the mass matrix multiplies the source vector s_K.

3.4 Stability analysis of an explicit finite-element scheme

The finite-element approach integrates the above matrix equation in space, but a suitable time integration scheme has yet to be determined. As a first example, we use an explicit time integration known as *central differences* (Zienkiewicz & Taylor, 2000) to approximate the time behavior of $\vec{\alpha}$

$$0 = c^2 S\vec{\alpha}_n + M\left(\frac{\vec{\alpha}_{n+1} - 2\vec{\alpha}_n + \vec{\alpha}_{n-1}}{\Delta t^2}\right), \tag{3.16}$$

where the subscripts refer to the time step $n+1$, to be calculated, and the previous time steps n and $n-1$. The time discretization interval is Δt. Notice that equation (3.16) is symmetric in the $n+1$ and $n-1$ terms. This ensures that the resulting dispersion relation on the numerical grid is real-valued. Such a property is desirable since a complex dispersion relation would yield solutions to the wave equation that grow or decay exponentially with distance. In contrast, real-valued solutions do not grow exponentially, so long as they satisfy a stability criterion.

To calculate the stability criterion for this explicit time integration scheme, first use equations (3.10), (3.11), (3.12), and (3.13) to carry out the matrix multiplications in equation (3.16). What results is the so-called *finite-element stencil*

$$\begin{aligned} 0 \quad = \quad & \frac{h}{6\Delta t^2}\alpha_{m-1,n+1} + \frac{2h}{3\Delta t^2}\alpha_{m,n+1} + \\ & \frac{h}{6\Delta t^2}\alpha_{m+1,n+1} - \left(\frac{h}{3\Delta t^2} + \frac{c^2}{h}\right)\alpha_{m-1,n} - \\ & \left(\frac{4h}{3\Delta t^2} - \frac{2c^2}{h}\right)\alpha_{m,n} - \left(\frac{h}{3\Delta t^2} + \frac{c^2}{h}\right)\alpha_{m+1,n} + \\ & \frac{h}{6\Delta t^2}\alpha_{m-1,n-1} + \frac{2h}{3\Delta t^2}\alpha_{m-1,n-1} + \\ & \frac{h}{6\Delta t^2}\alpha_{m-1,n-1}, \end{aligned} \tag{3.17}$$

where the first subscripts refer to gridpoints in space and the second subscripts are still the time steps. To investigate the stability of the central difference scheme, insert a harmonic function for α (Alterman & Loewenthal, 1970):

$$\alpha_{m,n} = e^{ikmh}\zeta^n \qquad \zeta = e^{b\Delta t},\ z = mh, \text{ and } t = n\Delta t, \tag{3.18}$$

where the integers m and n multiply the spatial and temporal interval lengths h and Δt, k is the wavenumber, and b is related to the frequency.

Inserting equation (3.18) into equation (3.17), and organizing terms yields

$$\begin{aligned} 0 \;=\; & \Big[\frac{h}{6\Delta t^2}(e^{-ikh}+4+e^{ikh})\zeta^2 \\ & -\frac{c^2}{h}(e^{-ikh}-2+e^{ikh})\zeta \\ & -\frac{h}{3\Delta t^2}(e^{-ikh}+4+e^{ikh})\zeta \\ & +\frac{h}{6\Delta t^2}(e^{-ikh}+4+e^{ikh}) \Big] e^{ikmh}\zeta^{n-1}. \end{aligned} \tag{3.19}$$

In order to have non-trivial solutions, the terms inside the brackets in equation (3.19) must equal zero. The resulting equation contains all the information about the dispersion and stability properties of the numerical scheme. Note that in higher dimensions, equation (3.19) is a matrix equation, and the condition for non-trivial solutions is that the determinant of the matrix equals zero.

Dividing equation (3.19) by the coefficient of the ζ^2 term and setting the terms inside the brackets to zero gives

$$0 = \zeta^2 - \frac{6c^2\Delta t^2}{h^2}\left(\frac{e^{-ikh}-2+e^{ikh}}{e^{-ikh}+4+e^{ikh}}\right)\zeta - 2\zeta + 1. \tag{3.20}$$

Using the Euler formula and the relation $\cos(kh) - 1 = -2\sin^2(kh/2)$, we can simplify equation (3.20),

$$0 = \zeta^2 - \left[\frac{\frac{2h}{\Delta t^2} - \left(\frac{4c^2}{h} + \frac{4h}{3\Delta t^2}\right)\sin^2(kh/2)}{\frac{h}{\Delta t^2} - \frac{2h}{3\Delta t^2}\sin^2(kh/2)}\right]\zeta + 1. \tag{3.21}$$

For the numerical scheme to be stable, the roots of equation (3.21) should have magnitudes less than or equal to 1. This means that the solutions are not exponentially growing in time. For a quadratic of the form

$$0 = x^2 - zx + 1, \tag{3.22}$$

the magnitude of the two roots, x_1 and x_2, are both less than or equal to 1 if

$$-1 \le \frac{z}{2} \le 1. \tag{3.23}$$

Inserting equation (3.21) into this expression yields

$$-1 \le \frac{\frac{2h}{\Delta t^2} - \left(\frac{4c^2}{h} + \frac{4h}{3\Delta t^2}\right)\sin^2(kh/2)}{2(\frac{h}{\Delta t^2} - \frac{2h}{3\Delta t^2}\sin^2(kh/2))} \le 1. \tag{3.24}$$

Scanning over all possible values of $\sin^2(kh/2)$, the strongest condition on the spatial and temporal discretizations h and Δt occurs when $\sin^2(kh/2) = 1$ (Alterman & Loewenthal, 1970). In this case, equation (3.24) becomes

$$-1 \leq \frac{\frac{2h}{3\Delta t^2} - \frac{4c^2}{h}}{\frac{2h}{3\Delta t^2}} \leq 1. \tag{3.25}$$

From equation (3.25), the right-hand inequality,

$$\frac{2h}{3\Delta t^2} - \frac{4c^2}{h} \leq \frac{2h}{3\Delta t^2}, \tag{3.26}$$

is trivially true. The left-hand inequality provides a more meaningful relation:

$$\begin{aligned} -\frac{2h}{3\Delta t^2} &\leq \frac{2h}{3\Delta t^2} - \frac{4c^2}{h}, \\ \text{or} \quad \frac{4c^2}{h} &\leq \frac{4h}{3\Delta t^2}, \\ \text{or} \quad c\Delta t\sqrt{3} &\leq h. \end{aligned} \tag{3.27}$$

This is the Courant-Friedrichs-Levy (CFL) stability condition for this implementation of explicit finite elements (Marfurt, 1984).

Above, we stated that equation (3.19) contains all the information about the dispersion and stability properties of the numerical scheme. We have the stability condition - what about the dispersion relation? To obtain this, set b in equation (3.18) to $i\omega$ so that $\zeta = e^{i\omega\Delta t}$. Substituting this into equation (3.19), setting the terms in the brackets to zero, and simplifying a bit yields the dispersion relation

$$\cos(\omega\Delta t) = 1 + \frac{3\Delta t^2 c^2}{h^2}\left(\frac{\cos(kh) - 1}{\cos(kh) + 2}\right). \tag{3.28}$$

For wavelengths much larger than the grid-spacing, $\omega\Delta t$ and kh are small parameters. Keeping the lowest order terms in a series expansion of equation (3.28) gives the familiar dispersion relation

$$\omega^2 = c^2k^2. \tag{3.29}$$

In other words, the finite-element scheme should do an excellent job propagating waves well-sampled by the numerical grid. In practice, ten grid samples per wavelength is adequate for avoiding numerical dispersion.

A finite-element method can be fitted with absorbing boundaries at the edges of the numerical grid. For the 1D case of layered media, Clayton-Enquist boundary conditions (or radiation boundary conditions) can be constructed that absorb any outward-going waves (Clayton & Enquist, 1977). In higher dimensions, this approach fails and other techniques, most notably the perfectly matched layer (PML) method, must be employed (Chew & Liu, 1996). If we take the numerical domain to extend from $z = 0$ to $z = L$, a discrete one-way wave equation at the boundary $z = 0$ is

$$\frac{u(0,t) - u(0,t-\Delta t)}{\Delta t} = c\frac{u(h,t-\Delta t) - u(0,t-\Delta t)}{h}, \tag{3.30}$$

We require that the velocity is constant, $c(z) = c$, for the boundary point and the nearest interior grid-point. Equation (3.30) can be rearranged to solve for $u(0,t)$, the displacement on the boundary, as a function of the displacement at the boundary at the previous time step, $u(0,t-\Delta t)$, and the displacement at the nearest interior grid-point at the previous time step, $u(h,t-\Delta t)$. Hence, the absorbing boundary condition is explicit in time. Slight boundary reflections occur because of interpolation errors in the derivatives in equation (3.30). We can dampen these interpolation errors further by using second-order approximations to the derivatives in equation (3.30) instead of the first-order derivatives shown.

3.5 The *P*-*SV* system in layered media

Of more interest to seismic surveys is the reflection and transmission of $P-SV$ waves at a slip discontinuity. Two compliances, the normal and tangential compliances (η_N and η_T), characterize a crack in this case. Analogous to equations (3.1) and (3.2), the interface boundary conditions are

$$u_x^+ - u_x^- = \eta_T \sigma_{xz}, \tag{3.31}$$

$$\sigma_{xz}^+ - \sigma_{xz}^- = 0, \tag{3.32}$$

$$u_z^+ - u_z^- = \eta_N \sigma_{zz}, \tag{3.33}$$

$$\sigma_{zz}^+ - \sigma_{zz}^- = 0. \tag{3.34}$$

The equations of motion for $P-SV$ waves in heterogeneous media couple the two components of displacement, u_x and u_z

$$\rho\frac{\partial^2 u_x}{\partial t^2} = (\lambda + 2\mu)\left[\frac{\partial^2 u_x}{\partial x^2} + \frac{\partial^2 u_z}{\partial x \partial z}\right] + \mu\left[\frac{\partial^2 u_x}{\partial z^2} - \frac{\partial^2 u_z}{\partial x \partial z}\right], \tag{3.35}$$

$$\rho\frac{\partial^2 u_z}{\partial t^2} = (\lambda + 2\mu)\left[\frac{\partial^2 u_z}{\partial z^2} + \frac{\partial^2 u_x}{\partial x \partial z}\right] + \mu\left[\frac{\partial^2 u_z}{\partial x^2} - \frac{\partial^2 u_x}{\partial x \partial z}\right], \tag{3.36}$$

where ρ is the density, μ is the shear modulus, and $\lambda + \frac{2}{3}\mu$ is the bulk modulus. To obtain the equations of motion for a layered medium, we use the fact that, in a medium that only varies with depth z, the horizontal component of the slowness

$$p = \frac{\sin\theta_p}{v_p} = \frac{\sin\theta_s}{v_s}, \tag{3.37}$$

is constant. In equation (3.37), $v_p = \sqrt{(\lambda + 2\mu)/\rho}$ is the P-wave velocity, $v_p = \sqrt{\mu/\rho}$ is the S-wave velocity, and θ_p and θ_s are the angles that the P- and S-waves make with the vertical (z) axis. That p is constant means plane-wave solutions for any of the displacements or stresses in a vertically varying medium would have the form $S(t - px - p_z z)$. With this information, x-derivatives can be exchanged for t-derivatives

$$\frac{\partial^2 u_x}{\partial x^2} = p^2 \frac{\partial^2 u_x}{\partial t^2}, \tag{3.38}$$

$$\frac{\partial^2 u_x}{\partial x \partial z} = -p \frac{\partial^2 u_x}{\partial t \partial z}. \tag{3.39}$$

With these substitutions (and the analogous ones for u_z), the system of equations (3.35) and (3.36) can be made into a system purely in terms of depth z and time t

$$(1 - v_p^2 p^2)\frac{\partial^2 u_x}{\partial t^2} = v_s^2 \frac{\partial^2 u_x}{\partial z^2} - p(v_p^2 - v_s^2)\frac{\partial^2 u_z}{\partial z \partial t}, \tag{3.40}$$

$$(1 - v_s^2 p^2)\frac{\partial^2 u_z}{\partial t^2} = v_p^2 \frac{\partial^2 u_z}{\partial z^2} - p(v_p^2 - v_s^2)\frac{\partial^2 u_x}{\partial z \partial t}. \tag{3.41}$$

Note that for normal incidence ($p = 0$), the system of two PDEs decouples into two independent PDEs.

Applying the Galerkin method to equations (3.40) and (3.41), we use the expansions

$$u_x(z,t) = \sum_{K=1}^{N} \alpha_K(t)\phi_K(z), \tag{3.42}$$

$$u_z(z,t) = \sum_{K=1}^{N} \beta_K(t)\phi_K(z), \tag{3.43}$$

and proceed as with the 1D wave equation shown earlier in this chapter. The technique for putting in a split node is outlined in Appendix D.

3.6 Numerical example

We first show an example where a P-wave is incident on a welded boundary for six incident angles between 0° and 30°. The model is shown in Table 3.1. For each angle, the ratio of the reflected P-wave to the incident wave gives reflection coefficient. In Figures 3.2 and 3.3, we compare the reflection coefficient calculated from the finite-element scheme with that obtained from the exact solution (Aki & Richards, 1980) using the Zoeppritz equations. Good agreement is seen over the range of incident angles, validating the numerical scheme for an elastic interface.

In addition, we used the finite-element code to model P-wave scattering from a slip discontinuity, as shown in Figure 3.4. The parameters used for this simulation are given in Table 3.2. Since the P-wave is incident on the slip discontinuity at an angle of 50.5°, it excites up- and down-going converted waves, labeled PS in Figure 3.4. Both horizontal and vertical displacements are shown in Figure 3.4; the polarizations for the various wave types, evident from comparing the horizontal and vertical displacements, agree with those

elastic property	value
density of incident medium	2000 kg/m^3
P-velocity of incident medium	1732 m/s
S-velocity of incident medium	961 m/s
density of transmitting medium	2000 kg/m^3
P-velocity of transmitting medium	1932 m/s
S-velocity of transmitting medium	1061 m/s

Table 3.1. The model used to compare the reflection coefficients calculated from the numerical scheme and the exact solution.

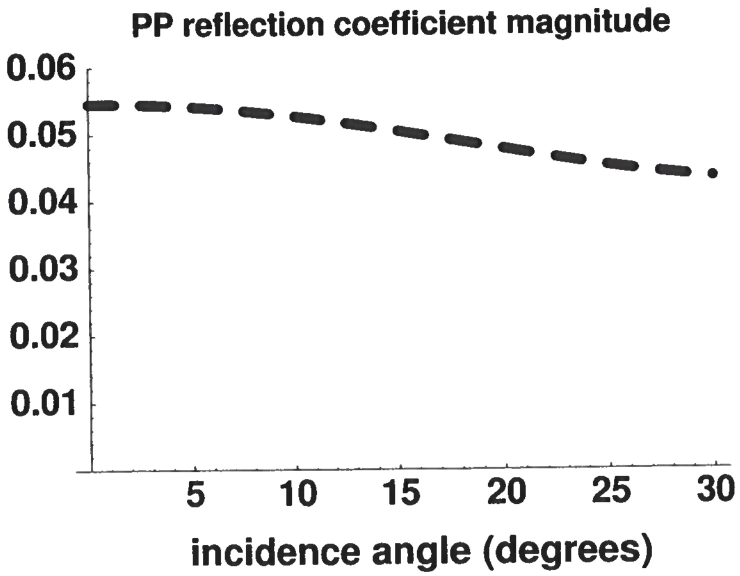

Figure 3.2. Analytically calculated PP reflection coefficients for the model shown in Table 3.1 for incidence angles between 0° and 30°. Compare with Figure 3.3

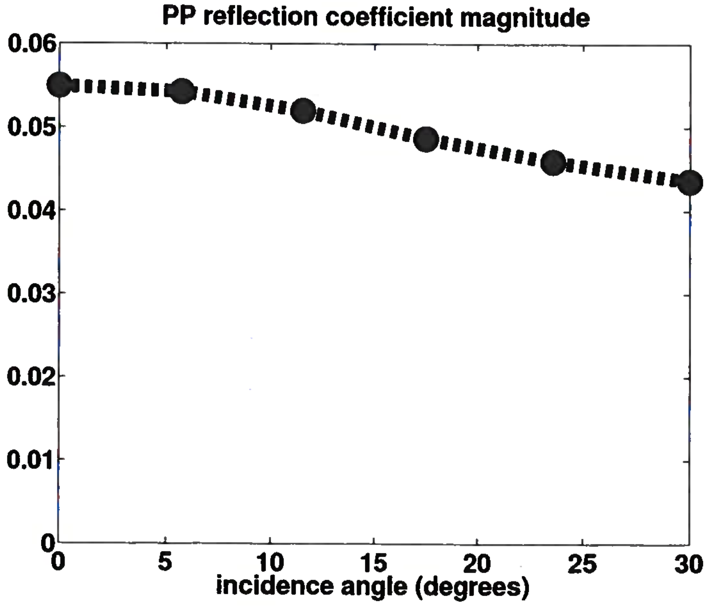

Figure 3.3. *PP* reflection coefficients calculated from the numerical scheme for the model shown in Table 3.1 for six incidence angles between 0° and 30°. Each of the six incidence angles is shown by a black dot. Compare with Figure 3.2

elastic property	value
density of the host medium	2260 kg/m^3
P-velocity of the host medium	2675 m/s
S-velocity of the host medium	1175 m/s
frequency of the incident P-wave	20 Hz
angle of incidence	50.5°
normal compliance	5×10^{-10} m Pa^{-1}
tangential compliance	1×10^{-9} m Pa^{-1}

Table 3.2. The model used to plot the snapshots of the scattered elastic wavefield from a linear slip interface.

expected (see Figure 3.5). The agreement of the polarizations for the various wave types validates our approach to coupling the P- and S-waves in a layered medium at non-normal angles of incidence.

3.7 Conclusions

The exercise of realizing slip discontinuities in a simple 1D finite-element algorithm assists in the understanding of the implementation of slip interfaces in 2D numerical codes, which are further complicated by meshing and assembly issues. We find that proper modeling of fractures can accommodate an explicit, conditionally stable time integration scheme. In 2D or 3D, the repeated use of integration by parts in this chapter would be replaced by Green's Theorem. Simulations in a higher dimension would allow the modeling of crack tips.

In the numerical examples, the background medium is homogeneous except for the slip discontinuities. The finite-element scheme has also been worked out for the case of smoothly varying changes in the material properties. An example of this would be a zone of linearly increasing velocity bounded by two slip discontinuities.

We limited this study to the reflection and transmission of a pure slip (displacement) discontinuity. Schoenberg (1980) has also suggested the possibility of a viscous slip condition. Other, more exotic interface conditions exist, such as the Maxwell and Kelvin versions of the combined displacement and velocity discontinuity (Pyrak-Nolte, 1996). That interface condition models the reflection and transmission from a thin, low shear zone with attenuation and has been validated in laboratory experiments (Pyrak-Nolte *et al.*, 1990). The same finite-element methods described here are needed to numerically model these other types of interfaces. A numerical code has been produced from the methods outlined in this chapter and will be made available in the Matlab codes released with Seismic Un*x (Stockwell, 1997).

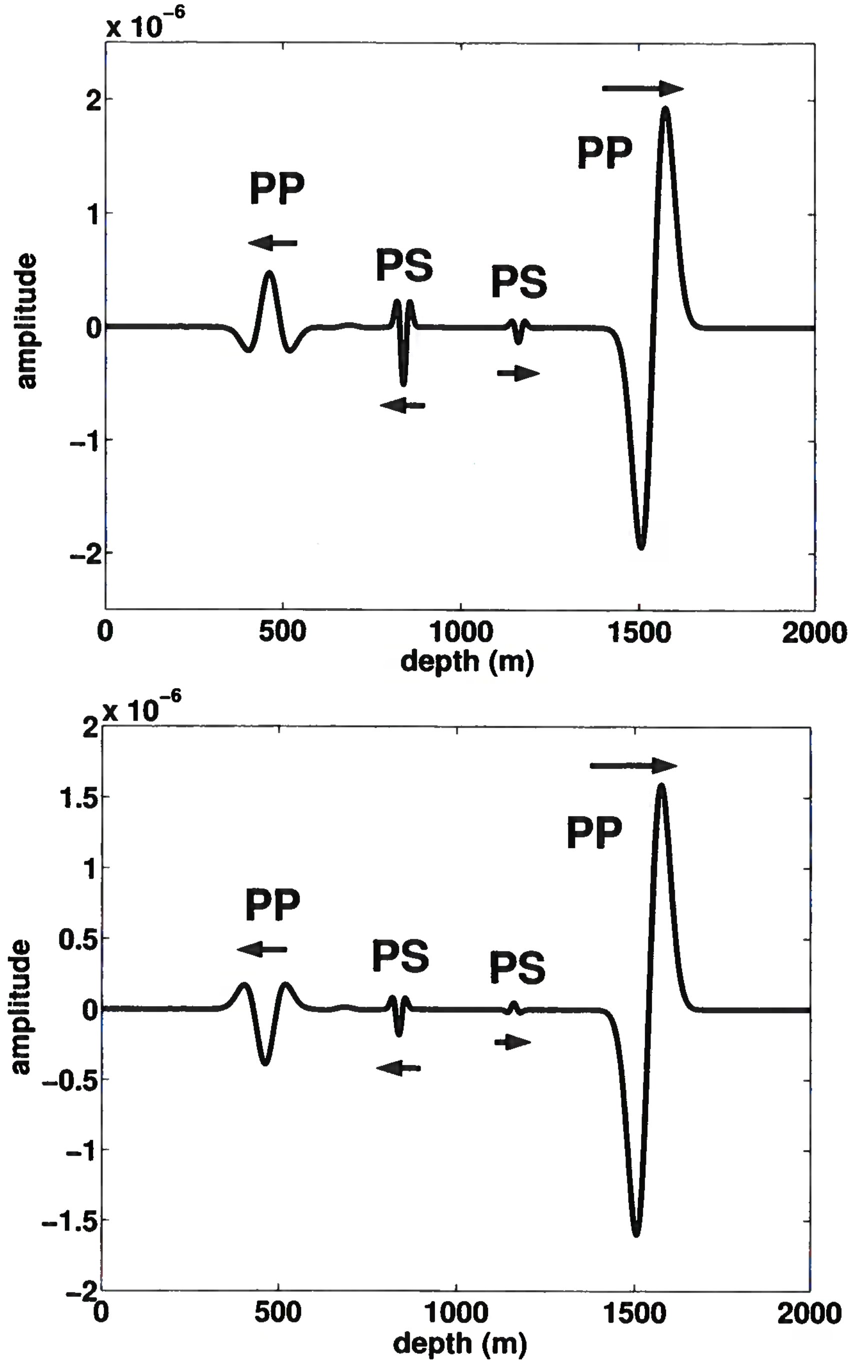

Figure 3.4. Snapshot of the horizontal displacement (top) and vertical displacement (bottom) of the scattered wavefield for a P-wave incident on a slip discontinuity located at a depth of 1000 m. The P-wave is incident from the left, or from smaller values of depth, and at an angle of 50.5°. The reflected PP, transmitted PP, and up- and down-going PS waves are displayed. Their polarizations agree with the expected polarizations shown in Figure 3.5. The model parameters are shown in Table 3.2.

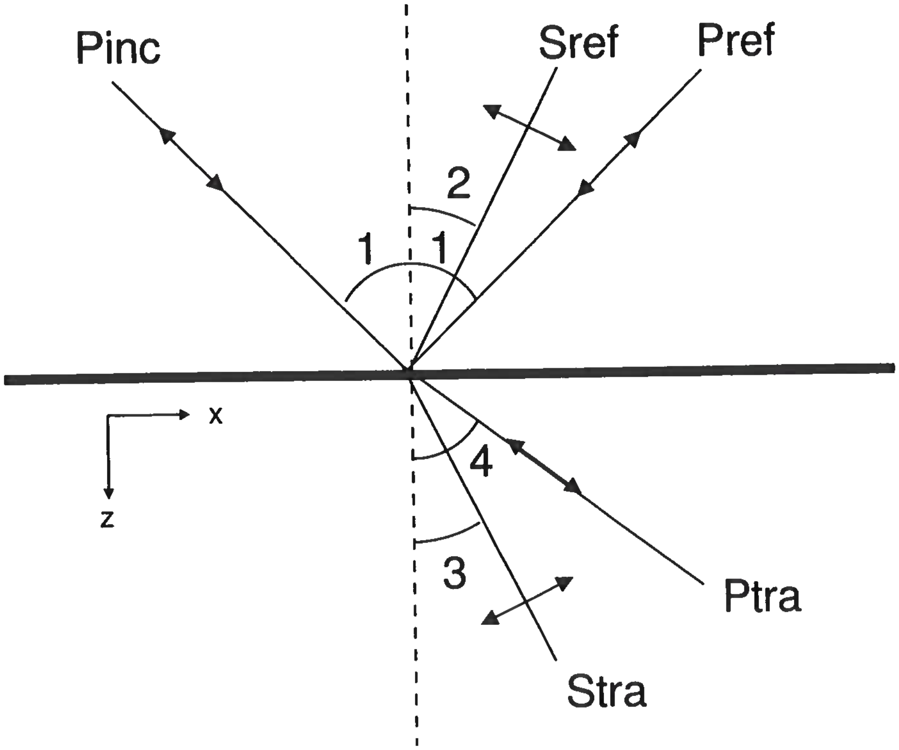

Figure 3.5. A P-wave is incident on a horizontal slip discontinuity. Four waves radiate from the imperfect interface, the reflected P, transmitted P, and up- and down-going converted waves. The polarizations of the waves are shown as arrows.

Chapter 4

Spectral element modeling of fault-plane reflections

4.1 Summary

Simulating the 2D elastic wave equation via the spectral element method (SEM) has advantages over other modeling techniques for studying seismic reflectivity associated with faults. For instance, irregular geometries can be easily accommodated and slip boundary conditions are implemented naturally, as are other methods based on the weak form, like finite-elements. In this chapter, we utilize an existing SEM code that models slip at an interface, such as a fault or fracture, by the split-node approach outlined in appendices C and D. The method of including a slip interface retains the desirable qualities of SEM in that it is explicit in time and does not require the inversion of a large matrix. We also exploit the freedom of meshing inherent in SEM by using an open-source meshing program. We then run through a complete numerical exercise incorporating both SEM forward modeling of shot gathers over a realistically-sized Earth model containing a normal fault and processing of the simulated data to reconstruct post-stack time-migrated images of the kind that are routinely interpreted in the seismic industry. Finally, we dip filter the seismic images to highlight the fault-plane reflections before making amplitude maps on the fault plane. We examine several different fault models to diagnose which of the various influences most contributes to fault reflectivity. To lend physical meaning to the compliance of a slipping fault, we propose an equivalent-layer model under the assumption of weak scattering. The empirical relationships between density, velocity, and effective stress derived in Chapter 1 can then be invoked to relate a slipping interface to a level of pore pressure in the fault zone.[1]

4.2 Introduction

Seismic data acquisition and processing have evolved to the point that fault-plane reflections are often imaged under favorable conditions, such as above salt in the Gulf of Mexico (Liner, 1999). Reflections originating from fault zones hold important information about fluid movement along faults, as shown in Chapter 6 of this thesis, or the capacity of a fault to act as a seal (Haney *et al.*, 2004). Faults have long stumped interpreters by

---

[1] To be submitted to Geophys. Journ. Int.

virtue of their split personality as both hydrocarbon traps and pathways for hydrocarbons to move from deep kitchens into shallower, economically producible reservoirs. Any light that seismic data can shed on the situation would be useful.

To gain a stronger grasp on the factors at play in causing fault-plane reflectivity and errors that can deteriorate their imaging, we have pursued a complete numerical study of seismic wave interaction with fault models. By complete, we do not simply model the entire measured (elastic) wavefield with high fidelity, but additionally process the data back into its time-migrated image, which is the point at which many geoscientists in the oil industry gain access to and begin examining seismic data. We model the wavefield with an implementation of the spectral element method (SEM) written by Dimitri Komatitsch and Jean-Pierre Vilotte at the Institut de Physique du Globe in Paris, France. Further improvements have been made to the original code by Jean-Paul Ampuero in the course of his graduate work (Ampuero, 2002). Jean-Paul has also taken an active role in educating other geoscientists on the subject of SEM and the code, known as SEM2DPACK. He is a main collaborator in the research presented in this chapter. Processing of the elastic wavefield output by the SEM code has been accomplished using Seismic Un*x (Stockwell, 1997).

We first sketch the theory behind SEM and demonstrate the complete numerical approach on a simple fault model that has been used in a previous study (Townsend *et al.*, 1998) of fault reflectivity. After discussing the along-fault dip-filtering step that we employ to highlight the fault-plane reflections in a migrated image, we present results for several different fault models. These models represent examples and combinations of three canonical types of heterogeneity expected at faults. These canonical types are:

1. juxtaposition (sand/shale or shale/sand) contacts
2. pressure contrast ΔP across the fault
3. a slipping fault

We expect from the outset that these various types of heterogeneity show up differently in dip-filtered seismic images. For instance, since the juxtaposition contacts exist over the length scale of a typical bed thickness and have positive (sand/shale) or negative (shale/sand) reflection coefficients, the smoothing of the dip-filter (Oppenheim & Schafer, 1975) should act to suppress their contribution to the fault-plane reflectivity. For instance, the specular contribution to the average reflected intensity of a fault-plane between two vertically shifted layered media with a random reflection coefficient series is zero (R. Snieder, 2002; personal communication). In practice then, away from this idealized model, this type of reflectivity should be relatively suppressed compared to the other two models. This is desirable since the juxtaposition contacts do not carry information on the sealing or conducting properties of the fault. The other two types of heterogeneity, pressure contrasts and slip at the fault plane, which do relate to pore pressure distributions at the fault, are not attacked by the dip filter in the same way as are the juxtaposition contacts. The results of numerical modeling presented in a later section support this claim. The model of a slipping fault has been discussed in the last chapter. It represents a fault that is locally weak compared to the surrounding rock. In the last part of this chapter, we derive a formula that gives physical relevance to the parameter describing the degree of slip on a fault, known as the compliance.

4.3 The spectral element method

Numerical modeling of wave propagation in the earth can be based on the weak (Zienkiewicz & Taylor, 2000) or strong forms (Boore, 1970) of the elastodynamic equations of motion. By weak and strong, we mean the integrated or differential forms of the equations of motion. The spectral element method (SEM), though based on the weak form, combines favorable aspects of both strong and weak formulations. For instance, SEM naturally handles general geometries and exotic boundary conditions. In the finite-difference method (based on the strong form), it is notoriously difficult to implement a linear-slip boundary condition (Coates & Schoenberg, 1995) or any general boundary condition for that matter (Boore, 1970; Kelly *et al.*, 1976). On the other hand, SEM does not require the inversion of a large matrix, a property usually identified with finite-difference methods. Formally, this last property of SEM means that its mass matrix is diagonal and its computational cost is relatively small. Note that SEM does this in a way similar to mass-lumping (Karniadakis & Sherwin, 1999), which has been used to diagonalize finite-element schemes. SEM has the additional property of spectral convergence, meaning that, as the polynomial order of the basis functions is increased, the numerical error goes down exponentially (Karniadakis & Sherwin, 1999).

The term "spectral element" indicates that SEM is a mixture of finite-element and spectral methods (Komatitsch & Vilotte, 1998). As a result, there are two parameters relevant to the mesh in SEM: the size of the elements and polynomial degree ($n-1$, where n is the number of zero crossings of the basis functions used within each element). Komatitsch & Tromp (2003) refer to these parameters when they speak of the global mesh and the local mesh. Concerning the local mesh, there is a known trade-off between accuracy and numerical cost (Seriani & Priolo, 1994), which suggests that polynomial degrees no higher than 10 should be used within the elements. For the numerical examples in this paper, we use a polynomial degree of eight. We made this choice based on an optimal criterion for polynomial degree and the fact that SEM typically works with Lagrange polynomials. The zero crossings of Lagrange polynomials are irregularly spaced over the interval [-1,1], which is mapped onto the sides of the elemental mesh. The exception to the irregular spacing occurs for Lagrange polynomials of even degree, for which a zero-crossing always occurs at 0 on the interval [-1,1].

4.4 Modeling of a fault

As an example of the ability of SEM to model seismic scale structures, we present a complete modeling and processing sequence for a simple fault model. The SEM forward modeling has been run in serial (one node for each shot) on a 32-processor pentium IV Xeon (3.0-GHz) cluster. All of the processing has been performed on a workstation using

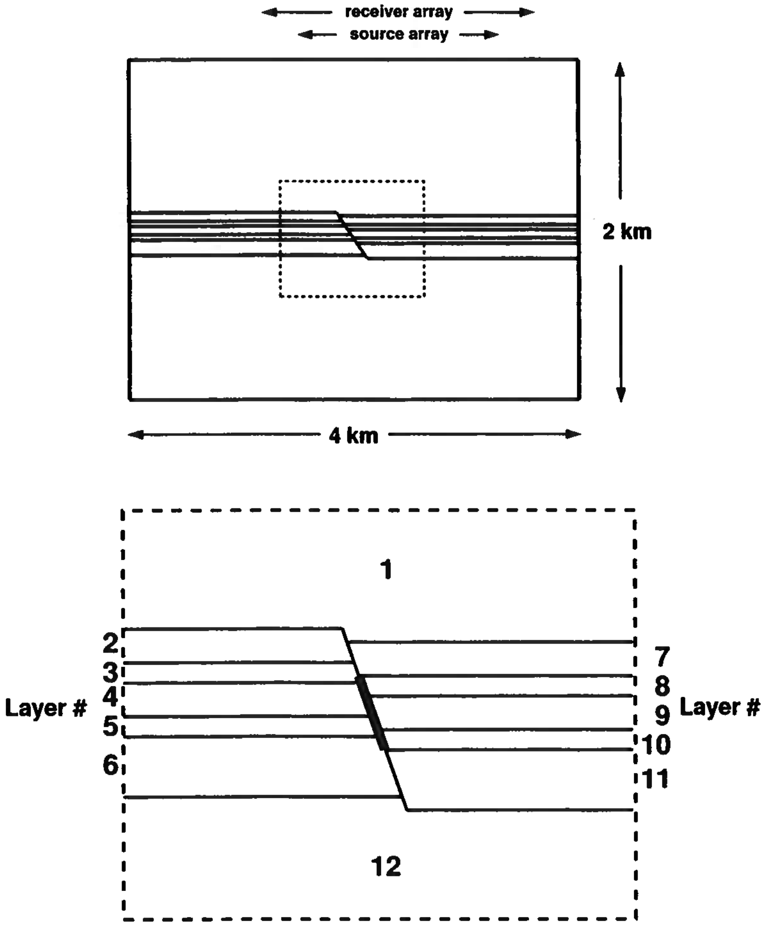

Figure 4.1. The entire numerical model with a zoom-in of the normal fault. The zoom area is shown on the entire numerical model with a dashed rectangle. The lengths of the source and receiver arrays are shown by extended arrows. Eleven sources evenly spaced over 2000 m (200-m shot interval) and 241 receivers over 3000 m (12.5-m receiver interval). In the zoom, the layers are labeled with numbers 1-12 corresponding to the material properties for models listed in subsequent tables. For models with a slipping fault, the portion of the fault plane that slips is shown by a thicker line in the zoom.

Layer	Thickness (m)	V_P (m/s)	ρ (kg/m^3)
1	900	2000	2000
2	50	2350	2080
3	30	2400	2150
4	50	2500	2130
5	30	2600	2200
6	90	2750	2180
7	850	2800	2250

Table 4.1. A model from Townsend *et al.* (1998) for the first SEM example in this chapter. Each layer is a Poisson medium, $v_s = v_p/\sqrt{3}$.

the Seismic Un*x package (Stockwell, 1997). Figure 4.1 depicts the geometry of the model, and Table 4.1 shows the material properties of the various layers. The normal fault we model has a vertical throw of 20 m, a value characteristic of a small fault. The model shown in Table 4.1 has been previously studied by Townsend *et al.* (1998) to assess changes in seismic attributes caused by faults disrupting the lateral continuity of events.

We mesh the interior of the computational grid shown in Figure 4.1 using a freely available mesh program developed by INRIA, called EMC2. The program can be downloaded at:

http://www-rocq.inria.fr/gamma/cdrom/www/emc2/eng.htm.

For this example and others in this paper, we use a semi-structured mesh since the fault geometries modeled are not overly complex. A semi-structured mesh is desirable when possible since the accuracy of SEM depends on the Jacobian of the transformation between a generally shaped element and a standard rectangular element over which the integration is performed. Though the mesh has structure, it honors the slanted boundaries of the fault. After initial construction of the mesh, the quadrangle elements are regularized so that their shapes mimic rectangles as closely as possible.

The upper left panel of Figure 4.2 displays a typical shot record. Since the SEM code is elastic, both primary and converted waves show up on the vertical component of the displacement seismograms. It should be noted that, if the model in Table 4.1 had a physically realistic vertical velocity gradient, ray bending would have served to separate the P- and S-waves more effectively into the vertical and horizontal components. Without a velocity gradient, model-specific muting of the converted waves is necessary in order to proceed with conventional P-wave time-processing. We first subtract off the direct waves by running a homogeneous subsurface simulation with the elastic properties of layer 1; see Figure 4.1 and Table 4.1. After this step, we perform a geometrical-spreading correction, NMO, DMO, and stack to simulate zero-offset data. The stacked section is shown in the upper right panel of Figure 4.2. Note the significant diffracted energy coming from the sharp

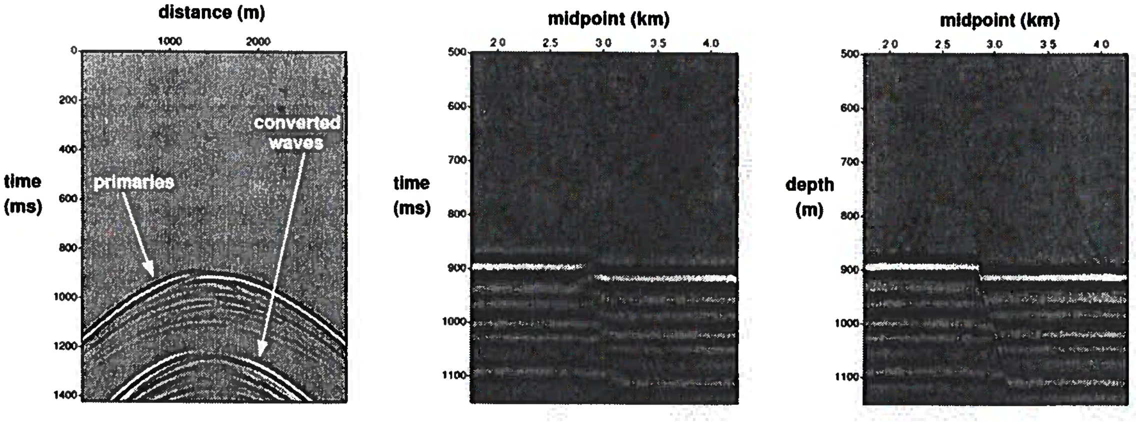

Figure 4.2. Three stages of data processing. On the left is a shot record from the SEM code after subtracting off the direct waves, leaving the purely up-going wavefield. The middle panel depicts the data in the midpoint-time domain after correction for geometric spreading, NMO, DMO, and stack. Note the diffractions from the bed terminations at the fault plane. Finally, the migrated image is shown on the right, with the fault plane clearly illuminated. The migration result, though based on constant velocity, was depth converted.

corners at the fault. With the simulated zero-offset section, we proceed with a constant-velocity migration using the velocity of the overburden (layer 1). Hence, a source of error in this simulation originates from the slight undermigration of the deepest reflectors and the fault-plane reflection. We chose to migrate with constant velocity since we have interpreted time-migrated seismic sections in the Gulf of Mexico (Haney *et al.*, 2004) and wanted the SEM modeling to mimmick the data as closely as possible. With this full suite of forward modeling and processing capabilities, we apply SEM to study various normal fault models. Before going into the details of the modeling, though, we present the type of dip-filter I use to isolate the migrated fault-plane reflections.

4.5 Dip filtering

In this section, using an array-based approach similar to the analysis of seismic data processing in Chapter 2, we derive the form of the dip filter that we apply to the migrated images to accentuate the fault-plane reflections. In the data examples from the Gulf of Mexico that make up the final chapters of this thesis, a similar dip filter acts on a 3D seismic data volume in successive 2D dip lines. The only difference is that the dip filter constructed here is spatially-invariant; the dip filter used on the 3D seismic data volume locally searches for the maximum coherency direction within an angular range before dip-filtering.

In Figure 4.3, a dipping event is shown in a post-stack seismic image. The function of

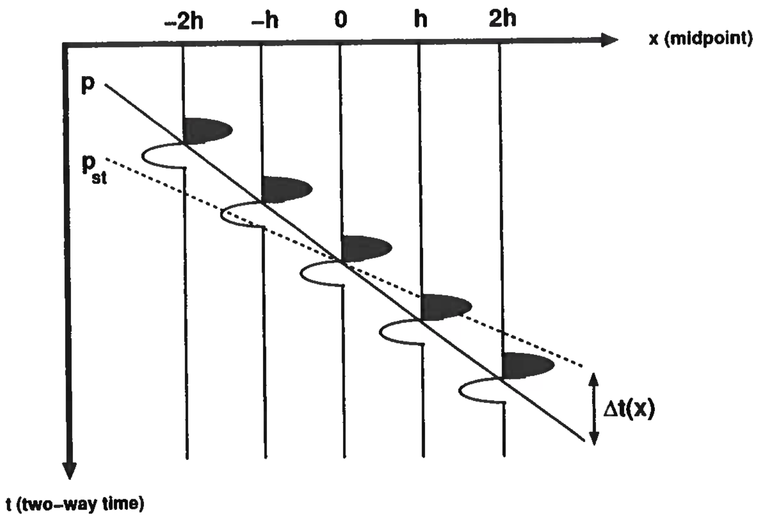

Figure 4.3. Dipping event with true dip direction given by the slanted solid line. The event is summed along a direction given by the dashed line, and the result is placed at the intersection of the two lines at the center trace. When there is a difference in the two dips, the true dip p and the stacking dip p_{st}, a time shift Δt is induced that varies linearly with midpoint x. In this example, the seismic data exist at equally-spaced, discrete midpoint locations.

the dip filter is to stack along the dashed line and place the stack result at the intersection of the solid and dashed lines; where the coordinate system is chosen such that the midpoint is equal to 0. Note that, in Figure 4.3, the dip filter emphasizes a direction different from the dip of the event. This difference induces a time shift at the m-th input trace (shown as a vertical arrow). Suppose that the true dip, the dip of the event, is p (dimension s m^{-1}) and the dip of the stacking curve is p_{st}. The time shift at the m-th input trace is thus

$$\Delta t_m = (p - p_{st})\, mh, \tag{4.1}$$

where h is the midpoint spacing and m is the discrete variable running over midpoint location. Assuming that the dipping event has a constant waveform $f(t)$, the result of the summation, $g(t)$, over the stacking curve can be written as

$$\begin{aligned} g(t) \;=\; & \frac{1}{2n+1}\left[f(t-\Delta t_{-n}) + \cdots + f(t-\Delta t_{-1}) + \right. \\ & \left. f(t) + f(t-\Delta t_1) + \cdots + f(t-\Delta t_n)\right], \end{aligned} \tag{4.2}$$

where $2n+1$ is the length of the dip filter in terms of the number of traces. In the example shown in Figure 4.3, $n = 2$. Equation (4.2) has exactly the same form as equation (2.1) encountered earlier during the discussion of stacking errors. When we again take the Fourier transform over time and move to the ω-x domain, equation (4.2) becomes

$$G(\omega) = F(\omega)K(\omega), \tag{4.3}$$

with the Fourier transforms of $f(t)$ and $g(t)$ shown as $F(\omega)$ and $G(\omega)$ and the transfer function, K, given by

$$K(\omega) = \frac{1}{2n+1} \sum_{m=-n}^{n} e^{i\omega(p-p_{st})mh}. \tag{4.4}$$

This series is exactly the same as the one approximated by stationary phase in Chapter 2. The difference here is that the time shifts, multiplying ω in the argument of the exponential term, are linear in m. Hence, the series in equation (4.4) can be evaluated exactly.

Using the geometric series, equation (4.4) can be written as

$$K(\omega) = \frac{1}{2n+1} \left[\frac{1 - e^{i\omega(n+1)(p-p_{st})h}}{1 - e^{i\omega(p-p_{st})h}} + \frac{1 - e^{-i\omega(n+1)(p-p_{st})h}}{1 - e^{-i\omega(p-p_{st})h}} - 1 \right]. \tag{4.5}$$

Putting the first two terms in the brackets of equation (4.5) under a common denominator and simplifying further yields a filter similar to that obtained for convolution with a boxcar, or rectangular window (Oppenheim & Schafer, 1975)

$$K(\omega) = \frac{1}{2n+1} \left[2\frac{\sin[\omega(n+1)(p-p_{st})h/2]}{\sin[\omega(p-p_{st})h/2]} \cos[\omega n(p-p_{st})h/2] - 1 \right]. \tag{4.6}$$

This filter is real because of the symmetric summation about its output point and can be better understood by making the substitution $\Delta t = (p - p_{st})h$ in equation (4.6)

$$K(\omega) = \frac{1}{2n+1} \left[2\frac{\sin[\omega(n+1)\Delta t/2]}{\sin[\omega\Delta t/2]} \cos[\omega n\Delta t/2] - 1 \right]. \tag{4.7}$$

The amplitude spectrum of the dip filter is shown in Figure 4.4 for certain values of n and Δt.

A dip filter in terms of ω and k is needed to enhance fault-plane reflections on a migrated time section. The filter in equation (4.6) is only in terms of ω. To get the k dependence, we exploit the fact that $p = -k/\omega$ (Hatton *et al.*, 1986). This means that linear features with a dip p in the t-x domain get mapped into linear features with the negative dip in the ω-k domain. Substituting $p = -k/\omega$ into equation (4.6) gives

$$K(\omega, k) = \frac{1}{2n+1} \left[2\frac{\sin[(n+1)(\omega p_{st} + k)h/2]}{\sin[(\omega p_{st} + k)h/2]} \cos[n(\omega p_{st} + k)h/2] - 1 \right]. \tag{4.8}$$

This is the form of a dip filter that corresponds to stacking $2n + 1$ traces centered about the output point along a dip p_{st}.

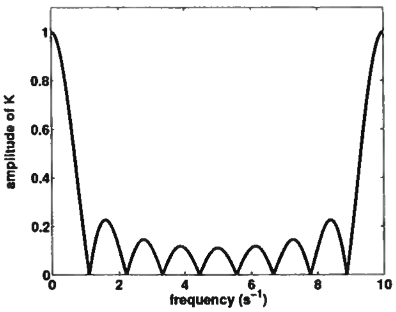

Figure 4.4. Representative amplitude spectrum for the dip filter. The parameters used for this plot were $n = 4$ and $\Delta t = 0.1$. Note that the first aliased frequency for this choice of Δt is at $f = 10$ Hz.

4.6 SEM modeling of reflected waves

The dip filter operation discussed in the previous section has been applied to simulated seismic images in the ω-k domain. An alternative procedure would be a combination of interpolation and slant stacking in the t-x domain; however, the ω-k dip filter is sufficiently accurate, as we show here. Figure 4.5 shows a plot of the simulated reflection images for the two of the models presented in this chapter next to their dip-filtered versions that highlight the fault-plane reflection. The dip filter applied to these plots has a length of 21 traces and the adata and filter have a trace-to-trace spacing of 6.25 m (the midpoint spacing); this sampling avoids any aliasing problems and attacks all events not having the dip (slope) of the fault-plane reflection. In particular, it attacks the horizontal reflections.

The upper panels of Figure 4.5 are for a model of a pressure difference across the fault, which acts like a traditional seismic interface. The lower panels of Figure 4.5 are for a model of a linear-slip interface, which, in contrast to the pressure difference model, reflects the derivative of the incident wave (see Appendix E for details). A slice cut out of the dip-filtered images in the direction perpendicular to the fault-plane (shown as a white arrow in the right-hand panels of Figure 4.5) helps in assessing the accuracy of the numerically simulated fault-plane reflections. In Figure 4.6, we plot the reflected waveforms together with either the incident wave or the derivative of the incident wave, depending on whether the model contains the pressure difference or slip at the fault. The agreement seen between the waveforms in Figure 4.6 demonstrates that the SEM modeling, processing, and dip-filtering together produce an accurate reflected waveform from the fault plane.

In the following three sections, we examine reflectivity from the fault plane for a juxtaposition-contrast model, three pore-pressure contrast models, and four slipping-fault models embedded in one of the pore-pressure-contrast models. The purpose of this modeling exercise is to get a feeling for which type of reflectivity should dominate at a general fault. We also perform the processing of the SEM modeled data contaminated with certain errors to see how maps of the amplitude along the fault are affected. I focus on maps of the

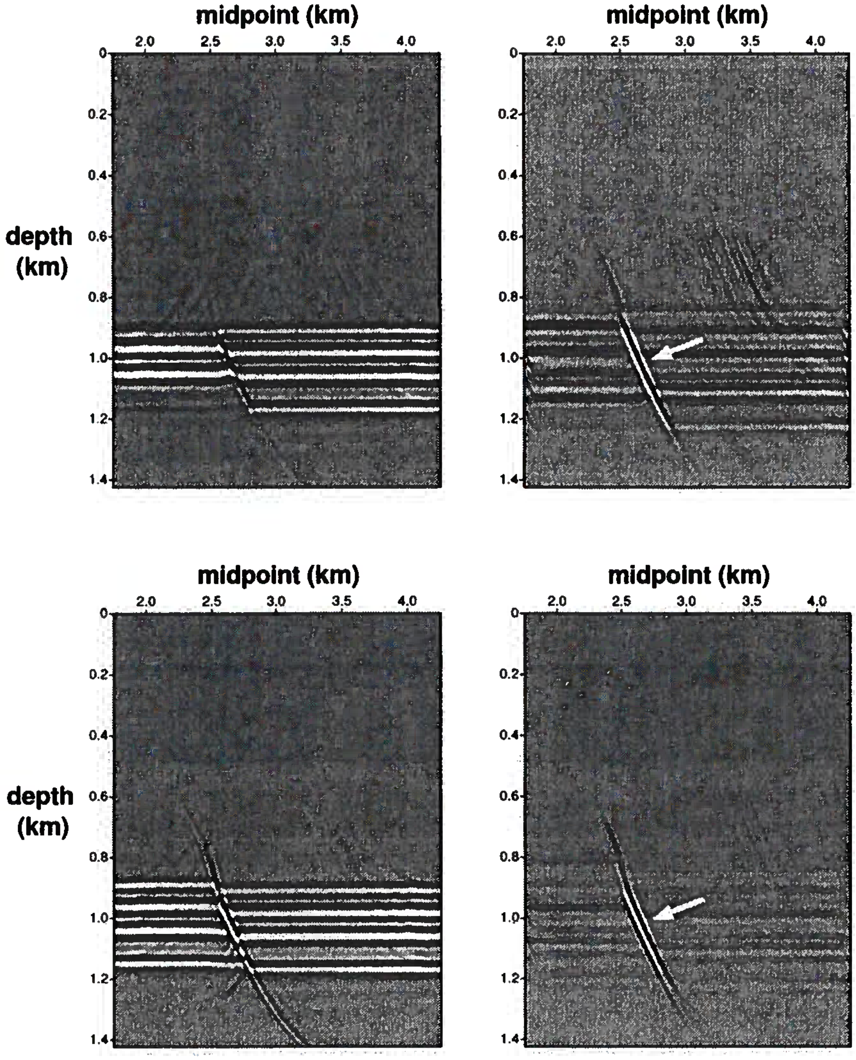

Figure 4.5. Migrated seismic images from Model 2 (top panels) and Slip-Model A embedded in Model 1 (bottom panels). Their dip-filtered versions, used to highlight the fault-plane reflections, are shown in the right-hand panels. Slip-Model A is for a slipping fault (see Table 4.6), which is embedded in Model 1 (see Table 4.2). Model 2 is for a pore-pressure contrast across the fault (see Table 4.3). The traces in Figure 4.6 are sliced from these images in a direction normal to the fault-plane, as shown by an arrow in the dip-filtered images. The horizontal events in the upper panels appear to be not as well suppressed as the lower panels simply because the fault-plane reflection is stronger in the bottom panel and, as a result, the amplitude clip for the display is higher.

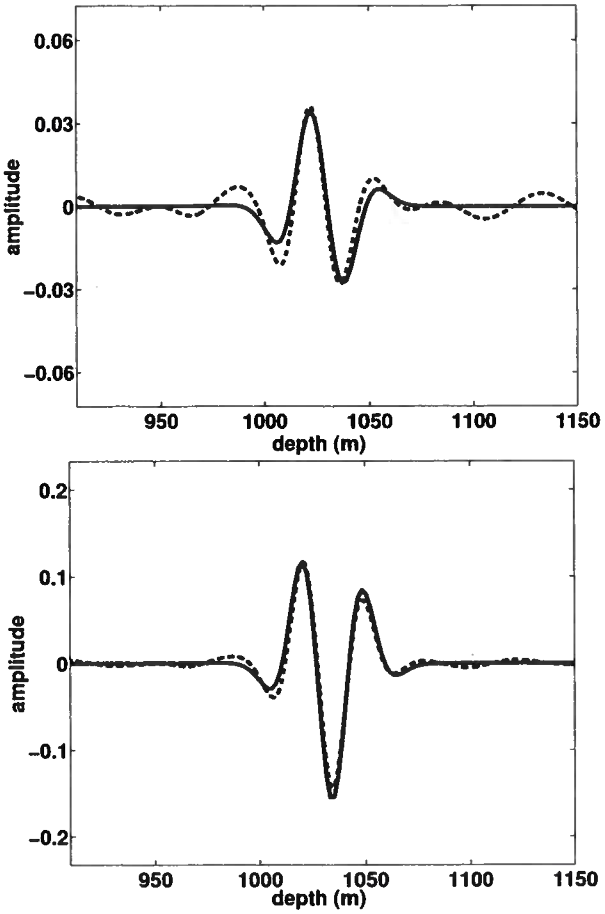

Figure 4.6. The reflected waves from Model 2 (top), a pore pressure contrast, and Slip-Model A embedded in Model 1 (bottom), a slipping fault, are shown in dashed lines. The reflected waveforms for these two models are different in shape. The reflected waveform for Model 2 should be the wavelet, which is plotted in the top panel as a solid line for comparison with the numerical result. The waveform for Slip-Model A embedded in Model 1 should be the the derivative of the wavelet, which is plotted in the bottom panel as a solid line for comparison. The agreement between the numerical results for the fault-plane reflections and the expected waveforms validates the sequence of modeling, processing, and dip-filtering used here.

Layer	Thickness (m)	ρ (kg/m^3)	v$_p$ (m/s)	v$_s$ (m/s)
1	900	2240	2600	1100
2	50	2280	2750	1250
3	30	2240	2600	1100
4	50	2280	2750	1250
5	30	2240	2600	1100
6	90	2280	2750	1250
7	50	2280	2750	1250
8	30	2240	2600	1100
9	50	2280	2750	1250
10	30	2240	2600	1100
11	90	2280	2750	1250
12	850	2240	2600	1100

Table 4.2. Model 1 for the SEM modeling. The throw between the upthrown (layers 2 through 6) and downthrown (layers 7 through 11) sediments is 20 m. The sediments on both sides of the fault are at hydrostatic pore pressure. The geometry of the model is given in Figure 4.1. The values are taken from the JD-sand and its lower bounding shale at a depth of 2 km. The pore pressure is ~ 2800 psi at that location.

amplitude along the fault since this is the approach taken on seismic data from South Eugene Island in Chapters 5 and 6.

4.7 Amplitude of waves reflected from a juxtaposition contact

Table 4.2 shows the parameters of a juxtaposition model for the subsurface geometry shown in Figure 4.1. There are two rock types in this example, an acoustically hard shale (ρ = 2280 kg/m^3, v$_p$ = 2750 m/s, and v$_s$ = 1250 m/s) and an acoustically soft sand (ρ = 2240 kg/m^3, v$_p$ = 2600 m/s, and v$_s$ = 1100 m/s). The values for the sand are taken from a well log that intersected a sand layer at the South Eugene Island field known as the JD-sand. The shale values come from the lower bounding shale beneath the JD-sand. In Figure 4.7, we plot these well logs at the depth of this lithologic contact. These two layers are at hydrostatic conditions, which at this depth is nominally 2800 psi.

In Figure 4.8, we plot the reflected amplitude from the juxtaposition model within a small window (100 ms) of the fault-plane for four different processing scenarios. These different scenarios are motivated by the data examples in Chapters 5 and 6. The first scenario, shown in the upper-left panel of Figure 4.8, compares the extracted amplitude on the fault plane of the noise-free dip-filtered image with the amplitude extracted after 20% Gaussian noise was added to the original image before dip filtering. As can be seen, the dip-filtering step is robust in the presence of random noise, giving roughly the $1/\sqrt{n}$

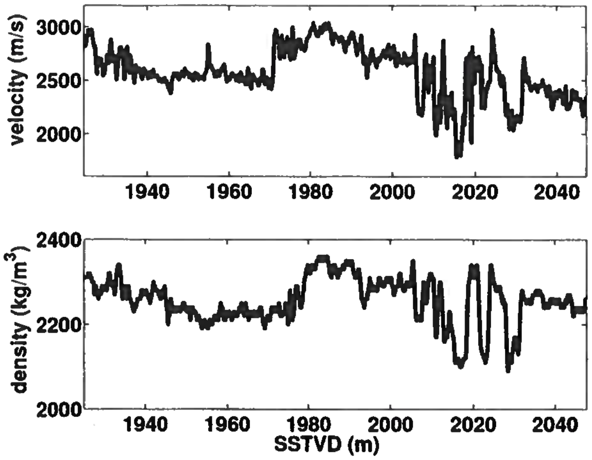

Figure 4.7. Velocity and density logs in the A20ST well at the South Eugene Island field showing the interface between the JD-sand and its lower bounding shale at 1975 m sub-sea true vertical depth (SSTVD). The log information at this contact is used to construct the sand/shale model in Table 4.2. These logs also cut through a growth fault zone known as the B-fault at around 2020 m SSTVD.

attenuation of noise exploited in stacking. The processing is such that the amplitude of the reflected waves is an indication of the reflection coefficient at the boundary giving rise to the reflected wave, at least within any changes induced by amplitude variations with offset (AVO) in the stack. The pattern of the amplitude map reflects the spatially varying presence of juxtaposition contacts for this model, as the amplitude wildly oscillates up and down. The second scenario, shown in the lower-left panel of Figure 4.8, compares the extracted amplitude on the fault-plane of the noise-free dip-filtered image with automatic gain control (AGC) applied to the amplitude extracted after 20% Gaussian noise was added to the original image before dip filtering and AGC. The AGC operates in a time window of 200 ms. In this panel, the true-amplitude degrading nature of the AGC is clear (the absolute value of the amplitude is completely different from the result without AGC); however, along the fault some of the same qualitative patterns are present. The same can be said for the third scenario in the upper-right panel of Figure 4.8. In this panel, everything is the same as in the upper-left panel, except that DMO has been omitted in the processing sequence. The omission of DMO serves to dampen the fault-plane reflections caused by mis-stacking, similar to what was discussed and shown in Chapter 2. The lower-right panel of Figure 4.8 is the same as in the lower-left panel, except that DMO has again been omitted in the processing sequence. This is the most extreme and problematic of the processing sequences, with AGC and without DMO; the patterns on the fault-plane seen in the upper-left panel are barely recognizable.

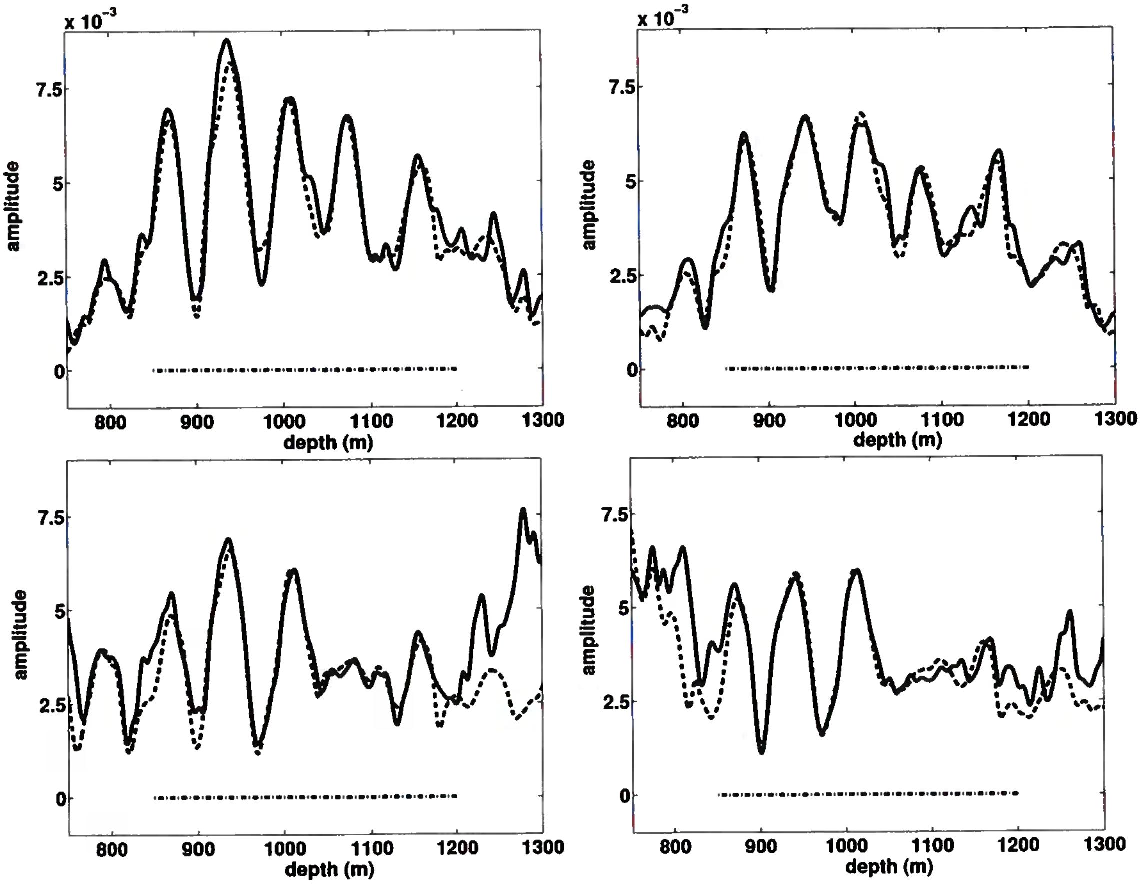

Figure 4.8. Amplitude along fault-plane for Model 1 shown in Table 4.2, the juxtaposition contact model, with four different processing scenarios. The amplitude is plotted as a function of depth on the fault-plane, and the extent of the fault-plane is shown by a horizontal line in the bottom portion of each plot. The processing scenarios are: 1) upper-left panel: amplitude extracted from the noise-free image (dashed) and from the image with 20% additive Gaussian noise (solid), 2) lower-left panel: amplitude extracted from the noise-free image with AGC applied (dashed) and from the image with 20% Gaussian noise added in before applying AGC (solid), 3) upper-right panel: amplitude extracted from the noise-free image without DMO included in the processing sequence (dashed) and from the image with 20% additive Gaussian noise, but no DMO (solid), and 4) lower-right panel: amplitude extracted from the noise-free image with AGC applied but no DMO (dashed) and from the image with 20% Gaussian noise added before applying AGC but no DMO (solid). There is no slip at the fault.

Layer	Thickness (m)	ρ (kg/m^3)	V$_P$ (m/s)	V$_S$ (m/s)
1	900	2240	2600	1100
2	50	2240	2570	1070
3	30	2210	2380	880
4	50	2240	2570	1070
5	30	2210	2380	880
6	90	2240	2570	1070
7	50	2280	2750	1250
8	30	2240	2600	1100
9	50	2280	2750	1250
10	30	2240	2600	1100
11	90	2280	2750	1250
12	850	2240	2600	1100

Table 4.3. Model 2 for the SEM modeling. The geometry of the model is given in Figure 4.1. There is 20 m of throw between the upthrown (layers 2 through 6) and downthrown (layers 7 through 11) sediments, in addition to 600 psi of pore pressure difference. The difference in pore pressures is the result of the upthrown sediments being overpressured. The densities and velocities of layers 2 through 6 are relatively lower than the normally compacted, hydrostatically pressured layers 7-11 on the downthrown side. To relate the velocities and densities to pressure, the mechanism of overpressure is taken to be purely compaction disequilibrium.

4.8 Amplitude of waves reflected from a pore-pressure contrast across a fault

In Tables 4.3, 4.4, and 4.5 are three different models that incorporate pore pressure contrasts of 600 psi, 300 psi, and 150 psi, respectively, across the fault. The aim of using these models is to see how small a pore pressure contrast can be and still be detectable in the fault-plane reflectivity. These figures are relevant to studying the fault-plane reflectivity at South Eugene Island since pressure measurements taken near the large, minibasin-bounding growth fault, known as the A-fault, show a 780 psi increase in pore pressure over 18 m in going from the hydrostatically pressured downthrown sediments to the overpressured upthrown sediments (Losh *et al.*, 1999). With the pore-pressure contrasts in the three models being 600 psi, 300 psi, and 150 psi, the effective stress values can be computed using a hydrostatic pressure of 2800 psi (the same as for the juxtaposition model covered in the previous section). The juxtaposition model can be thought of as having a 0 psi pore-pressure difference across the fault. The values of the densities and velocities used in the three models are consistent with the effective stress relationships derived in Chapter 1 assuming that the mechanism of overpressure is pure undercompaction.

In Figure 4.9 are plotted the maximum reflected amplitude from Model 2 ($\Delta P = 600$

Layer	Thickness (m)	ρ (kg/m^3)	V_P (m/s)	V_S (m/s)
1	900	2240	2600	1100
2	50	2260	2660	1160
3	30	2225	2490	990
4	50	2260	2660	1160
5	30	2225	2490	990
6	90	2260	2660	1160
7	50	2280	2750	1250
8	30	2240	2600	1100
9	50	2280	2750	1250
10	30	2240	2600	1100
11	90	2280	2750	1250
12	850	2240	2600	1100

Table 4.4. Model 3 for the SEM modeling. The geometry of the model is given in Figure 4.1. Same as Table 4.3 except that the pore pressure difference is 300 psi.

Layer	Thickness (m)	ρ (kg/m^3)	V_P (m/s)	V_S (m/s)
1	900	2240	2600	1100
2	50	2270	2705	1205
3	30	2232	2545	1045
4	50	2270	2705	1205
5	30	2232	2545	1045
6	90	2270	2705	1205
7	50	2280	2750	1250
8	30	2240	2600	1100
9	50	2280	2750	1250
10	30	2240	2600	1100
11	90	2280	2750	1250
12	850	2240	2600	1100

Table 4.5. Model 4 for the SEM modeling. The geometry of the model is given in Figure 4.1. Same as Table 4.3 except that the pore-pressure difference is 150 psi.

psi) within a small window (100 ms) of the fault-plane for four different processing scenarios. These different processing scenarios are motivated by the data examples in Chapters 1 and 6 of this thesis and are the same as in the previous section on juxtaposition contrasts. The scenarios include the presence and absence of 20% additive Gaussian noise with the full processing sequence (upper-left panel of Figure 4.9), the application of AGC (lower-left panel of Figure 4.9), the omission of DMO in the processing sequence (upper-right panel of Figure 4.9), and the combined application of AGC and the omission of DMO in the processing sequence (lower-right panel of Figure 4.9).

In these plots, the effect of the juxtaposition contacts shows up in this model as a high frequency wobble on top of the low frequency trend due to the presence of a ΔP across the fault. This means that a pore-pressure difference of 600 psi is sufficient enough to dominate the reflectivity attributable to juxtapositions. This occurs for two reasons: the ΔP is large enough across the fault and the dip filter preferentially attacks the juxtapositions since they change in polarity along the fault plane. From the plots in Figure 4.9, the most severe processing artifact, in the sense of destroying the relative amplitude pattern, is the AGC.

In Figure 4.10 are plotted four different models of ΔP across the fault: 600 psi in the upper-left panel (Model 2), 300 psi in the upper-right panel (Model 3), 150 psi in the lower-left panel (Model 4), and 0 psi (the juxtaposition model, Model 1) in the lower-right panel. All of these amplitude maps are plotted both with (solid line) and without (dashed line) 20% Gaussian additive noise. Comparison of the plots shows essentially linear reduction of reflection amplitudes with reduction in pore-pressure contrast. For a pore-pressure contrast as small as 150 psi, it is difficult to tell if a contrast exists. Specifically, note the similarity of the lower-left (150 psi) and lower-right (0 psi) panels, especially in the degree with which the wobbles due to the juxtapositions contribute to the fault reflectivity. To support this estimate of the minimum ΔP detectable, we show in Chapter 5 that, at a fault known as the F-fault ($\Delta P = 100$ psi) at South Eugene Island, there is almost no indication of reflectivity compared to the large minibasin-bounding A-fault ($\Delta P = 780$ psi).

4.9 Amplitude of waves reflected from a linear-slip fault

We use the abilities of the SEM code to accommodate slip at an interface to model four different slipping interfaces, as described in Table 4.6, in terms of their normal and tangential (shear) compliances. We label these models in order from the most to the least slipping as Slip-Model A, B, C, and D. The examples here have the linear-slip interface embedded in layered Model 2, described previously ($\Delta P = 600$psi). The entire fault-plane does not slip, only a portion of it as shown in Figure 4.1. In the next section, we present a weak scattering model to relate the value of the compliances to pore pressures in a thin fault zone. For now, these values are simply parameters describing the degree of bonding between the surfaces on either side of the linear-slip interface.

The amplitude of the fault-plane reflection from Slip-Model A embedded in Model 2 is displayed in Figure 4.11 for the four processing scenarios outlined earlier in the sections on juxtaposition contacts and pore pressure difference across the fault: 20% noise (upper-left panel), AGC (lower-left panel), no DMO (upper-right panel), and AGC and no DMO

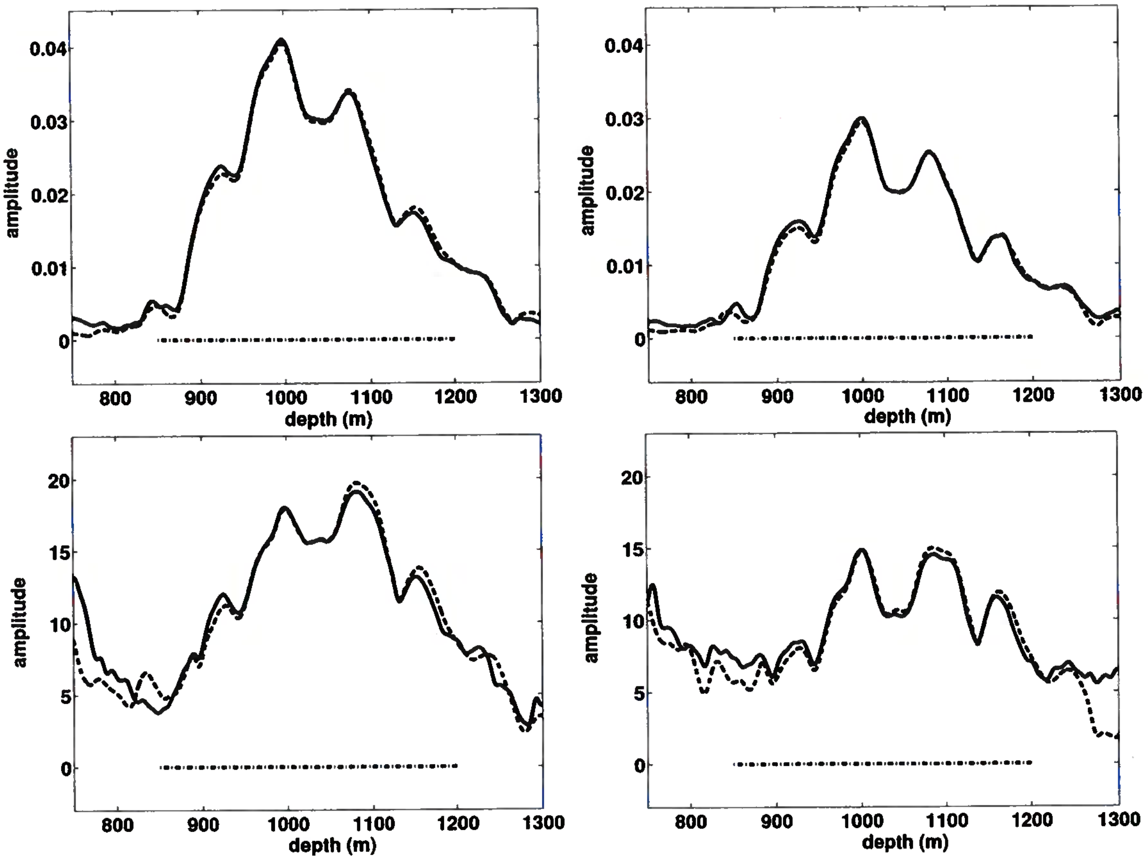

Figure 4.9. Amplitude along fault-plane for Model 2 shown in Table 4.3, a model with a pore pressure contrast of 600 psi across the fault, with four different processing scenarios (the same ones as in Figure 4.8). See the caption for Figure 4.8 for details about the amplitudes plotted and about the four scenarios.

Slip-Model	normal compliance, η_N (m Pa^{-1})	tangential compliance, η_T (m Pa^{-1})
A	5.0×10^{-10}	1.0×10^{-9}
B	3.5×10^{-10}	7.0×10^{-10}
C	2.5×10^{-10}	5.0×10^{-10}
D	1.0×10^{-10}	2.0×10^{-10}

Table 4.6. Four different slip interfaces described in terms of their normal and tangential compliances. These have been used in the SEM modeling.

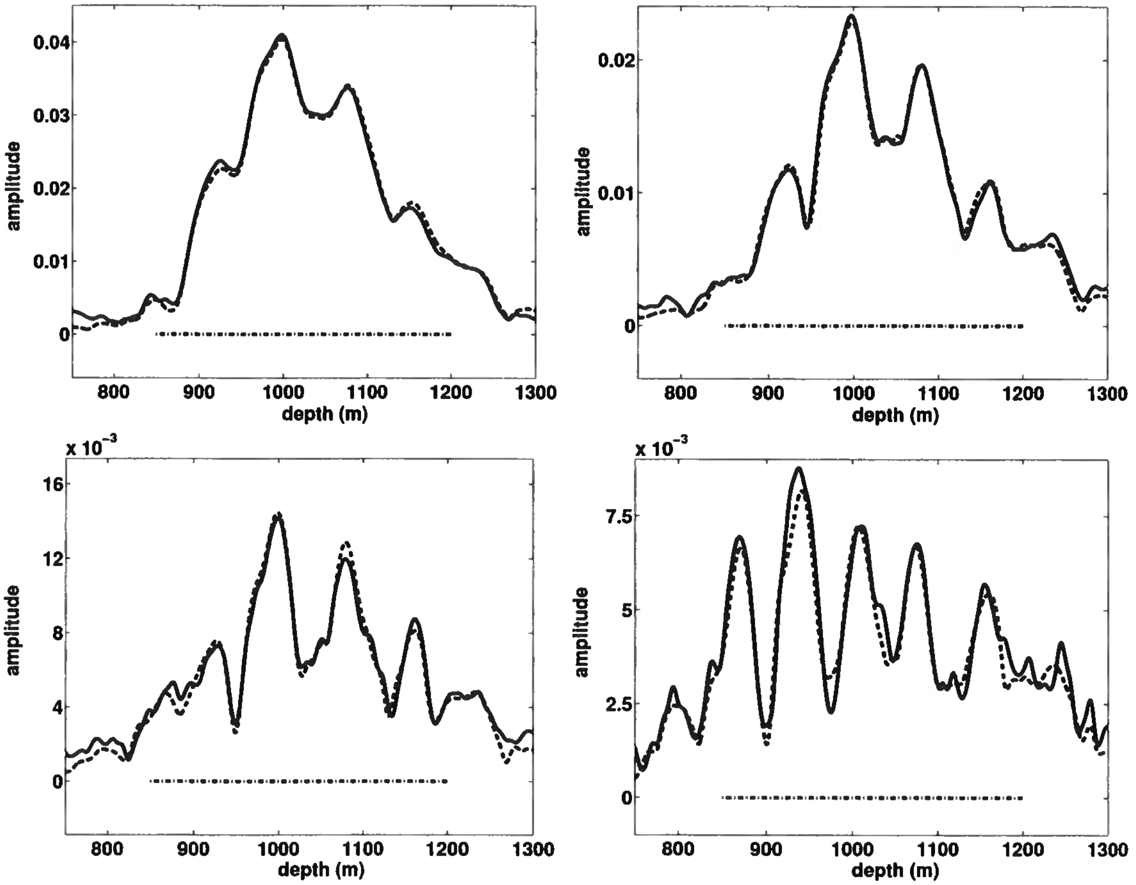

Figure 4.10. Amplitude along fault-plane for Models (clockwise from the upper left) 2 (upper-left), 3 (upper-right), 4 (lower-left), and 1 (lower-right). The amplitude is plotted as a function of depth on the fault-plane and the extent of the fault-plane is shown with a horizontal line in the bottom portion of each plot. These models represent the situations of: 600-psi pore-pressure difference across the fault (Model 2, upper-left), 300-psi pore-pressure difference across the fault (Model 3, upper-right), 150-psi pore-pressure difference across the fault (Model 4, lower-left), and 0 psi pore pressure difference across the fault; in other words, the juxtaposition contact model (Model 1, lower-right), There is no slip at the fault.

(lower-right panel). The fault-plane extends over the long horizontal line at the bottom of the plots in Figure 4.11. The shorter horizontal line signifies the part of the fault plane that slips. Note that the location of the maximum reflectivity occurs in the part of the fault that is slipping. Also, since the reflection from Slip-Model A, embedded in Model 2, is relatively large compared to the fault-plane reflection for Model 2 alone (as shown in the upper-left plot of Figure 4.9 - an amplitude of 0.14 versus 0.04), the sources of noise and error in the processing do not degrade the amplitude map severely in any of the scenarios. This highlights the efficiency of Slip-Model A in reflecting energy compared to the purely ΔP contrast of Model 2.

The amplitude maps for Slip-Models A, B, C, and D are shown in Figure 4.12. As the normal and shear compliances are decreased in going from Slip-Model A to Slip-Model D, the amplitude of the fault-plane reflection attributable to a slipping interface redcues in the about the same proportion. This occurs because the reflection coefficient is proportional to the compliance for a relatively weakly slipping interface (see Appendix E, equation (E.6)). For the the smallest compliance, Slip-Model D, the magnitude of the reflection is on the same order as that of the reflection caused by the ΔP present in Model 2 (shown in the upper-left plot of Figure 4.9). Hence, this would seem to be a lower limit for compliance for slipping behavior to dominate any ΔP across the fault.

4.10 Relating linear-slip to a pressurized fault

The values for the compliances used in the numerical modeling and shown in Table 4.6 do not, up to this point, have any physical meaning in terms of the pressure locally at the fault. In this section, we relate a slipping interface to an effective-layer model that demonstrates much of the same wave-scattering behavior. With an effective layer described in terms of its thickness, density, and velocity, the empirical relationships between effective stress and density, and effective stress and velocity, derived in Chapter 1 can give the compliance values a physical meaning. The derivation here is for normally incident P-waves, but can be extended to P-waves incident at an angle. We focus on normally incident P-waves since the seismic imaging discussed in previous sections utilized PP-scattered waves at small incidence angles.

The effective-layer model begins from a weak scattering assumption. For a thin layer, if the interface reflection coefficients at the upper and lower boundary are small, then the entire series of reverberations (Aki & Richards, 1980) within the layer can be neglected. The total reflection coefficient from the thin layer can thus be approximated simply as the sum of the reflections off the upper and lower interface. For the case when the thin layer is sandwiched between two identical media,

$$R_{tot} \approx R_{PP} \; - \; R_{PP} \; \exp\left(\frac{2i\omega h}{\alpha_L}\right), \tag{4.9}$$

where R_{PP} is the P-wave to P-wave (PP) reflection coefficient at the upper interface (the reflection at the lower interface is $-R_{PP}$), ω is the frequency, h is the thickness of the thin layer, and α_L is the P-wave velocity in the thin layer. In equation (4.9), we have assumed

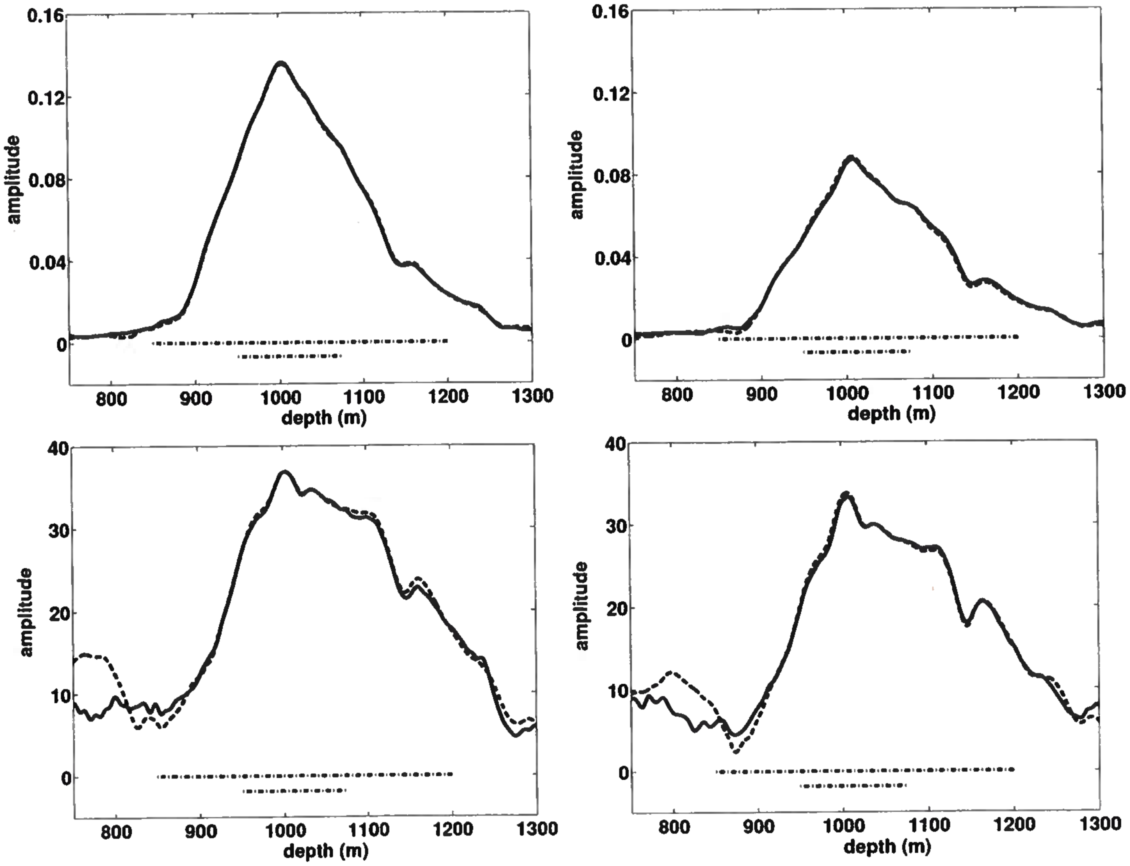

Figure 4.11. Amplitude along fault-plane for Slip-Model A (see Table 4.6) at a fault embedded in Model 2 (see Table 4.3) for four different processing scenarios. The amplitude is plotted as a function of depth on the fault-plane and the extent of the fault-plane is shown with a long horizontal line in the bottom portion of each plot. The sub-portion of the fault that slips is shown beneath this line with a shorter horizontal line. The processing scenarios are the same as those described in the caption for Figure 4.8. The Slip-Model uses slip at the fault to represent weakness caused by elevated pore pressure.

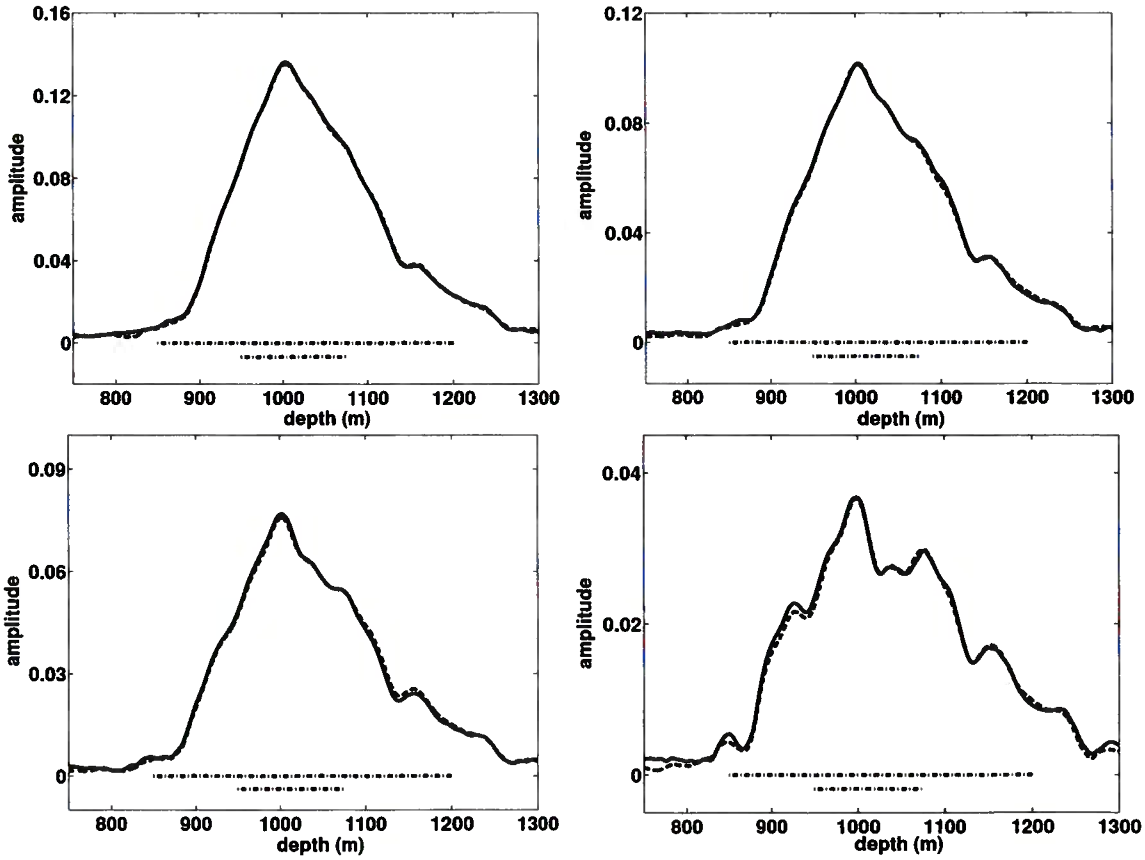

Figure 4.12. Amplitude along fault-plane for Slip-Models A (upper-left), B (upper-right), C (lower-left), and D (lower-right) shown in Table 4.11 at a fault embedded in Model 2 having a pore pressure contrast of 600 psi across the fault. The amplitude is plotted as a function of depth on the fault-plane and the extent of the fault-plane is shown with a long horizontal line in the bottom portion of each plot. The sub-portion of the fault that slips is shown beneath this line with a shorter horizontal line. The maximum amplitude occurs near the center of the slipping portion of the fault in each slip-model. The amplitude map also resembles a triangle since it is in essence the convolution of two boxcar functions: the slipping portion of the fault-plane and the dip filter. In moving from Slip-Model A to D, the compliance of the fault slip becomes smaller and, as a result, the reflection magnitude scales in the same proportion, as predicted by equation (E.6) in Appendix E for a weakly slipping interface. The Slip-Models use slip at the fault to represent weakness due to elevated pore pressure.

that the impedance difference between the thin layer and the host medium is small enough that the transmission coefficients in moving from the host medium into the thin layer and vice versa are close to 1. This is consistent with the weak-scattering assumption made above.

The next approximation relies on the layer being sufficiently thin. If, for the argument of the exponential term in equation (4.9),

$$\frac{2\omega h}{\alpha_L} \ll 1, \tag{4.10}$$

then the exponential can be expanded to first order in a Taylor series

$$\exp\left(\frac{2i\omega h}{\alpha_L}\right) \approx 1 + \frac{2i\omega h}{\alpha_L}. \tag{4.11}$$

Note that the condition in equation (4.10) states that $1 \gg 4\pi h/\lambda_L$, where λ_L is the wavelength of the wave in the thin layer. Hence, the condition means that only a fraction of a wavelength fits in the layer. Inserting the Taylor series approximation into equation (4.9) gives

$$R_{tot} \approx -R_{PP}\,\frac{2i\omega h}{\alpha_L}. \tag{4.12}$$

This expression shows that the total reflection from a thin weak layer is proportional to the derivative of the incident wave. Widess has discussed this fact in a famous paper on vertical seismic resolution (Widess, 1973).

From equation (E.6) in Appendix E, the PP reflection coefficient for a weakly-slipping interface between two identical media (the host medium) is

$$R^s_{PP} \approx \frac{i\omega\eta_N\rho\alpha}{2}, \tag{4.13}$$

where ω is the frequency, η_N is the normal compliance, ρ is the density of the host medium, α is the P-wave velocity of the host medium, and the superscript s indicates that this is the reflection coefficient for a slipping interface. This equation comes with its own assumption, namely that the dimensionless normal compliance is much smaller than 1, $\omega\eta_N\rho\alpha \ll 1$. Equating this expression to equation (4.12) gives

$$\frac{i\omega\eta_N\rho\alpha}{2} = -R_{PP}\,\frac{2i\omega h}{\alpha_L}. \tag{4.14}$$

By canceling common factors and solving this for η_N, the normal compliance, we get

$$\eta_N = -\frac{4h}{\rho\alpha\alpha_L}\,R_{PP}. \tag{4.15}$$

In the weak scattering approximation, we can substitute a weak-scattering approximation for the interface reflection coefficient R_{PP}. This can be obtained from equation (E.6) in

Appendix E

$$R_{PP} = \frac{1}{2}\left(\frac{\Delta\rho}{\bar{\rho}} + \frac{\Delta\alpha}{\bar{\alpha}}\right), \tag{4.16}$$

where $\Delta\rho = \rho_L - \rho$, $\bar{\rho} = (\rho_L + \rho)/2$, $\Delta\alpha = \alpha_L - \alpha$, and $\bar{\alpha} = (\alpha_L + \alpha)/2$. Rewriting equation (4.16) in terms of the properties of the layer and host medium,

$$R_{PP} = \frac{\rho_L - \rho}{\rho_L + \rho} + \frac{\alpha_L - \alpha}{\alpha_L + \alpha}. \tag{4.17}$$

Substituting into equation (4.15) for R_{PP} yields

$$\eta_N = \frac{4h}{\rho\alpha\alpha_L}\left(\frac{\rho - \rho_L}{\rho + \rho_L} + \frac{\alpha - \alpha_L}{\alpha + \alpha_L}\right). \tag{4.18}$$

Since η_N is always greater than zero, the effective thin layer can have relatively lower density $\rho > \rho_L$ and lower velocity $\alpha > \alpha_L$ than the host medium. This holds for a locally pressurized fault, since velocity and density decrease with increase in pore pressure.

It is interesting to compare equation (4.18) with the expression by Schoenberg (1980) for the compliance of a thin weak layer. Schoenberg (1980) relates the compliance to the properties of the layer by stating that, in the limit of $h \to 0$ and $\rho_L\alpha_L^2 \to 0$, the effective compliance of the thin layer is

$$\eta_N = \frac{h}{\rho_L\alpha_L^2}. \tag{4.19}$$

Equation (4.19) is somewhat different than equation (4.18), most notably in that equation (4.19) contains material properties of the layer only and not those of the host medium. The source of the difference between these two expressions is that the result of Schoenberg (1980) holds as $h \to 0$ and $\rho_L\alpha_L^2 \to 0$; that is, it is a strong-scattering approximation. The approximation that we have made in equation (4.18) is a weak-scattering one. A weak-scattering approximation should be more appropriate for an overpressurized fault since, according to the pore pressure relationships described in Chapter 1, $\rho_L\alpha_L^2 \to 0$ cannot happen for any value of the pore pressure. Schoenberg's analogous conditions for shear waves may be more realistic, since the shear velocity goes to nearly zero at zero effective stress (Zimmer *et al.*, 2002).

Using the finite-element code described in Chapter 3, we now test the above approximation by comparing the reflection from a weakly slipping fracture with the reflection from its effective weak thin layer. We use a 10-m thick layer with $\alpha_L = 2077$ m/s and $\rho_L = 2124$ kg/m^3 in a background medium of $\alpha = 2675$ m/s and $\rho = 2260$ kg/m^3. The layer thickness, α_L, and ρ_L are taken from the results in Table 4.10 described below. The background medium parameters are the average values of the sand/shale sequence in Table 4.2. The normal compliance η_N predicted by our weak-scattering model, equation (4.18), for these parameters is 5×10^{-10} m Pa^{-1}. For the Schoenberg model, equation (4.19), the normal compliance comes out to be 1.1×10^{-9} m Pa^{-1}. The source frequency in the simulation is peaked at 20 Hz, just as it was in the SEM modeling shown earlier in this chapter. The result of the finite-element simulation is shown by the traces in Figure 4.13. We find that our weak-scattering effective-layer model is in much better agreement than Schoenberg's model (Schoenberg, 1980). Our model is in error by 15% while the Schoenberg model is in error by 136%. This supports the weak-scattering model for equivalent thin layers and weakly slipping interfaces.

Using the effective-stress relationships from Chapter 1 for ρ_L and α_L in the case of unloading, $\rho^u_L(\sigma_d)$ and $\alpha^u_L(\sigma_d)$, and fixing the depth (or, equivalently the lithostatic stress σ_v) so that the effective stress varies only with pore pressure ($\sigma_d = \sigma_v - p$), the compliance of a fracture can be put in terms of the thickness of the layer and the pore pressure

$$\eta_N(h,P) = \frac{4h}{\rho\alpha\alpha^u_L(P)}\left(\frac{\rho-\rho^u_L(P)}{\rho+\rho^u_L(P)} + \frac{\alpha-\alpha^u_L(P)}{\alpha+\alpha^u_L(P)}\right). \tag{4.20}$$

Note that we use the unloading relationships for ρ_L and α_L. This is because a locally pressurized fault likely results from fluid migrating up the fault, as shown in Chapter 6. Hence, the correct curve to use is the unloading curve (Revil & Cathles, 2002). This curve requires another parameter, the maximum past effective stress σ_{max} that the fault rock experienced before being unloaded to its current state. With this information, the slip models used in the previous modeling section can be related to an effective layer described by four parameters: fault zone of thickness h, fixed depth z, excess fluid pressure $P - P_h$, and maximum past effective stress σ_{max}. Figure 4.14 shows how, given a maximum past effective stress σ_{max} and fault zone thickness h, one can construct equivalent compliances for the velocity and density values traced out along the unloading curve as a function of effective stress. To convert from effective stress to pore pressure, knowledge of the depth z or lithostatic level σ_V in necessary.

The upshot of all this is that the pore-pressure value corresponding to a linear-slip interface is not unique - it depends on three other parameters besides the pressure. In Tables 4.7 through 4.10, we fix two of these parameters - the depth of the fault zone (1850 m) and the thickness of the fault zone (10 m). The tables show the values of the effective thin layer for each Slip-Model, A through D, while varying σ_{max} between the different tables: σ_{max} = 2800 psi in Table 4.7, σ_{max} = 2400 psi in Table 4.8, σ_{max} = 2000 psi in Table 4.9, and σ_{max} = 1600 psi in Table 4.10. They also show the effective stress corresponding to those values of velocity and density along the unloading path, and use the depth to convert to pore pressure. I do not show results for the variation with thickness h since it is mundane, as seen in equation (4.18). The variation with depth z is also fairly unimportant since it changes only the value of the pore pressure for a given effective stress. As seen in Tables 4.7 through 4.10, certain values of the compliance cannot even exist for some values of σ_{max} since the compliance does not fall in the range of possible compliances based on the values of density and velocity. This is shown in Figure 4.14, where in the bottom panel the possible compliance values corresponding to the unloading path in the upper figures does not extend all the way to zero. Hence, some small compliance values cannot be modeled for those choices of h, z, and σ_{max}. In order to get smaller compliance values, the thickness of the fault would need to be made smaller because the compliance, from equation (4.18), scales with h. From the Tables 4.7 through 4.10, we find that the earlier that the rock in the fault zone began to be unloaded, i.e., the smaller the σ_{max}, the larger the compliance

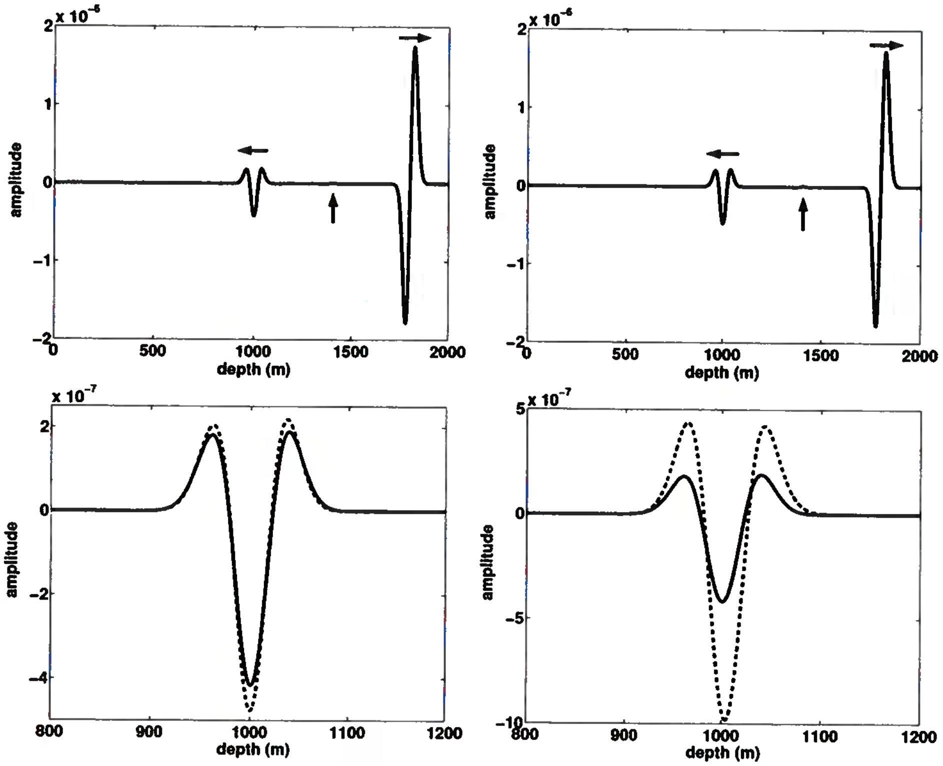

Figure 4.13. A test of the effective layer for a linear-slip fracture for a normally-incident P-wave. These traces are the result of the finite-element code described in Chapter 4. The upper-left panel shows a transmitted plane wave (traveling to the right) and a reflected plane wave (traveling to the left) from a horizontal thin bed of 10-m thickness with density and velocity values from Table 4.10. The background medium has $alpha$ = 2675 m/s and ρ = 2260 kg/m^3 (the average values of the hydrostatic sand/shale layers shown in Table 4.2). The upper-right plot shows the same picture for the equivalent linear-slip interface with compliance calculated from equation (4.18). In the lower-left panel, a zoom in of the reflected waves for the thin bed (solid) and the equivalent linear-slip interface (dashed) are shown. The reflection from the equivalent linear-slip interface, equation (4.18), is in error by 15%. The lower-right panel shows the comparison between the reflection from the thin bed (solid) and the equivalent linear-slip interface (dashed) from Schoenberg (1980). The reflection from Schoenberg's equivalent linear-slip interface, equation (4.19), is in error by 135% likely because it is a strong scattering approximation.

Slip-Model	ρ (kg/m^3)	v$_p$ (m/s)	σ_e (psi)	p (psi)
A	2204	2019	11	5490
B	2207	2175	88	5412
C	2216	2293	322	5178
D	2269	2472	1655	3845

Table 4.7. Four different slip-interfaces described in terms of their effective layer parameters assuming a thickness of 10 m. The estimates are made under the assumption that the fault rock began its unloading path after reaching a maximum vertical effective stress of 2800 psi. For Tables 4.7-4.10 relationships between velocity and pore pressure derived in Chapter 1 are used to relate these compliances to vertical effective stress σ_e and pore pressure p at South Eugene Island. Also, for the four tables, the pore-pressure estimate assumes a depth of 1850 m, where the overburden stress is 5500 psi and the hydrostatic pressure is 2800 psi.

Slip-Model	ρ (kg/m^3)	v$_p$ (m/s)	σ_e (psi)	p (psi)
A	2178	2037	31	5469
B	2186	2192	238	5262
C	2208	2301	775	4725

Table 4.8. Four different slip-interfaces described in terms of their effective layer parameters assuming a thickness of 10 m. The estimates are made under the assumption that the fault rock began its unloading path after reaching a maximum vertical effective stress of 2400 psi. There is no effective-layer model for Slip-Model D along this unloading path.

can be for smaller amounts of pore pressure. Hence, the more efficient the pressurized fault zone can be in scattering seismic waves for a small amount of pore pressure increase.

In the A10ST well at South Eugene Island, the effective stress in the B-fault zone was measured at as low as 166 psi (Losh *et al.*, 1999). In fact, Losh *et al.* (1999) state that "... the fault itself ... is at significantly lower vertical effective stress than the downthrown sediments." In other words, the fault itself is overpressured. Hence, some of the low values for effective stress shown in Tables 4.7 through 4.10, while unusual, are entirely possible for the growth faults at South Eugene Island. Anomalously low effective stresses of 575 psi and 807 psi were also measured in the nearby A20ST well as it crossed the A-fault system (Losh *et al.*, 1999).

4.11 Conclusion

We have presented a complete numerical modeling experiment by utilizing an SEM implementation of the 2D elastic wave equation and processing the resulting waveforms into

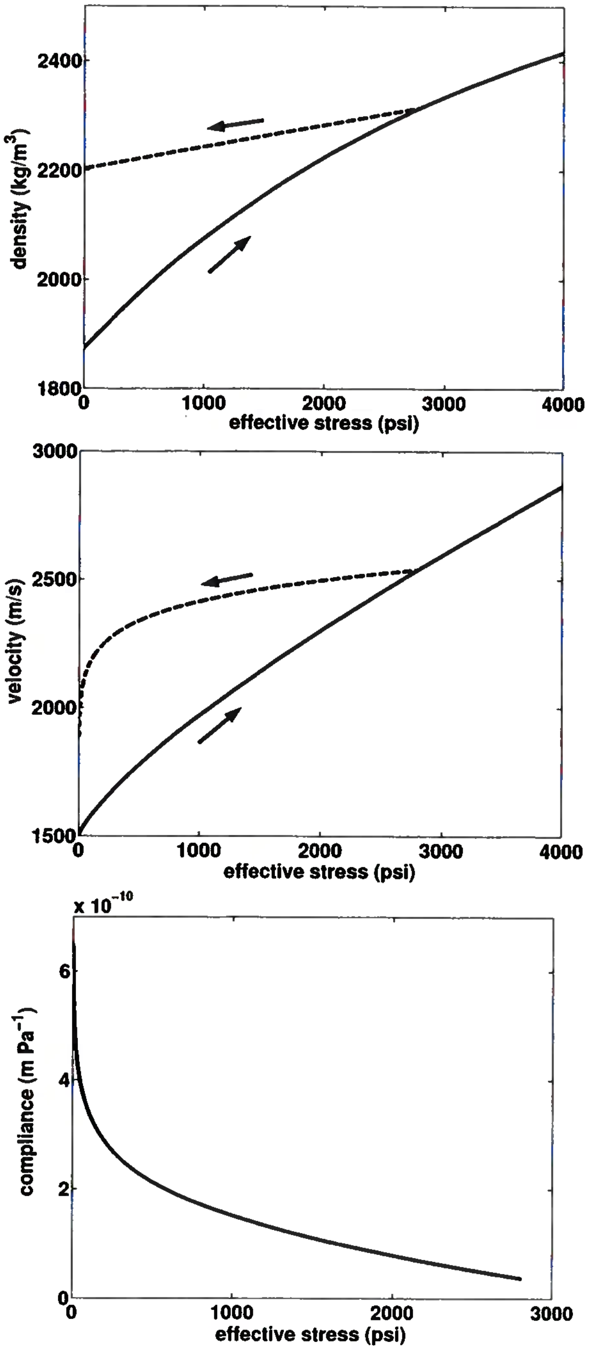

Figure 4.14. The unloading paths for density and velocity used for the values in Table 4.7. Also shown is the compliance for the effective layer model along the unloading path for a 10-m thick fault using equation (4.18). Note that the compliance values end at 2800 psi - the maximum past effective stress σ_{max} for this model.

Slip-Model	ρ (kg/m^3)	v$_p$ (m/s)	σ_e (psi)	p (psi)
A	2149	2058	109	5391
B	2172	2203	700	4800
C	2218	2292	1829	3671

Table 4.9. Four different slip-interfaces described in terms of their effective layer parameters assuming a thickness of 10 m. The estimates are made under the assumption that the fault rock began its unloading path after reaching a maximum vertical effective stress of 2000 psi. There is no effective-layer model for Slip-Model D along this unloading path.

Slip-Model	ρ (kg/m^3)	v$_p$ (m/s)	σ_e (psi)	p (psi)
A	2124	2077	453	5047

Table 4.10. Four different slip-interfaces described in terms of their effective layer parameters assuming a thickness of 10 m. The estimates are made under the assumption that the fault rock began its unloading path after reaching a maximum vertical effective stress of 1600 psi. There are no effective layer models for Slip-Models B, C, and D along this unloading path.

their time-migrated images. We derived a simple dip filter and used it to isolate fault-plane reflections. We then exploited the relationships between the elastic parameters, density and velocity, to create physically meaningful models of sealing faults that maintain a ΔP of up to 600 psi. For these ΔP models, we assumed that the overpressure mechanism is purely due to undercompaction. In the course of this modeling, we found that the minimum ΔP necessary to give rise to substantial fault-plane reflections is on the order of 150 psi. Taking advantage of the SEM modeling code's ability to accommodate linear-slip interfaces, we selected four different values of the normal and shear compliances for the fault interface. We find that the slipping interfaces are more efficient at scattering seismic energy than are the pore pressure differences across the fault for compliance values above $\sim 10^{-10}$ m Pa^{-1}. Unsatisfied with the lack of physical insight into the meaning of a compliance, we derived, from a weak-scattering model, an equivalent thin, weak layer that gives virtually the same reflection as a linear-slip interface under certain conditions. We used this equivalent layer model to relate the values of the compliance to realistic values of pore pressure at South Eugene Island. To do so required extensive use of the effective-stress relationships for the unloading paths derived in Chapter 1. We finally concluded that the smaller the past maximum effective stress is for the fault zone rock, the more efficient the fault can be at scattering seismic waves. This makes sense physically in that the overpressured fault rock is being poroelastically perturbed (by, for instance, fluid migrating up the fault) from a more extreme initial state.

Chapter 5

Fault-plane reflections as a diagnostic of pressure differences in reservoirs: a case study

5.1 Summary

Seismic data taken at Blocks 314, 315, 330, and 331 of the South Eugene Island field contain reflections from a major growth fault. Out of a number of possible causes, we find that differences in pore pressure across the fault give rise to the fault-plane reflections. The pressure differences are detectable because pore pressures that exceed the hydrostatic pressure, or overpressures, lower the seismic velocity. Thus, the presence of the reflections point to the fault providing a significant seal. We develop a processing scheme to highlight the fault-plane reflections while simultaneously suppressing the reflections from the layered structure. Using this processed data set, we extract the amplitude of the reflections from the fault-plane itself. The areas of strong reflection amplitude correlate well with the geology and known areas of overpressure. This work was done in collaboration with Jon Sheiman (Shell), Roel Snieder (CSM), Jay Busch (Shell), Steven Naruk (Shell), and Scott Wilkins (Shell).[1]

5.2 Introduction

The importance of faults as delimiters of compartments in hydrocarbon reservoirs cannot be stressed enough. The role of faults, however, is complicated by their dual nature as both fluid seals and conduits. Classifying a fault as one or the other typically demands extensive knowledge of a basin's geologic history, core samples, and well logs. Only recently have geophysicists begun to incorporate conventional seismic data into the evaluation of fluid pressure near faults (Dutta, 1997; Huffman, 2002). The method relies on seismic waves detecting the presence of pressure changes in the subsurface (Pennebaker, 1968), and, when successful, manages to predict regions of overpressure that affect drilling operations.

Evidence of faults can often be seen on migrated seismic data. Automated fault identification algorithms avoid the tedious picking of faults in 3D volumes of seismic data Townsend *et al.* (1998). According to Sheriff (1984), the imprints of faults on seismic data are: "(a) abrupt termination of events, (b) diffractions, (c) changes in dip, (d) distortions of dips seen

---

[1] Published in an EAGE proceedings on "Fault and Top Seals: What do we know and where do we go from here?" (Haney *et al.*, 2004); in addition, to be submitted to the AAPG Journal.

through the fault, (e) deterioration of data beneath the fault producing a shadow zone, (f) changes in the pattern of events across the fault, and (g) occasionally a reflection from the fault plane." Items (a), (c), and (f) provide indirect evidence of faults and form the basis of automated fault identification. Problems with how time migration treats lateral velocity variations lead to items (d) and (e). Here, we address the last point; namely, what are the occasional fault-plane reflections telling us about the nature of the fault itself?

Several fault-zone models describe different aspects of the seismic properties of a fault. One possibility is that the fault is a linear-slip interface (Worthington & Hudson, 2000; Schoenberg, 1980). Physically, this means that the fault is a zone of low shear modulus. Another model takes into account that the fault may be a barrier to lateral fluid flow. A high shale content in the fault gouge causes fluid pressures to build up on one side of the fault. As a result, the adjacent sediments are undercompacted, and subsequently have lower velocities (Dutta, 1997). Because of throw across the fault, lithological (sand/shale) contacts across a fault can also contribute to reflections from the fault-plane (Sheriff, 1984; Yielding *et al.*, 1991). A main difference in these models is that reflection from a low-shear zone acts as a high-pass filter; in essence, the fault zone is a thin bed. The magnitude of the reflection in this case depends on the seismic properties and thickness of the zone. Pore pressure and lithologic differences (away from diffractions) across a fault act as traditional seismic interfaces that preserve frequency in the reflection process. A true fault zone could be a combination of two or more of these models.

Here, we show that, at the South Eugene Island field, fault-plane reflections from a major growth fault, known as the A-fault, arise from pore pressure differences across the fault. We focus on this fault since previous studies (Losh *et al.*, 1999) suggest that it serves as a significant barrier to lateral fluid movement. The strength of the fault-plane reflections varies along strike and dip of the A-fault. We make the correlation between areas of fault-plane reflections and areas of strong pressure gradients based on existing well information and known zones of overpressure. No evidence yet suggests that the fault-plane reflections significantly originate from low-shear zones or lithologic contacts.

5.3 Overpressure at South Eugene Island

Growth faults, or syndepositional normal faults, divide the Pliocene-Pleistocene sediments at South Eugene Island into several compartments. Depending on whether or not the faults are significant barriers to fluid flow, the individual compartments can be overpressured. For instance, Losh *et al.* (1999) report an increase of more than 780 psi in pore pressure over a distance of 18 m while drilling through the A-fault in Block 330 of the South Eugene Island field.

A contour plot of the two-way reflection time from the A-fault is shown in map view in Figure 5.1. The arrow in Figure 5.1 points in the down-dip direction that makes an angle of approximately 50° with the horizontal. The A10ST well, where Losh *et al.* observed a large pore pressure jump, intersects the fault on the lower right.

Several mechanisms effectively cause anomalously high pore pressures in the subsurface (Bowers, 1995; Dutta, 1997; Huffman, 2002). In the Gulf of Mexico, overpressure commonly

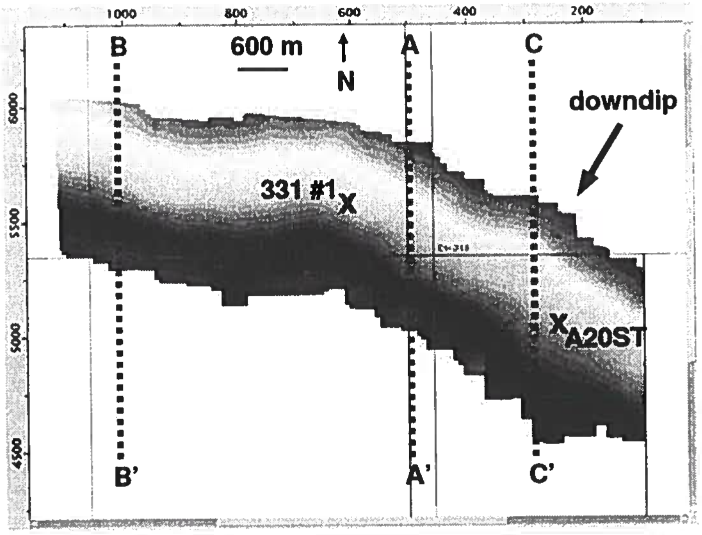

Figure 5.1. Map view of the two-way reflection time from the A-fault. The arrow points in the downdip direction. Two wells are shown by an X where they intersect the fault-plane. The locations of three seismic lines used in other figures are also shown as dashed lines.

results from disequilibrium compaction and dipping sands being bounded above and below by shales. Following the onset of disequilibrium compaction, the relatively high permeability of the sands allows additional fluid pressures from depth to move into high points of subsurface structure. Termed unloading, this mechanism results in an additional decrease in seismic velocity due to poroelastic expansion of the pores. More specifically, the high pore pressure causes a decrease in the vertical effective stress and, as a result, a decrease in the area of grain-to-grain contacts.

We have identified anomalous decreases in velocity from a constrained Dix-type inversion Toldi (1985) on the South Eugene Island data. Line C-C′ (see Figure 5.1) from this velocity cube is displayed in Figure 5.2. The velocity at marker '1' monotonically increases with depth. This represents the velocity variation resulting from the normal compaction trend. On the left side of this plot, between markers '2' and '3', a noticeable decrease in velocity occurs with increasing depth. Experience has shown that, in the Gulf of Mexico, such a decrease in velocity with depth is due to high pore pressures rather than lithology (Dutta, 1997). The spatial pattern of the relatively higher velocity pocket at '2' corresponds to the trend of the A-fault, providing evidence from the seismic data that the overpressures are related to the A-fault.

Zones of overpressure can be monitored while drilling from the rate of penetration of the drill bit into the formation (Jordan & Shirley, 1966). Such a method suffices for detecting the gradual build up of overpressure above a moderately sealing shale. By moderately sealing, we mean that the pressure front has, over geologic time, diffused somewhat

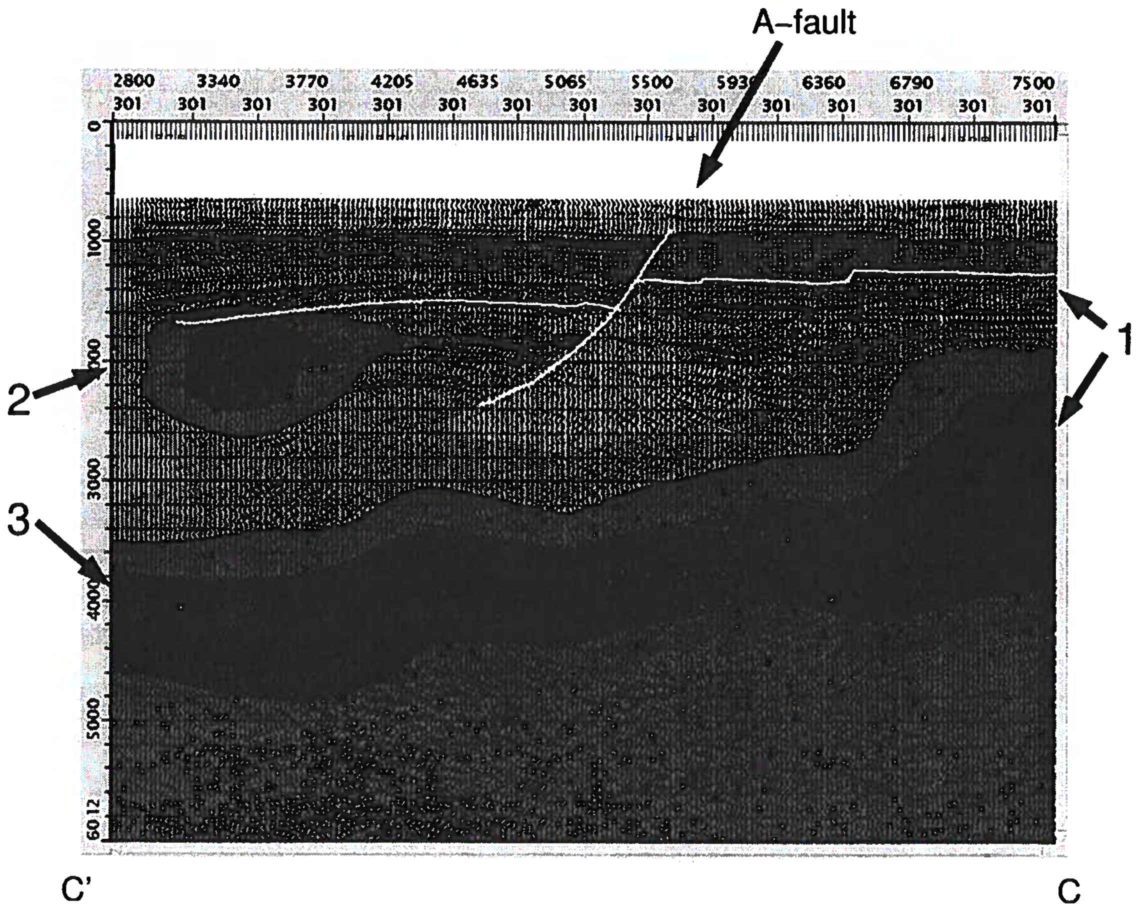

Figure 5.2. Interval velocities along the C-C′ line at the South Eugene Island field obtained via a smoothed Dix-type inversion (Toldi, 1985). The velocity increases monotonically with depth at marker ‘1’, but experiences a decrease between markers ‘2’ and ‘3’. The decrease in velocity with depth indicates that overpressures are present. The velocity also decreases laterally in moving from the left to right across the A-fault. This is an indicator that the A-fault seals an overpressured compartment on the right. That the normal compaction trend re-establishes itself on the far right, at marker ‘1’, indicates that another fault, to the right of the A-fault, is the other boundary of the overpressured compartment.

through the shale. Any sort of overpressure prediction while drilling should fail when a highly overpressured zone is quickly and unexpectedly encountered. This has motivated the development of pre-drill pore pressure prediction from seismic data.

For a smooth increase in fluid pressure across a moderate seal, the velocity decreases gradually, and a transmitted wave passes through the overpressured region with almost no reflection. However, the most dangerous instances of overpressure occur over distances less than a typical seismic wavelength ($\sim$ 200 m), and therefore, quick onsets of high fluid pressure across a sealing fault give rise to strongly reflected waves. By mapping out the amplitude of fault-plane reflections on the fault-plane itself, areas of sharp increase in pore pressure across the fault, as described in Losh *et al.* (1999), should stand out.

5.4 Isolating Fault-Plane Reflections

The fault-plane reflections at South Eugene Island are typically less prominent than the layer reflections (exceptions to this are discussed in Chapter 6). This may be due to either small reflectivity at the fault or the deterioration of the processing and imaging procedure (Kirchhoff) for steep dips. As a result, the fault image contains "noise" from the horizontal layers terminating at the fault. We employ a simple dip-filtering technique, as described in Chapter 4, along the fault to effectively remove the layers while at the same time accentuating the reflection from the fault plane.

Displayed in Figure 5.3 is a post-stack time migrated section along the A-A$'$ line (see Figure 5.1). Several growth faults stand out in this image. A particularly strong fault-plane reflection cuts through the center of Figure 5.3 - this is the A-fault. To the right, another fault (the C-fault) can be made out from the mismatch of adjacent layers; however, the C-fault does not give rise to a reflection. This is likely because the throw on the A-fault is greater than that on the C-fault. We have highlighted the H-sand as an indicator of the throw on these two faults. The greater the throw on a fault, the more developed its gouge, and, therefore, the more likely it is to be a barrier for lateral fluid flow.

To bring the fault-plane reflections out, we designed an adaptive local dip-filtering routine. Along each trace, we scan over a small angular window for the maximum coherence direction. The range of angles is selected to correspond to the dip of the fault. We then construct the dip-filtered data by summing over the 25 adjacent traces. If the angular window we wish to dip-filter over is too steep, aliasing can occur (see Figure 5.4 for an example of aliasing). When aliasing does occur, the strong reflections from the layers get added back into the dip-filtered data. The result of dip-filtering without aliasing is shown as a wiggle-plot in Figure 5.5 with the migrated image of Figure 5.3 in the background. The horizontal layers effectively cancel in the dip-filtered data, leaving the fault-plane reflections to stand out. Both the amplitude and phase of the fault-plane reflection from the A-fault vary along the fault. The phase seems to change at points where sandstones encounter the fault. For instance, moving up the fault-plane from the bottom, the wavelet changes shape and grows stronger as it moves past the JD-sand. It then vanishes between the downthrown and upthrown segments of the H-sand, only to continue again above the upthrown H-sand.

We do not make quantitative use of the phase since the absolute phase of the reflections

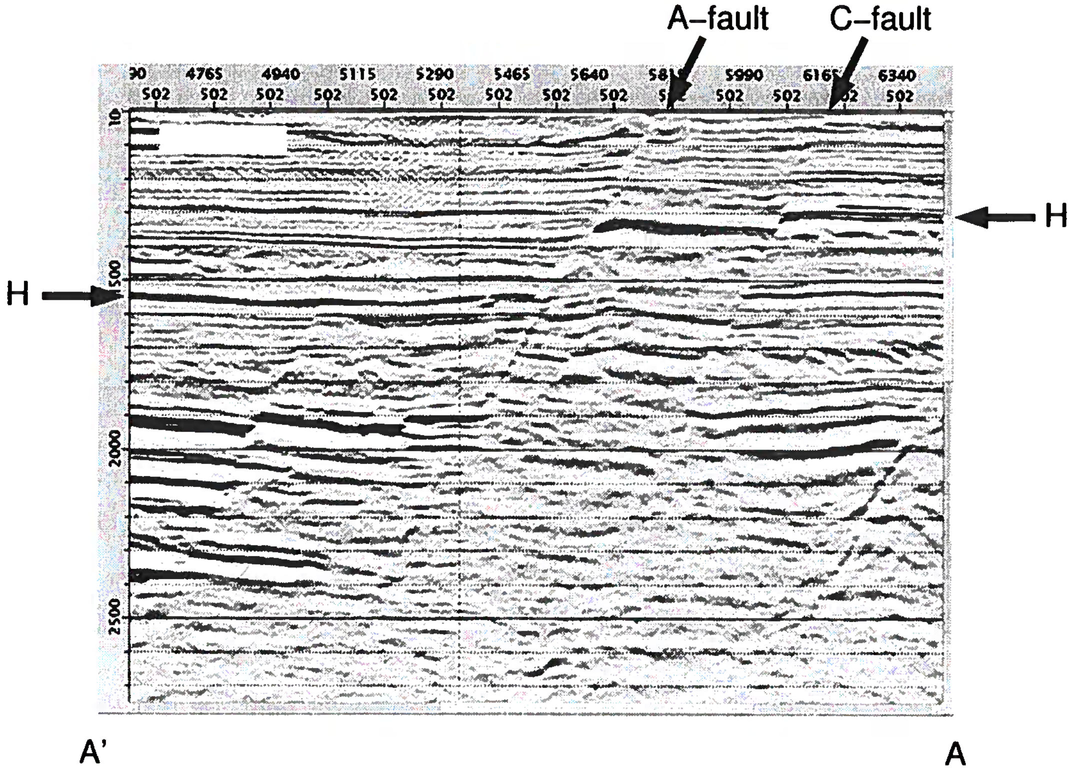

Figure 5.3. A typical fault-plane reflection from the A-fault along the A-A′ line. Shown is the post-stack time-migrated image. The H-sand is marked to show the amount of throw across the fault.

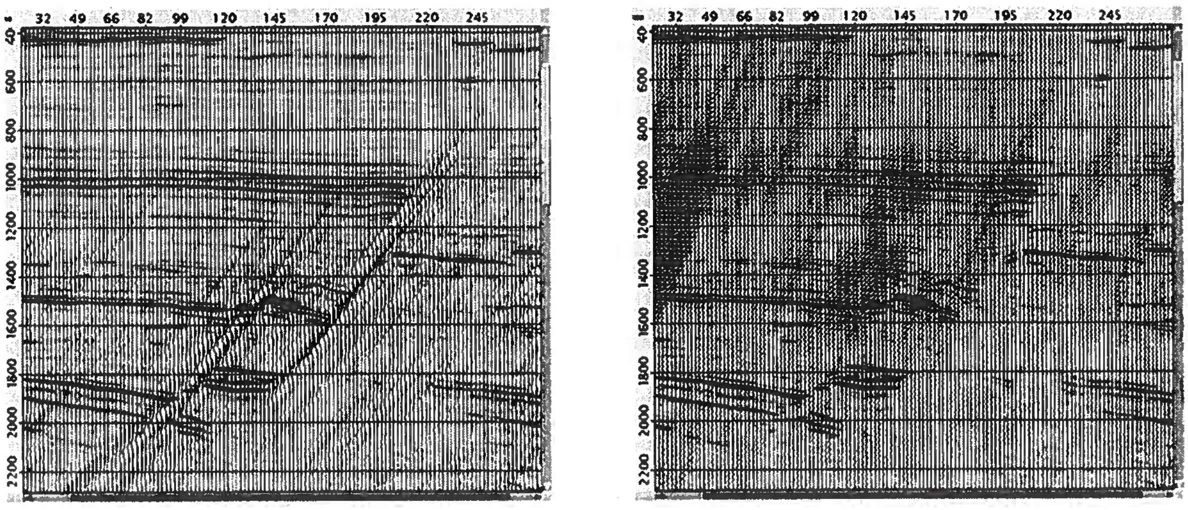

dip–filter fault–plane reflections

aliasing of the dip–filter

Figure 5.4. A test of the dip-filter to show how too steep of a dip leads to aliasing.

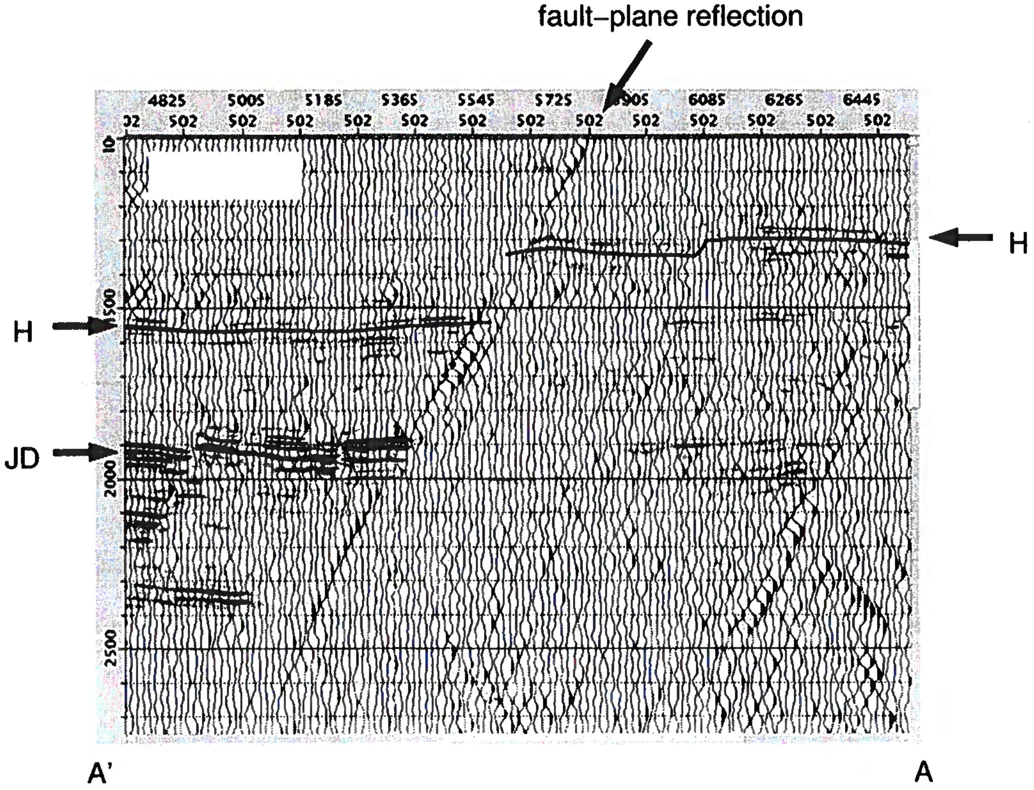

Figure 5.5. Overlay of the time-migrated seismic section from Figure 5.1 with the wiggle-trace slant stack. The fault-plane reflection becomes clearer in the slant stack.

may be contaminated with stacking errors, as discussed in Chapter 2. If the prestack data could be analyzed, the phase would be an excellent indicator of high fluid pressures inside a fault-zone. High fluid pressure in the A-fault has been reported by Losh *et al.* (1999) and leads to vanishingly small shear velocities in the fault. Since scattering from such a linear slip interface is frequency dependent, the phase of the reflected wavelet should change. Though we cannot trust the absolute phase in this post-stack data, we interpret the relative phase changes along the fault to be related to presence of the sands.

We extended the above procedure to 3D to gain a more extensive picture of the variations in fault-plane reflections. By breaking up the 3D seismic data volume into successive 2D planes in the dip direction, we could perform the slant stacking on each plane individually. The slant-stacked lines were then reassembled into a 3D data volume.

5.5 Correlation of Fault-Plane Reflections with Regions of Overpressure

The attributes of the slant-stacked 3D seismic data on the A-fault contain information about the fault seal. We extracted the maximum amplitude along the picked fault-plane (Figure 5.1) within a small time gate. The reflection amplitudes are displayed in map view on the fault plane in Figure 5.6. Higher amplitudes, shown as lighter colors in Figure 5.6, come and go on the fault plane. We discuss the details of the reflections between the dashed lines in Figure 5.6.

The area on the A-fault plane between the two dashed lines contains most of the strong fault-plane reflections and has geologic meaning. The time-migrated image and the dip-filtering along the B-B′ line (see Figure 5.6) are shown in the bottom panel of Figure 5.7. Actually, the bottom panel of Figure 5.7 is the sum of two dip-filtered images taken in opposite directions. We look in these two directions since faults form antithetic pairs in a vertical section in extensional regimes such as the Gulf of Mexico. In the two upper panels of Figure 5.7, we plot the two individual dip-filtered images prior to summing them together. On the downthrown side of the A-fault, shown on the left in Figure 5.7, the intersection of the seal with the A-fault corresponds to the lower white dashed line in see Figure 5.6. This seal is the shale immediately above a layer known as the JD-sand. The fact that this is the main seal between hydrostatic and overpressured sediments in the sedimentary column on the downthrown side has been mentioned by other authors before (Stump *et al.*, 1998; Revil & Cathles, 2002) based on fluid pressure measurements and well logs. It is also discussed in Chapter 1 of this thesis. The lack of strong amplitudes south of the lower white dashed line in Figure 5.6 means that the A-fault does not reflect below the JD horizon, since both its upthrown and downthrown sides are overpressured at that depth. The upper white dashed line in Figure 5.6 marks the intersection of the A-fault with the seal on the upthrown side shown in Figure 5.7 on the right. Revil & Cathles (2002) have implicated this shale layer, directly above the H-sand, as the seal on the upthrown side. The lack of strong amplitudes north of the upper white dashed line in Figure 5.6 means that the A-fault does not reflect above the top of its intersection with the upthrown seal. This suggests that the seal transfers from the downthrown seal to the A-fault and from the A-fault to the upthrown seal in moving from left to right in Figure 5.7. Hence, a

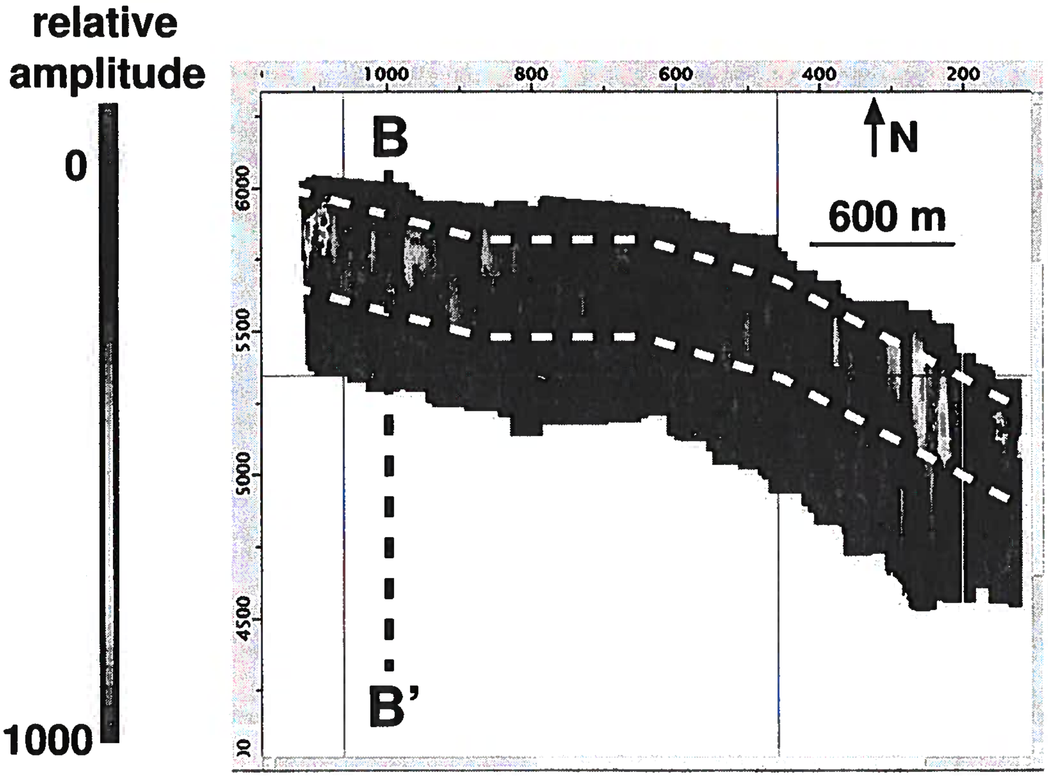

Figure 5.6. Reflection amplitude from the A-fault as a function of position on the fault-plane. Stronger amplitudes show up as hotter colors (red and yellow). The lower white dashed line is the intersection of the shale beneath the JD-sand with the A-fault from the south (the hangingwall side). The upper white dashed line is the intersection of the shale above the H-sand with the A-fault from the north (the footwall side). The fault plane between these two sealing layers separates hydrostatic from overpressured sediments, thereby creating a pressure contrast.

portion of the A-fault acts as the seal, and it is this interval (between the two dashed lines in Figure 5.6) that contains most of the fault-plane reflectivity. The interval is labelled in Figure 5.7 as "reflecting". This interpretation is further supported by Losh *et al.* (1999), wherein the author state that "the fluid pressure differential (across the A-fault) is most pronounced between 1650 and 1950 m depth; above that depth, the extent of overpressuring in less on both sides of the fault, whereas at greater depths, the sediments on both sides of the fault are highly overpressured.

There is other evidence for fault-plane reflections resulting from pore pressure contrasts. Figure 5.8 shows a pair of fault-plane reflections: one that originates from a fault separating hydrostatic from overpressured sediments (the A-fault) and the other from a fault separating overpressured from hydrostatic sediments (the D-fault). In the upper left panel of Figure 5.8, the dip-filtered data is plotted on top of the migrated image, showing the two reflections coming from the A-fault and the D-fault. The upper right panel of Figure 5.8 shows the same dip-filtered data, but now with an inverted velocity field in the background. The velocities represent a smoothed Dix-type stacking velocity inversion (Toldi, 1985). The area between the faults has relatively low velocity, an indicator of overpressure. From the velocity inversion only, we do not know over which length scale the pore pressure contrast occurs; however, the presence of the fault-plane reflections that correlate with the shape of the variable velocity field strongly suggests the pressure contrast is sharp and less than a seismic wavelength. In the middle panels of Figure 5.8, we show the fault-plane reflected waveforms within the dashed boxes of the upper left panel. In the lower panel, we show the amplitude and phase spectrum for the reflected waveforms. At the peak frequency, they are almost 150° different in phase. A 180° difference would be expected from two interfaces that are the opposite of each other (hydrostatic/overpressured vs. overpressured/hydrostatic); however, due to the stacking errors that were discussed in Chapter 2, phase shifts of $\pm 45°$ can occur for each waveform from mis-stacking. Hence, the two waveforms are sufficiently different from each other in phase since the errors of $\pm 45°$ cannot explain the 150° difference. Their true phase difference could be $150° \pm 90°$ depending on the degree of mis-stacking.

Finally, we plot the reflection amplitude from the F-fault in Figure 5.9. The F-fault is known to be a leaky fault (Losh *et al.*, 2002) with only a minimal amount of pore pressure contrast across it ($\sim$ 100 psi). As a result, the amplitude extracted from its dip-filtered version is relatively quiet, especially when compared to the reflection amplitude from the A-fault, which holds back a pore pressure contrast of up to 800 psi. This supports one of the conclusions of Chapter 4, that, below 150 psi of pressure contrast, the presence of the contrast is drowned out by the juxtaposition contacts.

5.6 Conclusions

At the South Eugene Island field, observed fault-plane reflections from the A-fault arise due to pressure differences across the fault. By applying a technique to accentuate the fault-plane reflections, we are able to map out the reflection amplitudes on the fault plane. The spatial distribution of the reflections has a geologic meaning and shows which part of the fault-plane is acting as a seal. Two other examples showed how fault-plane reflections can

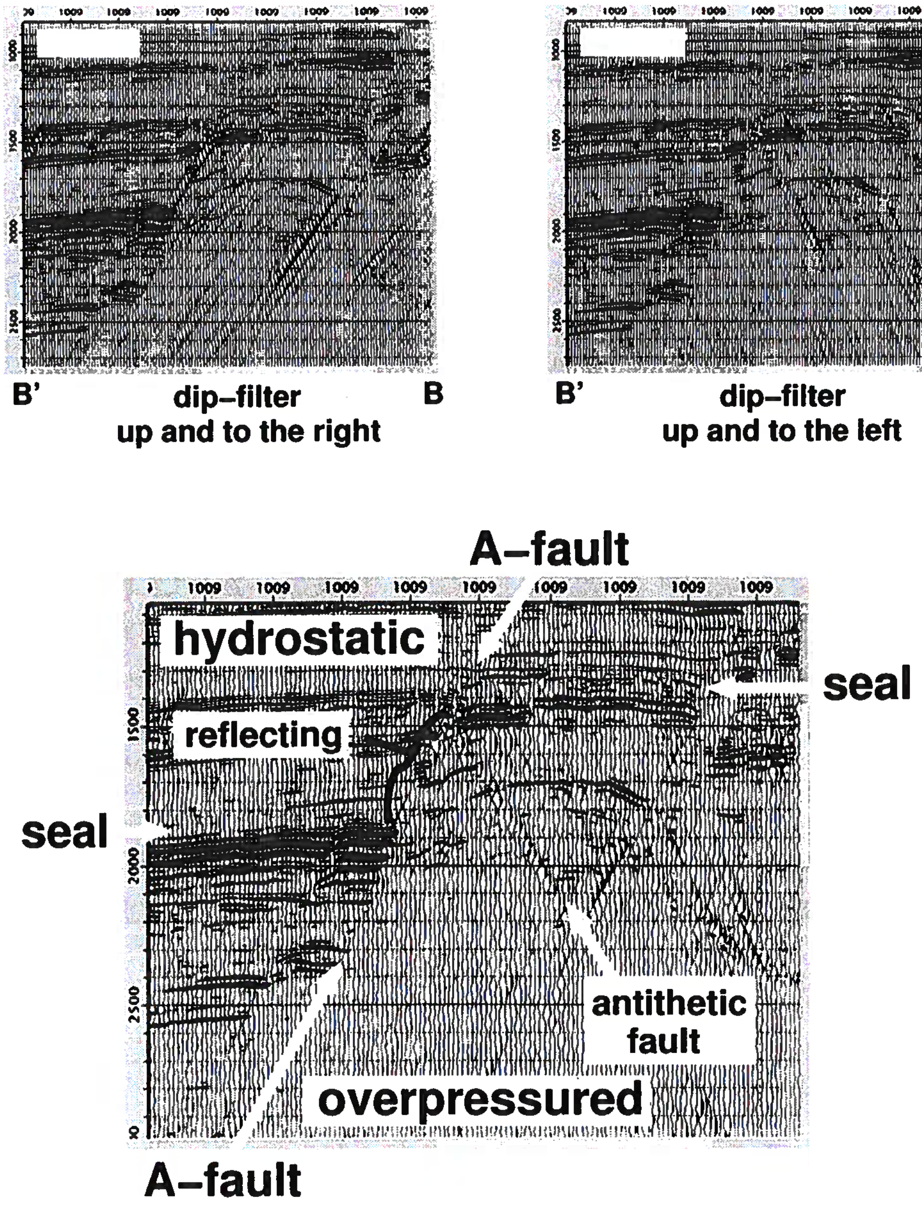

Figure 5.7. In the upper two panels, I show overlays of the time-migrated seismic section along the along line B-B′ with the section for two directions of the dip-filter in wiggle trace. I then sum the two directional dip-filters and overlay the time-migrated seismic section in the lower panel with the summed dip-filtered section. An antithetic fault exists at this location and gives rise to some fault reflectivity. The reflecting part of the A-fault corresponds to the part of it above the downthrown seal (on the left side) and beneath the upthrown seal (on the right side).

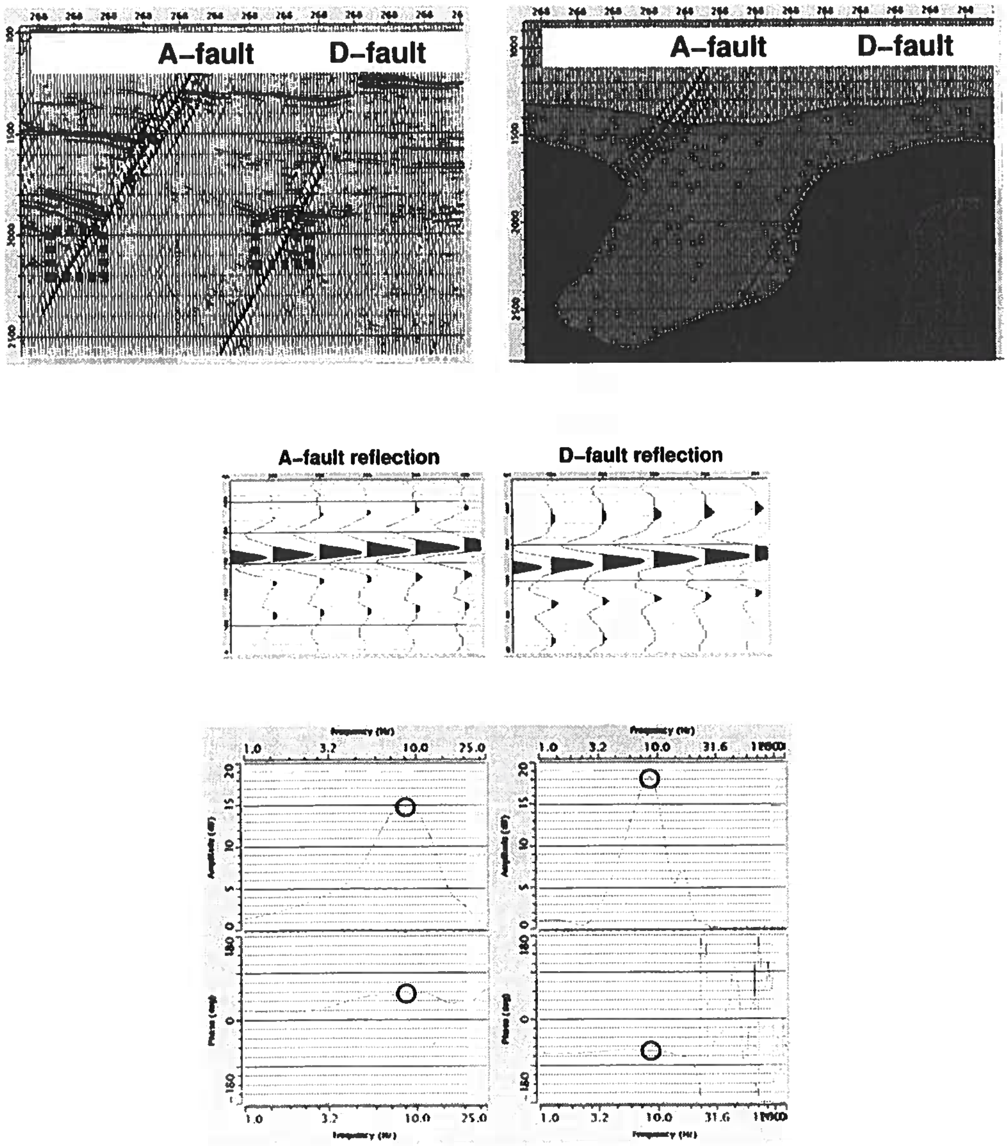

Figure 5.8. A series of panels illustrating a pair of fault-plane reflections that are out-of-phase. See the text for details.

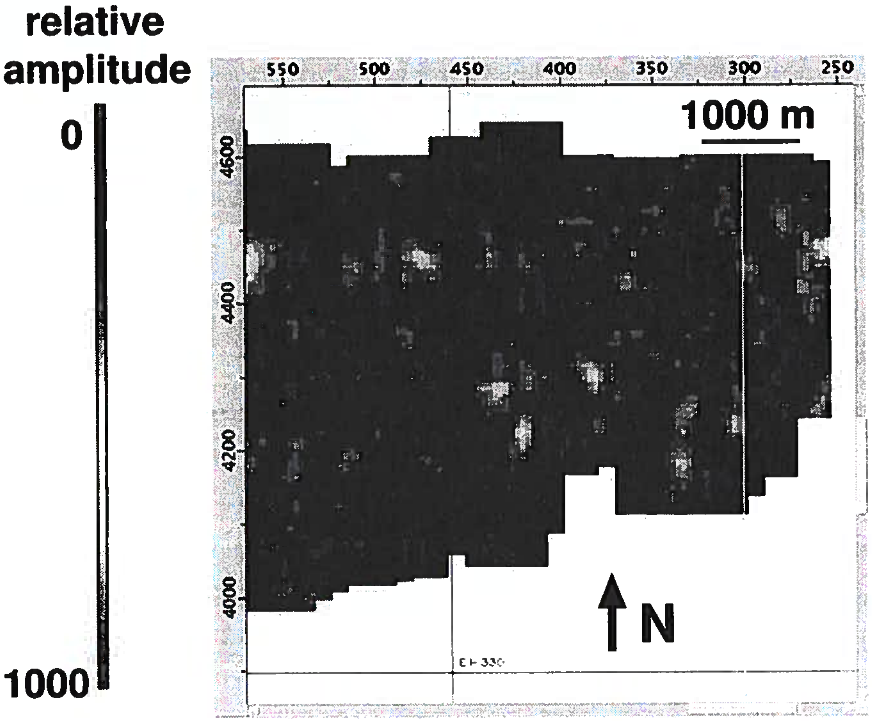

Figure 5.9. Reflection amplitude from the F-fault as a function of position on the fault plane. The F-fault is known to be leaky and holds only up to 100 psi of pore pressure difference. As a result, its reflected amplitude is much smaller than that of the A-fault, which holds up to 800 psi of pore pressure difference. Compare this plot to Figure 5.6, the reflection map for the A-fault.

have different polarities due to different pressure contrasts and how the reflected amplitude vanishes for the leaky F-fault, where hardly any pore pressure contrast exists. Future work will focus on other faults in the South Eugene Island field and attempt to estimate fault-zone properties, particularly fluid properties, from the fault-plane reflections.

Chapter 6

Seismic detection of a spatially-limited fluid pulse ascending a growth fault

6.1 Summary

We report on what is, to our knowledge, the first image of a fluid pulse inside a fault-zone that, based on geochemical evidence, is ascending the fault with time. The fluid pulse is confined to a growth fault (the B-fault) at the South Eugene Island 330 field, offshore Louisiana. Though the thickness of the fault-zone may only be tens of meters, or a fraction of a seismic wavelength, at the location of the fluid pulse, it is detectable because the fluid pulse is of high fluid pressure and, hence, low *P*-wave velocity. We extract the amplitude of the fault-plane reflection from the B-fault by applying a dip-filter to migrated 3D seismic data gathered by Shell in 1992. The reflectivity at the location of the fluid pulse is roughly three times greater than at an unremarkable part of the B-fault where sonic, shear, and density logs passed through the fault in 1993. We modify the logs by placing a slipping interface at the fault-plane, representing a model of the fluid pulse. As discussed earlier in this thesis in Chapter 4, a slipping interface can be thought of as an effective low velocity zone. After generating synthetic seismograms from both the original logs and the modified logs, we find that the slipping interface produces high reflectivity similar to that observed at the fluid pulse. The ability to detect such a spatially-limited, high fluid pressure anomaly has implications for the understanding of hydrocarbon migration mechanisms and the time scale of reservoir-recharge in the Gulf of Mexico.

In addition, we discuss the first observation derived from seismic reflection images of a fluid pulse inside a fault-zone that, based on previous evidence, is suspected to be ascending the fault with time. We find that areas of high fault-plane reflectivity from a growth fault known as the B-fault at the South Eugene Island Block 330 field, offshore Louisiana, systematically move up the fault 1 km between 1985 and 1992. The up dip movement can be explained by the presence of a high pressure fluid pulse ascending a vertically permeable fault-zone. These "fault burps" play a central role in hydrocarbon migration. This work has been done in collaboration with Steven Losh (Cornell), Roel Snieder (CSM), and Jon Sheiman (Shell). [1]

---

[1] submitted and accepted for review as a brief correspondence to Nature

6.2 Introduction

Faults act as zones of highly focused deformation and fluid flow in the subsurface; the exact mechanism of fluid flow and rate of flow along faults are, however, not well understood. For instance, Revil and Cathles (2002) claim that fluids may propagate as solitary waves along faults at the rate of kilometers per year. Since faults deform, or slip, in an episodic manner, it has been postulated that flow along faults should also be episodic and linked to the slip events (Sibson, 1990). Episodic flow along faults may be common in sedimentary basins worldwide. In the Gulf of Mexico, growth faults cutting through young, poorly consolidated sediments provide a means for hydrocarbons generated in deep source rocks to migrate into shallower, economically producible reservoirs.

We have previously established from 3D seismic data collected at the South Eugene Island field, offshore Louisiana, that fault-plane reflections from the main basin-bounding growth fault (the A-fault) indicate the portions over which the fault acts as a lateral seal (Haney *et al.*, 2004). In this brief paper, we extend our interpretation of the seismic data to examine the possibility that the faults at South Eugene Island also act as vertical conduits for fluid migration. Such behavior has been observed during the Global Basins Research Network (GBRN) drilling project at South Eugene Island (Anderson *et al.*, 1995) and highlights the dual nature of faults as both effective lateral seals and vertical fluid migration pathways.

We find that at one location, the intersection of the A10ST well with a fault synthetic to the A-fault, known as the B-fault, high fault-plane reflectivity occurs where a fluid pulse has been documented from drilling records (Losh *et al.*, 1999). Using a logs that passed through part of the B-fault, we perform some simple numerical modeling to estimate the dimensions and properties of a fluid pulse confined to the fault-zone. We conclude that a fracture model, or an effective thin, low velocity zone and low density zone (as shown in Chapter 4) is consistent with the presence of a fluid pulse and could be responsible for the high reflectivity observed at the B-fault. A trade-off exists between the elastic properties of the pulse, its thickness, and the magnitude of its reflection. As a result, more than one fracture model gives an identical reflection.

6.3 Vertical fluid migration at South Eugene Island

The South Eugene Island field displays strong evidence of vertical fluid migration from deep source rocks into its shallow Plio-Pleistocene reservoirs (Revil and Cathles, 2002). This phenomenon has been given the name dynamic fluid injection. Evidence of recent and fast fluid migration up the growth faults comes from the present day oil seeps at the fault scarps on the sea floor (Anderson *et al.*, 1995), the variation in the chemistry of petroleum fluids over the time scale of years (Whelan *et al.*, 2001), and geochemical anomalies observed near the A-fault in the A6ST well (Losh *et al.*, 1999).

Extensive drilling and geologic studies have taken place at South Eugene Island. The best known is the multifaceted GBRN DOE-funded drilling project that took place in the mid-1990's. During late 1993, GBRN intentionally drilled into and successfully cored several

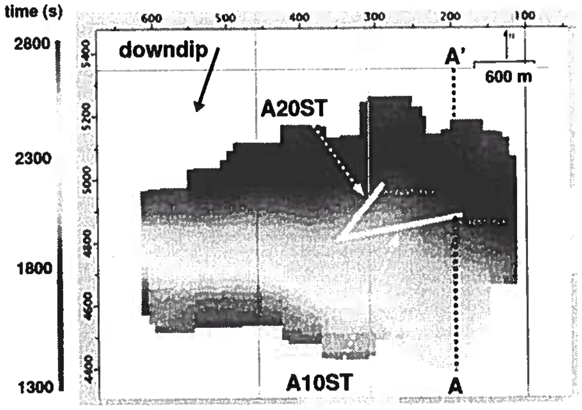

Figure 6.1. Map view of the two-way reflection time from the B-fault. The fault dips toward the southwest, as indicated by the arrow in the upper left portion of the plot. The line A-A′ is shown in the N-S direction and the paths of two wells, the A10ST and the A20ST, are shown projected onto the horizontal plane.

of the growth faults at South Eugene Island. The wells GBRN drilled into the A-fault and B-fault began in the downthrown, hydrostatically pressured sediments and passed through the faults into overpressured (upthrown) sediments. At most of the wells, the B-fault was found to be overpressured relative to the downthrown sediments, but not more overpressured than the upthrown block; the one exception was at the A10ST well. As participants in the GBRN drilling project, Losh *et al.* (1999) concluded that "except for the A10ST well, the fault itself does not generally represent a zone of low effective stress (high fluid pressure) relative to the upthrown sediments, but it is at significantly lower vertical effective stress than downthrown sediments." Furthermore, Losh *et al.* (1999) claimed that "the isolated pocket of anomalously high fluid pressure in the A10ST well may represent a spatially limited pulse of anomalously pressured fluid." Recently, Losh and Cathles (2004) identified the pulse at A10ST as an ascending fluid pulse initiated by episodic slip on the fault. With this information, we decided to apply our dip-filtering technique for studying fault-plane reflections (Haney *et al.*, 2004) to the B-fault, especially near the A10ST well.

6.4 Locally high reflectivity at the A10ST well

Our processing sequence for interpreting fault-plane reflections begins by manually picking the fault-plane of interest in a time-migrated 3D seismic data volume. In Figure 6.1, we show a time-map of the B-fault from our picks. We then dip-filter the seismic data in the direction of fault dip to accentuate the fault-plane reflections while simultaneously

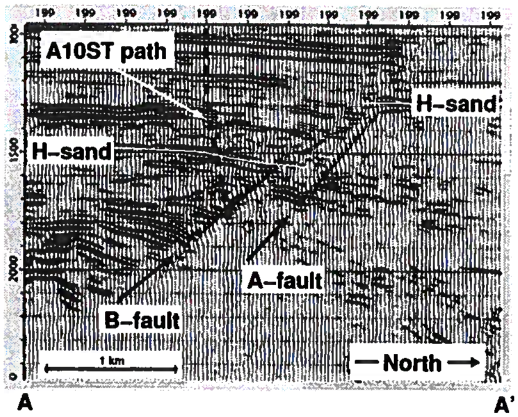

Figure 6.2. Overlay of the time-migrated seismic data (variable density) with a dip-filtered version (wiggle trace) of the same data along line A-A$'$. The dip-filtering is in the direction of fault dip to accentuate fault-plane reflections. The H-sand is highlighted to indicate the total throw across the A-fault and B-fault. The path of the A10ST well is projected into the A-A$'$ plane. The vertical axis is two-way-time in milliseconds and, taking the approximation that 1 ms two-way-time = 1 m depth, the vertical exaggeration of the plot is about 2×.

attenuating the reflections from the flat layers. The final step is to extract the maximum amplitude of the fault-plane reflection, which lies close to our picked fault-plane. We select the maximum amplitude within a time gate of 100 ms around our picked fault-plane.

In Figure 6.2, we show an overlay of the seismic data along the A-A$'$ line (see Figure 6.1) with its dip-filtered version. From this image, one can see the fault-plane reflections that occur over portions of the A-fault and the B-fault. These fault-plane reflections, as discussed in Haney *et al.* (2004), are due in part to a sharp increase in pore pressure across parts of the A-fault. The sharp increase in pore pressure results in an equally sharp decrease in seismic velocity, as shown in Chapter 1 by the velocity/pore-pressure relationship we constructed from wells at South Eugene Island. As the pore pressure increases, the differential stress (the difference between the lithostatic stress and the pore pressure) decreases. Since most of the overpressure at South Eugene Island is caused by undercompaction, the decrease in the differential stress is correlated with a decrease in seismic velocity. Losh *et al.* (1999) have documented a decrease of differential pressure by 800 psi over a distance of 18 m while drilling into the A-fault.

After extracting the maximum amplitude of the fault-plane reflection from the B-fault, we obtain the reflectivity map shown in Figure 6.3. Strong reflectivity, shown as brighter colors, come and go on the fault-plane due to the sharp lateral sealing of the B-fault. However, the strongest reflection amplitude occurs at the intersection of the A10ST

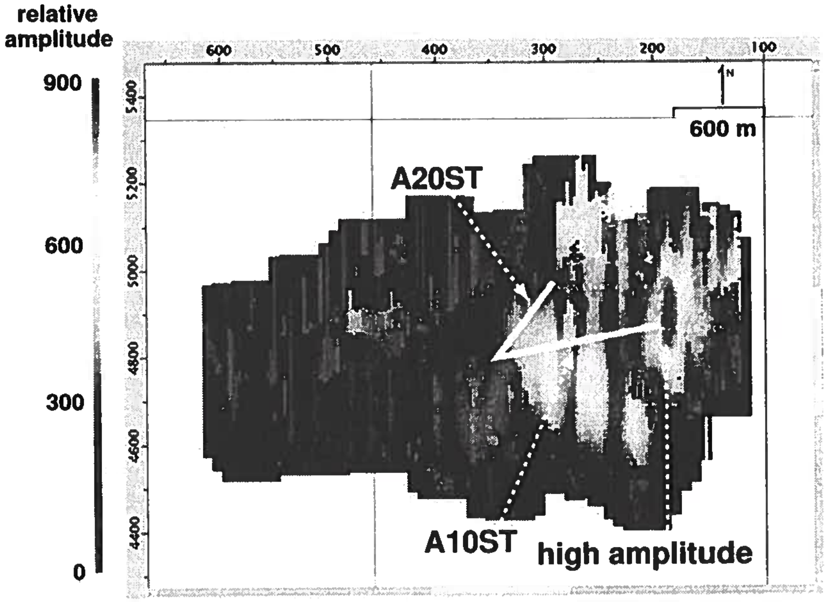

Figure 6.3. Reflection amplitude from the B-fault as a function of position on the fault-plane. The view is the same as in Fig. 1. Note the smearing of the reflection amplitudes in the up-down direction due to the dip-filter processing we employed to isolate the fault-plane reflection from the B-fault. The A20ST well, which intersected the B-fault in a "dead-zone", does not encounter an unusually high-amplitude anomaly on the fault-plane. In contrast, the A10ST well, which encountered a fluid pulse at the B-fault, terminates into the strongest reflecting portion of the fault. The reflectivity at the intersection of the A10ST well is approximately three times greater than at the A20ST well.

well with the B-fault - where a fluid pulse has been reported by Losh *et al.* (1999). At this location, we hypothesize that the fault-plane reflection arises due to a spatially-limited fluid pulse in the fault zone. We test this hypothesis in the next section by constructing synthetic seismograms with well logs from the A20ST well that cross the B-fault. Finally, we make note that, from the reflectivity map in Figure 6.3, the magnitude of the fault-plane reflection at the A10ST well is, roughly speaking, three times larger than the reflection at the A20ST well, where we have well log information.

6.5 Numerical modeling from A20ST sonic log

To better understand the variation of elastic properties that could give rise to the high reflectivity observed at the A10ST well, we generated full waveform elastic synthetic seismograms from a sonic, shear, and density log. Unfortunately, no such logs existed for the A10ST well; however, these logs were acquired through the B-fault at the nearby A20ST well. Smoothed versions of these logs are shown in Figure 6.4. Since the B-fault zone at the A10ST well was overpressured relative to the upthrown sediments and at the A20ST well it was not, we expect that, if the logs had been acquired at the A10ST well, they would have shown an anomaly on the B-fault plane. Types of anomalies at the fault-plane have been discussed already in Chapter 4 of this thesis.

We use the logs from A20ST as the physical basis for our numerical modeling. We utilize a finite-element implementation of the elastic wave equation (as discussed in Chapter 3) with a range of incident P-wave angles from 0° to 30° and a source of 20 Hz dominant frequency. We then correct the moveout for the different angles of incidence and stack the waveforms. Since the code is elastic, we are able to model conversions to S-waves. To model the anamoly at the A10ST well, we place a fracture into the B-fault zone in the logs taken from the A20ST well, where the fault was characterized as a "dead-zone" (S. Losh, 2004; personal communication). As discussed in Chapter 4, this fracture model ($\eta_N = 5 \times 10^{-10}$ m Pa^{-1} and $\eta_T = 10^{-9}$ m Pa^{-1}) can effectively be thought of as a 10 m zone with a density of 2124 kg/m^3 and a P-velocity of 2077 m/s at an effective stress of 453 psi. This model is consistent with the dimensions of the fault zone described by Losh *et al.* (1999) and the degree of additional overpressure in the fluid pulse (Losh, 2004; personal communication). Note that, at the near-normal angles of incidence used in this modelling, the reflected P-waves are hardly sensitive to the tangential compliance η_T.

The synthetic seismograms are plotted in Figure 6.5. The main waveforms are the reflections from the sedimentary layers, and the reflection from the B-fault. For both models, the seismograms are identical until the reflection from the B-fault arrives. The maximum amplitude of the fault-plane reflection from the A10ST model, which includes a fracture in the B-fault zone, is approximately three times larger than the associated fault-plane reflection from the A20ST sonic log. The model qualitatively agrees with the relative strengths of fault-plane reflections at A10ST and A20ST observed on the reflectivity map of Figure 6.3. Though the above model of a fracture in the B-fault zone qualitatively matches our observations, note that the value of the compliance scales with the thickness of the effective layer (which we assumed to be 10 m). The thickness of the layer can be thought

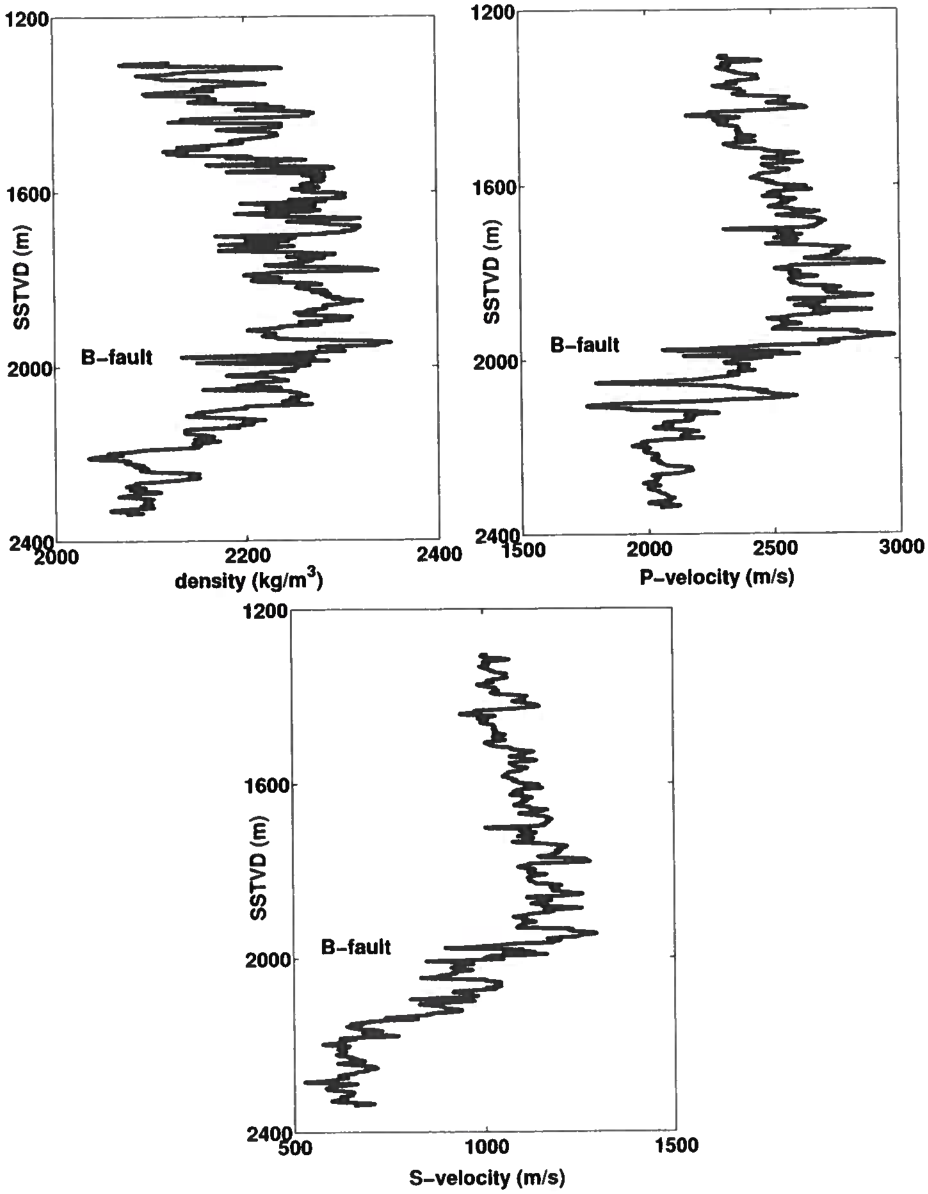

Figure 6.4. The three well logs from the A20ST well that are used for the modeling of fault reflectivity. The depth of interesection with the B-fault is displayed on each log. The shear log did not exist over the same depth range (below 2000m) as the sonic and density logs. As a result, the shear velocity is taken to be in a ratio of $V_p/V_s = 2.5$ above 2000 m and is calculated from the sonic log. These raw well logs are altered for the purpose of modeling the nearby A10ST well by placing a fracture in the B-fault zone. The fracture has a normal compliance of 5×10^{-10} m Pa^{-1} and a tangential (shear) compliance of 10^{-9} m Pa^{-1}. This fracture model can be viewed physically as a thin layer of low velocity and density, as discussed in Chapter 4.

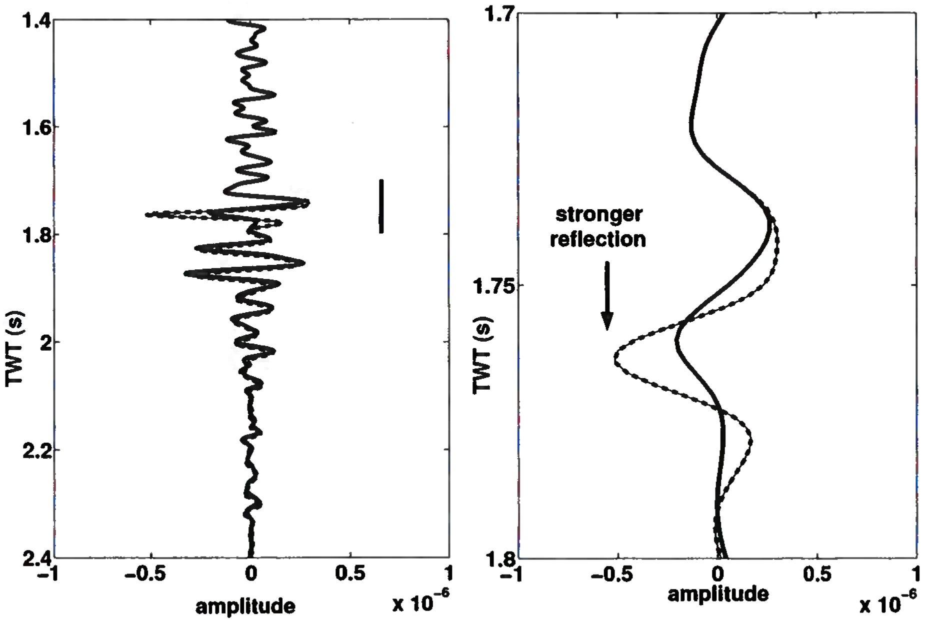

Figure 6.5. The synthetic seismograms for the A20ST (solid) and A10ST (dashed) models. On the left is a plot of the entire synthetic seismogram and on the right is a zoom of the time range shown as a vertical line on the left plot. Since the only difference in the two models is the fracture at the B-fault zone in the A10ST model, the seismograms are identical until ~ 1.74 s. At that point, the fracture in the A10ST model produces a reflection roughly three times stronger than the reflection due to only the decrease in velocity at the B-fault in the A20ST model. This factor qualitatively agrees with the relative difference in the reflectivity observed between the intersections of the A20ST and A10ST wells in Figure 6.3.

of as the fractured damage zone surrounding the main cataclastic zone, since it is this zone that effectively conducts fluids.

6.6 Conclusion on the detection of a fault burp

We have observed anomalously high reflectivity associated with a portion of a growth fault in the Gulf of Mexico where others have speculated, based on drilling records and geochemical evidence, that a fluid pulse is ascending the fault. By generating synthetic seismograms based on well logs that passed through the fault, we have demonstrated that a fracture, or effective low velocity and low density zone, at the fault-plane qualitatively agrees with the relative strength of reflected amplitudes in seismic data. The ability of reflected seismic waves to detect a fluid pulse could lead to a better understanding of hydrocarbon migration or new drilling concept that targets hydrocarbons in a fault zone. Future work will attempt to observe the fluid pulse move in different vintages of seismic data taken over a period of ten years.

6.7 Introduction to a moving pulse

In a review article, Hickman *et al.* (1995) presented nine outstanding questions in the field of "Mechanical involvement of fluids in faulting". Among these key issues, the eighth question was

> What roles do faults play in distributing fluids in the crust and in altering pressure domains? In other words, when and by what mechanisms do faults aid in or inhibit fluid migration? What are the typical fluid/rock ratios, flow rates, and discharges for fault zones acting as fluid conduits?

Despite the fact that fault-hosted fluid flow is still a poorly understood subject, several studies, both theoretical and observational, have put our understanding of the interaction of fluids and faults on firmer footing. One popular model, introduced by Rice (1992) and discussed by Revil & Cathles (2002), maintains that fluids may intermittently propagate as shock waves along faults at geologically fast rates (from m/yr to km/yr). The shock waves are excited in the subsurface when the rock permeability is a strongly nonlinear function of fluid pressure - a characteristic of highly fractured zones, such as fault zones. Nur & Walder (1992) refer to intermittent times of intense fault-hosted fluid flow as "fault burps", an endearing term that I adopt in this thesis. Such behavior is fully in line with the fault-valve model of Sibson (1990), in which fluid flow along faults is episodic and initiated by an increase in fault zone permeability in response to fault slip. Recently, Miller *et al.* (2004) show how a combination of Rice's shock wave model and Sibson's fault-valve model explains the upward movement of aftershock epicenters along a fault in the deep crust beneath Italy.

In the Gulf of Mexico, growth faults cutting through young, poorly consolidated sediments provide a means for hydrocarbons generated in deep, highly pressurized source rocks to migrate into shallow, economically producible reservoirs. This "pressure-driven" migration moves fluids at much higher rates than the conventional picture of hydrocarbon stringers slowly rising into structural high points via buoyancy. Several lines of evidence taken at the South Eugene Island Block 330 field, offshore Louisiana, point to faults allowing significant volumes of fluid to pass vertically over the last million years, even continuing to the present day. The evidence includes (a) oil seeps from the fault scarps along the ocean floor (Anderson *et al.*, 1995), (b) thermal anomalies associated with the spatial patterns of the fault scarps (Anderson *et al.*, 1991), (c) reports from drilling of anomalously high pore pressure confined to one of the fault planes (Losh *et al.*, 1999), (d) a year-to-year variation in the fluid chemistry of hydrocarbons produced from the same reservoir (Whelan *et al.*, 2001), and (e) geochemical anomalies seen in core samples taken from fault zones (Losh *et al.*, 1999). Here, I examine an additional set of data - seismic reflection images - for any indications of fast fluid movement along growth faults.

6.8 A fluid pulse caught in the act of ascending a growth fault

The South Eugene Island field is an ideal location to examine fault-plane reflections since there exists a wealth of previous studies at the field and a considerable number of wells. Most of the available information is due to a multifaceted drilling project conducted by the Global Basins Research Network (GBRN) in the 1990s (Anderson *et al.*, 1995). During late 1993, GBRN intentionally drilled into and successfully cored several of the growth faults at South Eugene Island. Included among these growth faults was a down to the southwest dipping-fault known as the B-fault. The wells GBRN drilled into the B-fault began in the downthrown, hydrostatically pressured sediments and passed through the fault into deeper, overpressured (upthrown) sediments. At most of the wells, the B-fault was found to be overpressured relative to the downthrown sediments, but not more overpressured than the upthrown block; the one exception was at the A10ST well. As participants in the GBRN drilling project, Losh *et al.* (1999) speculated that "the isolated pocket of anomalously high fluid pressure in the A10ST well may represent a spatially limited pulse of anomalously pressured fluid."

To test the hypothesis of a moving fluid pulse, we isolate the fault-plane reflections from the B-fault in surveys from 1985 and 1992 and look for indications of movement. First, we pick the fault plane in the 3D seismic reflection images (Figure 6.6A). We then proceed by dip-filtering the seismic reflection images in the direction of the B-fault (Figure 6.6B). This dip-filtering step serves to accentuate the fault-plane reflections while simultaneously attenuating the reflections from the sedimentary layers. The final step is to extract the maximum amplitude of the fault-plane reflection along the B-fault in a small time-window around the picked fault-plane. The result of this processing scheme is shown in Figure 6.6C for the 1985 data and Figure 6.6D for the 1992 data. Note the "streaking" of the reflectivities in the N-S direction due to the dip-filter operating in vertical N-S planes.

The most striking pattern in the fault reflectivity maps (Figure 6.6, C and D) is the northeast movement of the highest reflectivity areas between 1985 and 1992. This movement, in the up-dip direction, is to be expected for a fluid pulse ascending the B-fault. From the reflectivity maps, we estimate the movement of the fluid pulse to be on the order of 1 km between 1985 and 1992, for an average velocity of $\sim$ 140 m/yr. Such fast fluid

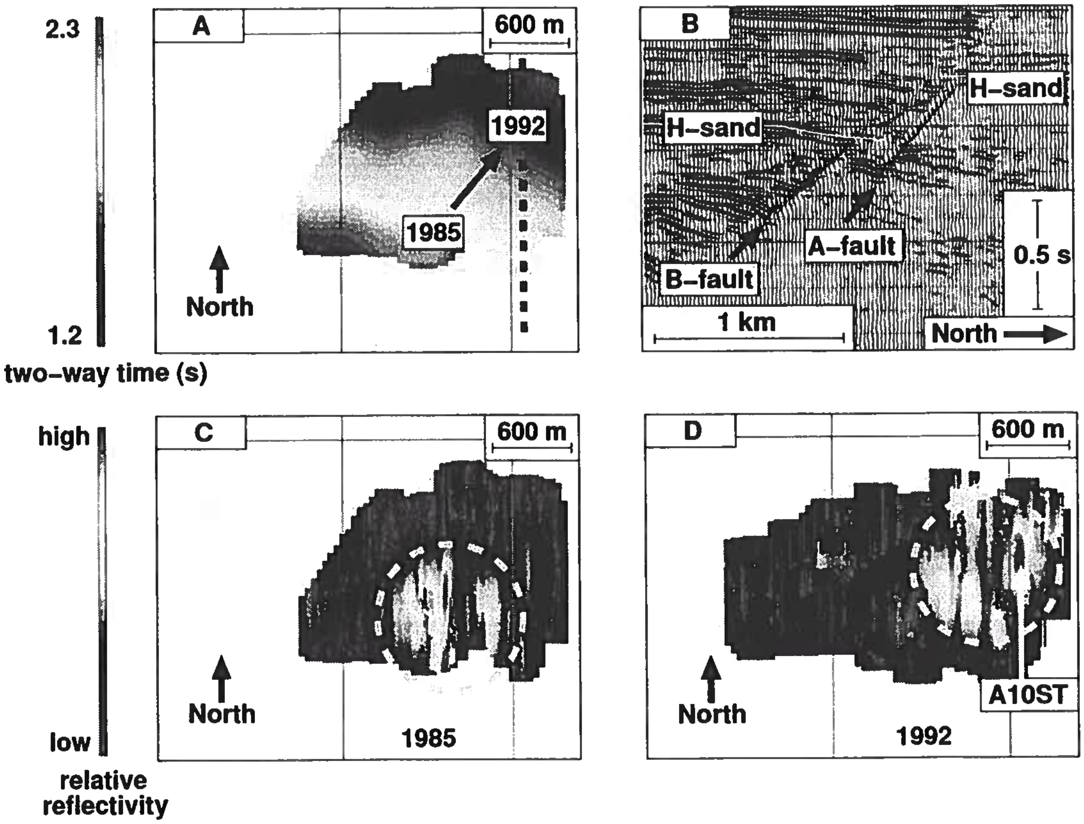

Figure 6.6. (A) Map of the two-way reflection time (TWT) to the B-fault plane. Using the approximation 100 m depth $\sim$ 0.1 s TWT (Losh *et al.*, 1999), this map shows the structure of the B-fault, most notably the down-to-the-SW dip. (B) Overlay of the dip-filtered seismic reflection image (black & white) on top of the original image (red & blue) along the dashed line in (A). The dip-filtering highlights the fault-plane reflections from the B-fault and a nearby fault known as the A-fault. The H-sand is shown to indicate throw. (C) Map of the B-fault, as in (A), but with reflectivity from the fault-plane in 1985 plotted instead of TWT. The area of highest reflectivity is circled in gold. (D) Map of the B-fault reflectivity, as in (C), but from 1992. Note that the data extends over a slightly larger area than in (C); however, the spatial perspective is identical. The area of highest reflectivity is circled in gold; it is shifted roughly 1 km NE in the up dip direction relative to the 1985 data in (C). This movement is depicted by the arrow in (A). Also shown is the location of the A10ST well intersection, where high fluid pressures were encountered while drilling into the B-fault zone in 1993 (Losh *et al.*, 1999).

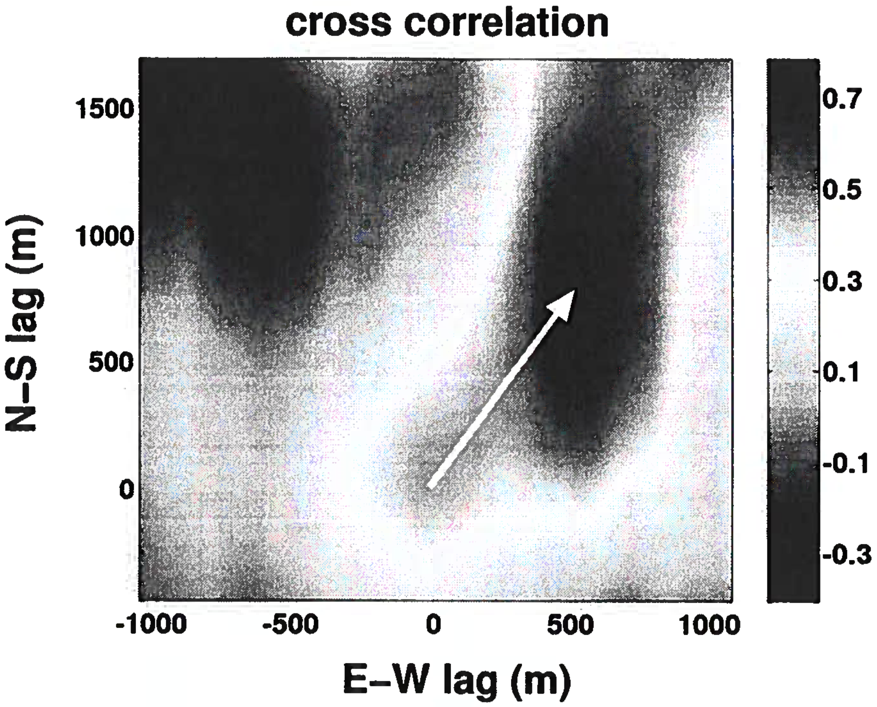

Figure 6.7. Spatial cross correlation of the 1985 and 1992 B-fault amplitude maps shown in Figure 6.6. There is a maximum in the cross correlation when the spatial lag is 1 km to the NE (the up-dip direction of the A-fault). At the maximum, the correlation coefficient is 0.78, which is close to the value 0.80 for a horizontal reflector known as the O-sand at zero spatial lag. The correlation can be seen visually in subplots (C) and (D) of Figure 6.6.

flow up a vertically permeable fault is in line with a nonlinear permeability model first discussed by Rice (1992) and has relavence for the understanding of hydrocarbon migration mechanisms.

In Figure 6.7, I plot the spatial cross correlation of the amplitude maps from the B-fault. There is a local maximum at 1 km spatial lag in the NE direction. This corresponds to what is seen visually in Figure 6.6 C and D. The value of the correlation at the maximum is 0.78, which is close to the value 0.80 computed for a horizontal reflector known as the O-sand at zero-lag (see Figure 6.6). The zero-lag correlation for the B-fault amplitude maps is 0.45. The fact that the correlation is as high as 0.80 for the O-sand in its zero-lag position supports the similarity of the two surveys and their processing schemes. In Chapter 4, I included noise, no DMO, and AGC as some possible problematic processing scenarios to see which of these most degraded the amplitudes. The AGC was the worst by far in changing the relative amplitudes. Though an AGC appears to have been applied to the 1985 data, it obviously did not damage the amplitudes from the O-sand enough to bring its correlation below 0.8. I have also checked the K-sand and found good amplitude agreement in its

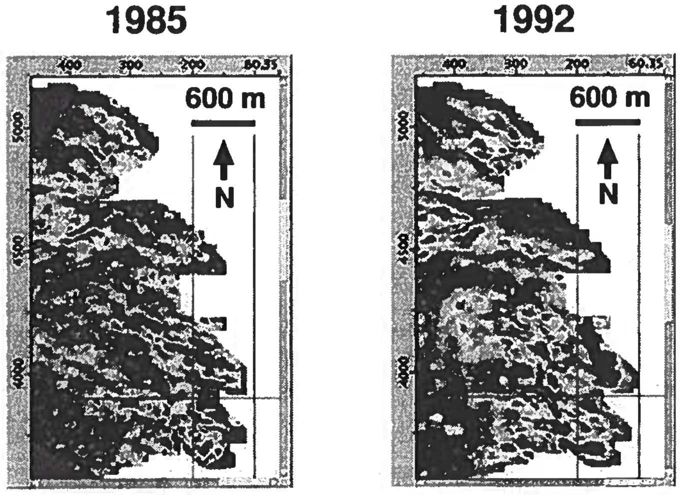

Figure 6.8. A comparison of the O-sand amplitude in the 1985 and 1992 surveys. The consistency of the amplitudes in these two images supports the interpretation of the fault-plane reflections. The correlation coefficent of the two images is 0.80

zero-lag poisiton. Both the O- and K-sands are in the same depth interval as the B-fault plane.

In the final figure, I plot the amplitude along the Z-fault in a data set from 1988 and the Shell data set from 1992. The Z-fault is antithetic to both the B- and A-faults; it is the opposite minibasin-bounding fault from the A-fault (see Figure 1.2). The 1988 data was shot by Texaco over the southern portion of South Eugene Island Block 330. Unfortunately, the 1988 survey did not cover the B-fault or I would have plotted the B-fault amplitude as well. The reflectivity from the Z-fault shown in Figure 6.9 does not appear to move during the time between 1988 and 1992. Hence, the fault-plane reflection could be due to a pore pressure contrast across the fault that is stationary, as the ones I described in Chapter 5. The fact that there is not a lot of change between the 1988 and 1992 data sets at the Z-fault disputes the argument that, due to different processing in 1988 and 1992, the fault-plane reflections should be completely different. The amplitude image in Figure 6.9 for the 1988 data is considerably more noisy, but still similar to the amplitude along the Z-fault in the 1992 data.

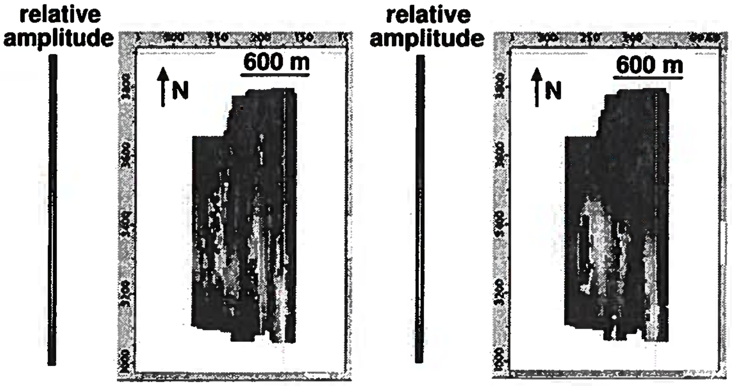

Figure 6.9. A comparison of the Z-fault reflectivity in the 1988 and 1992 surveys. Compared to the changes seen at the B-fault between the 1985 and 1992 surveys, this reflectivity pattern does not appear to change. This may be due to the fault-plane reflections from the Z-fault arising due to a pressure contrast across the fault that is stationary with time.

Chapter 7

Conclusions

The faults at South Eugene Island, Block 330 truly cannot make up their mind. In some areas, they provide a significant seal and hold back tens of meters of hydrocarbon columns. And yet, large volumes of fluid, both hydrocarbon and brine, have seemingly managed to pass upwards through shale-dominated sedimentary layers by moving along the fault plane. I find evidence in seismic data acquired at South Eugene Island to support the existence of both types of fault behavior. Over large parts of the A-fault, elevated reflectivity occurs along the depth range of the fault known to have the highest pressure difference across it (Losh *et al.*, 1999). At a location on the nearby B-fault, where anomalously high pore pressures have been reported in the fault zone (Anderson *et al.*, 1995), areas of high reflectivity appear to move up the fault-plane, as would be expected for an ascending, pressure-driven fluid pulse. The seismic waves are able to sense these different pressure domains due to the effective stress controlling the elastic properties of the soft Plio-Pleistocene sediments. I have performed extensive numerical modeling while utilizing effective stress relationships for velocity and density in an effort to substantiate the dip-filtering technique for interpreting fault-plane reflections. A main outcome of this thesis is the demonstration that fault-plane reflections constitute another source of useful information for geologists and basin modellers to take into account when forming their picture of the petroleum system. Another primary outcome is the first observation based on seismic reflection images of a fluid pulse ascending a growth fault. This observation gives additional credence to the "dynamic fluid injection" (Whelan *et al.*, 2001) hypothesis and points to natural processes in sedimentary basins that occur on production time scales.

One question is whether the speed of the fluid pulse I obtain from the seismic images, $\sim$140 m/yr makes any sense from the point of view of fluid dynamics. It turns out that, when the permeability of the fault zone rock is highly dependent on pore pressure, solitary wave solutions exist to the fluid flow equations that propagate along faults (Rice, 1992; Revil & Cathles, 2002). Moreover, flow tests conducted in fault zones have shown that, due to intense fracturing, the permeability of the fault rock can vary by orders of magnitudes in going from hydrostatic to nearly lithostatic pore pressures (Fisher *et al.*, 1996; Anderson *et al.*, 1995). The physical picture for this phenomenon is that the fluid flow is mostly in an interconnected fracture network (Domenico & Schwartz, 1990). As the pore pressure rises, the fractures open up, thereby allowing more flow (higher permeability). Hence, the permeability depends on the fluid pressure. As the originator of this model, Rice (1992) quoted a nominal pulse speed of 60 m/yr, within an order of magnitude of the estimate I get from the movement of the fault-plane reflections. Losh & Cathles (2004) modelled the fault-hosted fluid flow at South Eugene Island and obtained a flow rate of 43 m/yr. In perhaps an attempt to grab attention, Revil & Cathles (2002) claimed that the fluid pulses could move at up to 160 km/yr! In any case, though the speed observed in the time-lapse seismic images is geologically fast, it is conducive with previous estimates of flow along faults.

The nonlinear permeability model may make it possible to have solitary fluid waves propagating up a fault, but how does a fault actually initiate one of these "fault burps"? If slip along a fault increases the along-fault permeability, then the breaching of an overpressured compartment, such as those known to exist in the deeper sediments (beneath the O-sand) of South Eugene Island, can result in "fault-valve" behavior (Sibson, 1990). During this time, the fault acts as a pipe connecting shallow, hydrostatic sediments to deeper overpressured ones. It is unclear how the issue of seismic versus aseismic slip impacts the ability of a fault to exhibit valving.

The fact that the fluid pulse I observe at South Eugene Island appears to be limited in its spatial extent begs another question - why and how does the fault reseal in the wake of the fluid pulse? Does the reservoir it is tapping drain all of its fluids, or does the fault reseal due to porosity reduction? To my knowledge, the research done on fluid pulses racing up faults focuses almost entirely on the initiation of the fluid pulse (Miller *et al.*, 2004).

Could the vertical permeability at the B-fault be forming in response to the interaction of the B-fault and the large, minibasin-bounding A-fault instead of repeated shear along the fault-plane? Close proximity of faults can create relay zones between them (Rowan *et al.*, 1998). These relay zones, as a result of their local stress field, are typically highly fractured. The B-fault and A-fault, being within tens to hundreds of meters from each other, are most likely interacting with each other's stress fields and deforming the rock mass between them.

An additional goal of my research into the properties of faults is to identify advantageous, but rare, methodologies for investigating fault zones. One such technique I would like to highlight for future investigation is the measurement of seismic waves within a fault zone. If the fault is a relatively weak layer compared to the host rock, as is the case for a pressurized fault, "fault-zone guided waves" should be observed. These dispersive waves have proven to be a useful tool for characterizing the interior structure of tectonic faults in earthquake seismology (Li *et al.*, 1990; Li & Leary, 1990; Igel *et al.*, 1997). Since most of the energy of these guided waves resides at the fault plane, these waves are extremely sensitive to the elastic properties of the fault. Perhaps, if observed in time-lapse mode, the guided waves could give an indication of any fluid movement along the fault.

Two wells drilled by the Global Basins Research Network, the A20ST and A6ST, intersect the A-fault hundreds of meters from each other. As an example of a possible guided wave experiment at South Eugene Island, a crosswell seismic survey, between the A20ST and A6ST wells, could generate dispersive waves along the fault if the source is located in or near the fault zone itself. Whether the dispersive waves turn out to be guided or leaky would depend on the elastic properties of the A-fault zone relative to the upthrown and downthrown sediments. Since the upthrown (overpressured) sediments have a lower velocity than the downthrown (hydrostatic) sediments, it may well be that the dispersive waves along the A-fault leak into the upthrown sediments but are guided by the downthrown sediments.

Both wells have been cased (Losh, 2003; personal communication) which increases the coupling between the source and the formation for a crosswell experiment. Other data sets to incorporate into future fault studies are prestack data, especially for doing AVO analysis on a fault-plane reflection, and microseismicity data. Based on the initial comparisons of the 1985 and 1992 data sets in this thesis, future studies on faults should incorporate time-lapse measurements to capture the essence of faults as dynamic and quickly-changing zones.

References

Adams, N., & Kuhlman, L. 1994. *Kicks and Blowout Control.* Tulsa: PennWell Books.

Aki, K., & Richards, P. 1980. *Quantitative Seismology.* San Francisco: W. H. Freeman and Company.

Alterman, Z. S., & Loewenthal, D. 1970. Seismic Waves in a Quarter and Three-Quarter Plane. *Geophys. J. R. astr. Soc.*, **20**, 101.

Ampuero, J. P. 2002. *Etude physique et numérique de la nucléation des séismes.* PhD Thesis, Université Paris 7, Paris, France.

Anderson, R. N., He, W., Hobart, M. A., Wilkinson, C. R., & Roice, H. R. 1991. Active fluid flow in the Eugene Island area, offshore Louisiana. *The Leading Edge*, **10**, 12–17.

Anderson, R. N., Billeaud, L. B., Flemings, P. B., Losh, S., & Whelan, J. K. 1995. *Results of the Pathfinder Drilling Program into a Major Growth Fault, Part of the GBRN/DOE Dynamic Enhanced Recovery Project in Eugene Island 330 Field, Gulf of Mexico.* Lamont-Doherty Earth Observatory: Global Basins Research Network.

Athy, L. F. 1930. Density, porosity, and compaction of sedimentary rocks. *AAPG Bulletin*, **14**, 1–22.

Black, J. L., Schleicher, K. L., & Zhang, J. 1993. True-amplitude imaging and dip moveout. *Geophysics*, **58**, 47–66.

Bleistein, N., Cohen, J. K., & Jr., J. W. Stockwell. 2001. *Mathematics of multidimensional seismic imaging, migration and inversion.* New York: Springer-Verlag.

Boore, D. M. 1970. *Finite-difference solutions to the equations of elastic wave propagation, with applications to Love waves over dipping interfaces.* PhD Thesis, MIT.

Born, M., & Wolf, E. 1980. *Principles of Optics.* Cambridge: Cambridge University Press.

Bowers, G. L. 1995. Pore Pressure Estimation from Velocity Data: Accounting for Overpressure Mechanisms Besides Undercompaction. *SPE Drilling & Completion*, **June**, 89–95.

Carcione, J. M., & Tinivella, U. 2001. The seismic response to overpressure: a modeling study based on laboratory, well, and seismic data. *Geophysical Prospecting*, **49**, 523.

Chaisri, S., & Krebes, E. S. 2000. Exact and approximate formulas for *P-SV* reflection and transmission coefficients for a nonwelded contact interface. *JGR*, **105**, 28045.

Chew, W. C., & Liu, Q. H. 1996. Perfectly matched layers for elastodynamics: a new absorbing boundary condition. *Journal of Computational Acoustics*, **4**, 341–359.

Clayton, R., & Enquist, B. 1977. Absorbing boundary conditions for acoustic and elastic wave equations. *Bulletin of the Seismological Society of America*, **67**, 1529–1540.

Coates, R. T., & Schoenberg, M. 1995. Finite-difference modeling of faults and fractures. *Geophysics*, **60**, 1514.

Demirbag, E., Çoruh, C., & Costain, J. K. 1993. Inversion of P-Wave AVO. *Pages 500–540 of:* Castagna, J. P., & Backus, M. M. (eds), *Offset-dependent reflectivity - theory and practice of AVO analysis.* Tulsa: SEG.

Domenico, P. A., & Schwartz, F. W. 1990. *Physical and Chemical Hydrogeology.* New York: Wiley.

Dunkin, J. W., & Levin, F. K. 1973. Effect of Normal Moveout on a Seismic Pulse. *Geophysics*, **38**, 635–642.

Dutta, N. C. 1997. Pressure prediction from seismic data: implications for seal distribution and hydrocarbon exploration and exploitation in the deepwater Gulf of Mexico. *Pages 187–199 of:* Moeller-Pederson, P., & Koestler, A. G. (eds), *Hydrocarbon Seals: Importance for Exploration and Production.* Singapore: Elsevier.

Elliott, D. A. 1999. *Hydrofracture Permeability Response and Maximum Previous Consolidation Stress Estimations for Faulted and Micro-Faulted Silty-Shales Taken from the Eugene Island Block 330 Field Pathfinder Well in the Gulf of Mexico.* MSc Thesis, University of California, San Diego.

Fisher, A. T., Zwart, G., & Party, Ocean Drilling Program Leg 156 Scientific. 1996. Relation between permeability and effective stress along a plate-boundary fault, Barbados accretionary complex. *Geology*, **24**, 307–310.

Gausland, I. 2004. The stacking response: what happened to offset? *First Break*, **22**, 43–46.

Groenenboom, J. 1998. *Acoustic Monitoring of Hydraulic Fracture Growth.* PhD Thesis, Delft University.

Hale, D. 1991. *Dip Moveout Processing.* Course Notes Series, vol. 4. Tulsa: Society of Exploration Geophysicists.

Haltiner, G. J., & Williams, R. T. 1980. *Numerical Prediction and Dynamic Meteorology.* New York: Wiley.

Haney, M., & Li, Y. 2002. Total magnetization direction and dip from multiscale edges. *Pages 735–738 of: 72^{nd} Ann. Internat. Mtg., Society of Exploration Geophysicists, Expanded Abstracts.* to be submitted to Geophysics.

Haney, M., , & Snieder, R. 2003a. Breakdown of Diffusion in 2D due to Loops. *Phys. Rev. Lett.*, **91**, 093903.

Haney, M., Li, Y., & Nabighian, M. N. 2003b. Envelopes of 2D and 3D magnetic data and their relationship to the analytic signal: Preliminary results. *Pages 592–595 of: 73^{rd} Ann. Internat. Mtg., Society of Exploration Geophysicists, Expanded Abstracts.* to be submitted to Geophysics.

Haney, M., Sheiman, J., Snieder, R., Naruk, S., Busch, J., & Wilkins, S. 2004. Fault-plane reflections as a diagnostic of pressure differences in reservoirs: a case study from South Eugene Island Block 330. *Pages O–07 of:* Engelder, T., Konstanty, J., & Grauls, D. (eds), *Proceedings of the EAGE special session on Fault and Top Seals.* EAGE.

Haney, M., Van Wijk, K., & Snieder, R. 2005. Radiative transfer in layered media and its connection to the O'Doherty-Anstey formula. *to be published in the January-February Geophysics.*

Hart, B. S., Flemings, P. B., & Deshpande, A. 1995. Porosity and pressure: Role of compaction disequilibrium in the development of geopressures in a Gulf Coast Pleistocene basin. *Geology*, **23**, 45–48.

Hatchell, P. J. 2000. Fault whispers: Transmission distortions on prestack seismic reflection data. *Geophysics*, **65**, 377.

Hatton, L., Worthington, M. H., & J., Makin. 1986. *Seismic Data Processing: Theory and Practice.* Oxford: Blackwell Science.

Hickman, S., Sibson, R., & Bruhn, R. 1995. Introduction to special section: Mechanical involvement of fluids in faulting. *JGR*, **100**, 12831–12840.

Huffman, A. R. 2002. The Future of Pressure Prediction Using Geophysical Methods. *Pages 217–233 of:* Huffman, Alan, & Bowers, Glenn (eds), *Pressure regimes in sedimentary basins and their prediction.* AAPG Memoir, no. 76. Tulsa: AAPG.

Igel, H., Ben-Zion, Y., & Leary, P. C. 1997. Simulation of SH- and P-SV-wave propagation in fault zones. *Geophys. J. Int.*, **128**, 533.

Jordan, J. R., & Shirley, O. J. 1966. Application of Drilling Performance Data to Overpressure Detection. *Journal of Petroleum Technology*, **18**, 1387.

Karniadakis, G. E., & Sherwin, S. J. 1999. *Spectral/HP Element Methods for CFD.* Oxford: Oxford University Press.

Kelly, K. R., & Marfurt, K. J. (eds). 1990. *Numerical Modeling of Seismic Wave Propagation.* Geophysics reprint series No. 13. SEG.

Kelly, K. R., Ward, R. W., Treitel, S., & Alford, R. M. 1976. Synthetic seismograms: A finite-difference approach. *Geophysics*, **41**, 2.

Komatitsch, D., & Tromp, J. 2003. Introduction to the spectral-element method for three-dimensional seismic wave propagation. *Geophys. J. Int.*, **139**, 806.

Komatitsch, D., & Vilotte, J. P. 1998. The spectral element method: An efficient tool to simulate the seismic response of 2D and 3D geological structures. *BSSA*, **88**, 368–392.

Komatitsch, D., Barnes, C., & Tromp, J. 2000. Wave propagation near a fluid-solid interface: A spectral-element approach. *Geophysics*, **65**, 623–631.

Li, Y., Shearer, S., Haney, M., & Dannemiller, N. 2004. Comprehensive approaches to the inversion of magnetic data with strong remanent magnetization. *Pages 638–641 of: 74th Ann. Internat. Mtg., Society of Exploration Geophysicists, Expanded Abstracts.*

Li, Y.-G., & Leary, P. 1990. Fault Zone Trapped Seismic Waves. *BSSA*, **80**, 1245.

Li, Y.-G., Leary, P., Aki, K., & Mahlin, P. 1990. Seismic Trapped Modes in the Oroville and San Andreas Fault Zones. *Science*, **249**, 763.

Liner, C. L. 1999. *Elements of 3-D Seismology.* Tulsa: PennWell.

Losh, S., & Cathles, III, L. 2004. Fault Conduit/Fault Seal Behavior, South Eugene Island Block 330 Field, Offshore Louisiana. *Pages P-43 of:* Engelder, T., Konstanty, J., & Grauls, D. (eds), *Proceedings of the EAGE special session on Fault and Top Seals.* Houten: EAGE.

Losh, S., Eglinton, L., Schoell, M., & Wood, J. 1999. Vertical and Lateral Fluid Flow Related to a Large Growth Fault. *AAPG Bulletin*, **83**, 244–276.

Losh, S., Walter, L., Meulbroek, P., Martini, A., Cathles, L., & Whelan, J. 2002. Reservoir fluids and their migration into the South Eugene Island Block 330 reservoirs, offshore Louisiana. *AAPG Bulletin*, **86**, 1463–1488.

Lu, J. 1993. *The principles of seismic exploration.* Beijing: Press of the Petroleum University, in Chinese.

Marfurt, K. J. 1984. Accuracy of finite-difference and finite-element modeling of the scalar and elastic wave equations. *Geophysics*, **49**, 533.

Miller, S. A., Collettini, C., Chiaraluce, L., Cocco, M., Barchi, M., & Kaus, B. J. P. 2004. Aftershocks driven by a high-pressure CO_2 source at depth. *Nature*, **427**, 724–727.

Needham, T., & Yielding, G. 1996. Fault population description and prediction using examples from the offshore U.K. *Journal of Structural Geology*, **18**, 155–167.

Nur, A., & Walder, J. 1992. Hydraulic Pulses in the Earth's Crust. *Pages 461–474 of:* Evans, B., & Wong, T.-F. (eds), *Fault Mechanics and Transport Properties of Rocks.* San Diego: Academic Press.

Oppenheim, A. V., & Schafer, R. W. 1975. *Digital Signal Processing.* Englewood Cliffs, New Jersey: Prentice-Hall.

Pennebaker, E. S. 1968. Seismic data indicate depth, magnitude of abnormal presures. *World Oil*, **166**, 73.

Press, W. H., Flannery, B. P., Teukolsky, S. A., & Vetterling, W. T. 1992. *Numerical Recipes in C: the Art of Scientific Computing.* Cambridge: Cambridge University Press.

Pyrak-Nolte, L. 1996. The seismic response of fractures and the interrelations among fracture properties. *Int. Journ. of Rock Mechanics and Mining Sci. and Geomech. Abstr.*, **8**, 785.

Pyrak-Nolte, L., Myer, L., & Cook, N. 1990. Transmission of Seismic Waves Across Single Natural Fractures. *JGR*, **95**, 8617.

Revil, A., & Cathles, L. M. 2002. Fluid transport by solitary waves along growing faults: A field example from the South Eugene Island Basin, Gulf of Mexico. *Earth and Planetary Science Letters*, **202**, 321–335.

Rice, J. R. 1992. Fault Stress States, Pore Pressure Distributions, and the Weakness of the San Andreas Fault. *Pages 475–503 of:* Evans, B., & Wong, T.-F. (eds), *Fault Mechanics and Transport Properties of Rocks.* San Diego: Academic Press.

Rowan, M. G., Hart, B. S., Nelson, S., Flemings, P. B., & Trudgill, B. D. 1998. Three-dimensional geometry and evolution of a salt-related growth-fault array: Eugene Island 330 field, offshore Louisiana, Gulf of Mexico. *Marine and Petroleum Geology*, **15**, 309–328.

Schoenberg, M. 1980. Elastic wave behavior across linear slip interfaces. *J. Acoust. Soc. Am.*, **68**, 1516–1521.

Scholz, C. H., & Anders, M. H. 1994. The permeability of faults. *Pages 247–253 of:* Hickman, S., Sibson, R., & Bruhn, R. (eds), *The Mechanical Involvement of Fluids in Faulting.* USGS Workshop LXIII. USGS.

Seriani, G., & Priolo, E. 1994. Spectral element method for acoustic wave simulation in hetrogeneous media. *Finite Elements in Analysis and Design*, **16**, 337–348.

Sheriff, R. E. 1984. *Encyclopedic Dictionary of Exploration Geophysics.* Tulsa: SEG.

Shuey, R. T. 1985. A simplification of the Zoeppritz equations. *Geophysics*, **50**, 609.

Sibson, R. H. 1990. Conditions for fault-valve behavior. *Pages 15–28 of:* Knipe, R. J., & Rutter, E. H. (eds), *Deformation Mechanisms, Rheology and Tectonics.* Geological Society Special Publication, no. 54. Oxford: Alden Press.

Stockwell, Jr., J. W. 1997. Free software in education; a case study of CWP7SU: Seismic Unix. *The Leading Edge*, **16**, 1045–1049.

Stump, B., Flemings, P., Finkbeiner, T., & Zoback, M. 1998. Pressure differences between overpressured and bounding shales of the Eugene Island 330 field (offshore Louisiana, USA) with implications for fluid flow induced by sediment loading. *in: Overpressures in petroleum exploration: workshop proceedings, eds. A. Mitchell and D. Grauls, Elf Exploration Production Memoir 22.*

Stump, B. B., & Flemings, P. B. 2002. Consolidation State, Permeability, and Stress Ratio as Determined from Uniaxial Strain Experiments on Mudstone Samples from the Eugene Island 330 Area, Offshore Louisiana. *Pages 131–144 of:* Huffman, Alan, & Bowers, Glenn (eds), *Pressure regimes in sedimentary basins and their prediction.* AAPG Memoir, no. 76. Tulsa: AAPG.

Terzaghi, K. 1943. *Theoretical Soil Mechanics.* New York: Wiley.

Thomsen, L. 1993. Weak anisotropic reflections. *Pages 200–240 of:* Castagna, J. P., & Backus, M. M. (eds), *Offset-dependent reflectivity - theory and practice of AVO analysis.* Tulsa: SEG.

Toldi, J. L. 1985. *Velocity analysis without picking.* PhD Thesis, Stanford University.

Townsend, C., Firth, I. R., Westerman, R., Kirkevollen, L., Harde, M., & Anderson, T. 1998. Small seismic-scale fault identification and mapping. *in: Faulting, Fault Sealing and Fluid Flow in Hydrocarbon Resrvoirs, eds. G. Jones, Q. J. Fisher, and R. J. Knipe, Geological Society Special Publication No. 147.*

Van Wijk, K., Haney, M., & Scales, J. 2004. 1D energy transport in a strongly scattering laboratory model. *Phys. Rev. E*, **69**, 036611.

Wang, H. F. 2000a. *Theory of Linear Poroelasticity.* Princeton: Princeton University Press.

Wang, J. 2000b. *Finite Element Methods: Theory and Implementation.* Course Notes, Colorado School of Mines.

Wang, Y. 1999. Approximations to the Zoeppritz equations and their use in AVO analysis. *Geophysics*, **64**, 1920–1932.

Whelan, J. K., Eglinton, L., Kennicutt, II, M. C., & Qian, Y. 2001. Short-time-scale (year) variations of petroleum fluids from the U. S. Gulf Coast. *Geochim. Cosmochim. Acta*, **65**, 3529–3555.

Widess, M. B. 1973. How Thin is a Thin Bed? *Geophysics*, **38**, 1176.

Worthington, M. H., & Hudson, J. A. 2000. Fault properties from seismic *Q*. *Geophys. J. Int.*, **143**, 937.

Yielding, G., Badley, M. E., & Freeman, B. 1991. Seismic reflections from normal faults in the northern North Sea. *in: The Geometry of Normal Faults, eds. A. M. Roberts, G. Yielding, and B. Freeman, Geological Society Special Publication No. 56.*

Yilmaz, Ö. 1987. *Seismic Data Processing.* Tulsa: Society of Exploration Geophysicists.

Zhang, S., & Tullis, T. E. 1998. The effect of fault slip on permeability and permeability anisotropy in quartz gouge. *Tectonophysics*, **295**, 41.

Zienkiewicz, O. C., & Taylor, R. L. 2000. *The Finite Element Method.* Vol. 1. Oxford: Butterworth-Heinemann.

Zimmer, M., Prasad, M., & Mavko, G. 2002. Pressure and porosity influences on $V_P - V_S$ ratio in unconsolidated sands. *The Leading Edge*, **21**, 178.

Appendix A

Derivatives needed for the DMO filter

There are two fundamental equations to consider in the derivation of the DMO filter. The first is the DMO trajectory, previously given by equation (2.36) as

$$t_{dmo}(x) = \frac{t_{out}}{\sqrt{1 - (x - x_{out})^2/h^2}},$$

where t_{out} is the time output from DMO, x_{out} is the output midpoint, and h is the half-offset. The expression for $t_{dmo}(x)$ is given as a function of midpoint. The other relationship is the equation of a dipping reflector after NMO-correction, previously given by equation (2.42) as

$$t_{refn}(x) = \sqrt{\left(p(x - x_{in}) + \sqrt{t_{in}^2 + p^2h^2 + 4h^2\left[\frac{1}{v_{st}^2} - \frac{1}{v^2}\right]}\right)^2 - p^2h^2 - 4h^2\left[\frac{1}{v_{st}^2} - \frac{1}{v^2}\right]},$$

where v is the true velocity, v_{st} is the stacking velocity, p is the time dip, and t_{in} is the time input to DMO. As with $t_{dmo}(x)$, the expression for $t_{refn}(x)$ is given as a function of midpoint.

The organization of this appendix is as follows: we first derive the second derivatives of $t_{refn}(x)$ and $t_{dmo}(x)$ since these are needed in the stationary phase approximation for the DMO filter, equation (2.48). We evaluate the second derivatives at the input point $x = x_{in}$, as required by equation (2.48). From this analysis, we derive equations (2.53), (2.54), and (2.52). We then return to some relationships involving the first derivatives of $t_{refn}(x)$ and $t_{dmo}(x)$. By examining these relationships, we derive equations (2.45), (2.44), (2.47), and (2.51).

For the DMO trajectory, $t_{dmo}(x)$, the first derivative with respect to x is

$$\frac{\partial t_{dmo}(x)}{\partial x} = \frac{t_{out}\ (x - x_{out})}{h^2\ [1 - (x - x_{out})^2/h^2]^{3/2}}. \tag{A.1}$$

The second derivative is obtained via the product rule of differentiation

$$\frac{\partial^2 t_{dmo}(x)}{\partial x^2} = 3\frac{t_{out}(x - x_{out})^2}{h^4}\left[1 - \frac{(x - x_{out})^2}{h^2}\right]^{-5/2} + \frac{t_{out}}{h^2}\left[1 - \frac{(x - x_{out})^2}{h^2}\right]^{-3/2}. \tag{A.2}$$

By pulling out a common factor in equation (A.2), we get

$$\frac{\partial^2 t_{dmo}(x)}{\partial x^2} = \left[1 - \frac{(x - x_{out})^2}{h^2}\right]^{-5/2} \frac{t_{out}}{h^2} \left(2\frac{(x - x_{out})^2}{h^2} + 1\right). \tag{A.3}$$

Evaluating equation (A.3) at $x = x_{in}$ yields equation (2.53). To obtain equation (2.54), we rewrite equation (A.3) as

$$\frac{\partial^2 t_{dmo}(x)}{\partial x^2} = \left[1 - \frac{(x - x_{out})^2}{h^2}\right]^{-5/2} \frac{t_{out}}{h^2} \left(3\frac{(x - x_{out})^2}{h^2} + \left[1 - \frac{(x - x_{out})^2}{h^2}\right]\right). \tag{A.4}$$

Evaluating equation (A.4) at $x = x_{in}$ gives

$$\frac{\partial^2 t_{dmo}(x)}{\partial x^2}|_{x=x_{in}} =$$

$$\left[1 - \frac{(x_{in} - x_{out})^2}{h^2}\right]^{-5/2} \frac{t_{out}}{h^2} \left(3\frac{(x_{in} - x_{out})^2}{h^2} + \left[1 - \frac{(x_{in} - x_{out})^2}{h^2}\right]\right). \tag{A.5}$$

The DMO ellipse, equation (2.43), can be rearranged as

$$\frac{(x_{in} - x_{out})^2}{h^2} = 1 - \frac{t_{out}^2}{t_{in}^2}.$$

Substituting this expression into equation (A.5) results in

$$\frac{\partial^2 t_{dmo}(x)}{\partial x^2}|_{x=x_{in}} = \left(\frac{t_{in}}{t_{out}}\right)^5 \frac{t_{out}}{h^2} \left(3\left[1 - \left(\frac{t_{out}}{t_{in}}\right)^2\right] + \left(\frac{t_{out}}{t_{in}}\right)^2\right). \tag{A.6}$$

By combining common terms and doing some rearranging, equation (A.6) can be written as

$$\frac{\partial^2 t_{dmo}(x)}{\partial x^2}|_{x=x_{in}} = \left(\frac{t_{in}}{t_{out}}\right)^4 \frac{t_{in}}{h^2} \left(3 - 2\left(\frac{t_{out}}{t_{in}}\right)^2\right). \tag{A.7}$$

Finally, by pulling out $(t_{out}/t_{in})^2$ from the last term on the right-hand side of equation (A.7), we get equation (2.54):

$$\frac{\partial^2 t_{dmo}(x)}{\partial x^2}|_{x=x_{in}} = \left(\frac{t_{in}}{t_{out}}\right)^2 \frac{t_{in}}{h^2} \left(3\left(\frac{t_{in}}{t_{out}}\right)^2 - 2\right).$$

The same analysis as outlined above needs to be performed on the equation of a dipping reflector after NMO-correction, $t_{refn}(x)$. Using the expression for $t_{refn}(x)$ given at the beginning of this appendix, the derivative of $t_{refn}(x)$ with respect to x is

$$\frac{\partial t_{refn}(x)}{\partial x} = \frac{p\left(p(x-x_{in})+\sqrt{t_{in}^2+p^2h^2+4h^2\left[\frac{1}{v_{st}^2}-\frac{1}{v^2}\right]}\right)}{\sqrt{\left(p(x-x_{in})+\sqrt{t_{in}^2+p^2h^2+4h^2\left[\frac{1}{v_{st}^2}-\frac{1}{v^2}\right]}\right)^2-p^2h^2-4h^2\left[\frac{1}{v_{st}^2}-\frac{1}{v^2}\right]}}. \tag{A.8}$$

The second derivative follows from the product rule

$$\frac{\partial^2 t_{refn}(x)}{\partial x^2} = \frac{-p^2\left(p(x-x_{in})+\sqrt{t_{in}^2+p^2h^2+4h^2\left[\frac{1}{v_{st}^2}-\frac{1}{v^2}\right]}\right)^2}{\left[\left(p(x-x_{in})+\sqrt{t_{in}^2+p^2h^2+4h^2\left[\frac{1}{v_{st}^2}-\frac{1}{v^2}\right]}\right)^2-p^2h^2-4h^2\left[\frac{1}{v_{st}^2}-\frac{1}{v^2}\right]\right]^{3/2}} + \frac{p^2}{\sqrt{\left(p(x-x_{in})+\sqrt{t_{in}^2+p^2h^2+4h^2\left[\frac{1}{v_{st}^2}-\frac{1}{v^2}\right]}\right)^2-p^2h^2-4h^2\left[\frac{1}{v_{st}^2}-\frac{1}{v^2}\right]}}. \tag{A.9}$$

Pulling common factors out of this equation gives

$$\begin{aligned}\frac{\partial^2 t_{refn}(x)}{\partial x^2} = {} & -p^2\left[\left(p(x-x_{in})+\sqrt{t_{in}^2+p^2h^2+4h^2\left[\frac{1}{v_{st}^2}-\frac{1}{v^2}\right]}\right)^2-p^2h^2-4h^2\left[\frac{1}{v_{st}^2}-\frac{1}{v^2}\right]\right]^{-3/2} \times \\ & \left[\left(p(x-x_{in})+\sqrt{t_{in}^2+p^2h^2+4h^2\left[\frac{1}{v_{st}^2}-\frac{1}{v^2}\right]}\right)^2 - \right. \\ & \left.\left(p(x-x_{in})+\sqrt{t_{in}^2+p^2h^2+4h^2\left[\frac{1}{v_{st}^2}-\frac{1}{v^2}\right]}\right)^2+p^2h^2+4h^2\left[\frac{1}{v_{st}^2}-\frac{1}{v^2}\right]\right].\end{aligned} \tag{A.10}$$

The final term on the right-hand side equation (A.10) can be simplified by realizing that a quantity is both added and subtracted; from this consideration, we get

$$\frac{\partial^2 t_{refn}(x)}{\partial x^2} = -p^2 \left(p^2h^2 + 4h^2\left[\frac{1}{v_{st}^2} - \frac{1}{v^2}\right]\right) \times$$
$$\left[\left(p(x - x_{in}) + \sqrt{t_{in}^2 + p^2h^2 + 4h^2\left[\frac{1}{v_{st}^2} - \frac{1}{v^2}\right]}\right)^2 - p^2h^2 - 4h^2\left[\frac{1}{v_{st}^2} - \frac{1}{v^2}\right]\right]^{-3/2}. \tag{A.11}$$

Evaluating equation (A.11) at the input point, $x = x_{in}$, yields

$$\frac{\partial^2 t_{refn}(x)}{\partial x^2}\Big|_{x=x_{in}} = -\frac{p^2}{t_{in}^3}\left(p^2h^2 + 4h^2\left[\frac{1}{v_{st}^2} - \frac{1}{v^2}\right]\right). \tag{A.12}$$

When the stacking velocity used in the NMO-correction is correct ($v_{st} = v$), equation (A.12) can be further simplified as

$$\frac{\partial^2 t_{refn}(x)}{\partial x^2}\Big|_{x=x_{in}} = -\frac{p^4h^2}{t_{in}^3}.$$

This is equation (2.50).

We now show some relations pertaining to the first derivatives of $t_{refn}(x)$ and $t_{dmo}(x)$. In order for $t_{refn}(x)$ and $t_{dmo}(x)$ to be tangent to each other at $x = x_{in}$, their derivatives must be equal at that point; hence, $\partial t_{refn}(x)/\partial x = \partial t_{dmo}(x)/\partial x$ at $x = x_{in}$. Evaluating the first derivative of $t_{refn}(x)$, equation (A.8), at $x = x_{in}$ gives

$$\frac{\partial t_{refn}(x)}{\partial x}\Big|_{x=x_{in}} = \frac{p\sqrt{t_{in}^2 + p^2h^2 + 4h^2\left[\frac{1}{v_{st}^2} - \frac{1}{v^2}\right]}}{t_{in}}. \tag{A.13}$$

Using equation (2.46), equation (A.13) can be more concisely written as

$$\frac{\partial t_{refn}(x)}{\partial x}\Big|_{x=x_{in}} = p\frac{t_{out}}{t_{in}}. \tag{A.14}$$

For notational purposes, we use the symbol $\tilde{p}$ to represent $\partial t_{refn}(x)/\partial x$ evaluated at $x = x_{in}$; hence, to show the equivalence, the previous equation can be expressed as

$$\frac{\partial t_{refn}(x)}{\partial x}\Big|_{x=x_{in}} \equiv \tilde{p} = p\frac{t_{out}}{t_{in}}. \tag{A.15}$$

Equation (A.15) is equation (2.45). The first derivative of $t_{dmo}(x)$ at $x = x_{in}$ follows from evaluating equation (A.1) at $x = x_{in}$

$$\frac{\partial t_{dmo}(x)}{\partial x}\Big|_{x=x_{in}} = \frac{t_{out}\ (x_{in} - x_{out})}{h^2\ [1 - (x_{in} - x_{out})^2/h^2]^{3/2}}. \tag{A.16}$$

The DMO ellipse, equation (2.43), can be rearranged as

$$t_{out} = t_{in}\sqrt{1 - \frac{(x_{in} - x_{out})^2}{h^2}}.$$

Substituting equation (A.17) into equation (A.16) for t_{out} gives

$$\frac{\partial t_{dmo}(x)}{\partial x}|_{x=x_{in}} = \frac{t_{in}\ (x_{in} - x_{out})}{h^2\ [1 - (x_{in} - x_{out})^2/h^2]}. \tag{A.17}$$

For tangency at $x = x_{in}$, we set equations (A.15) and (A.17) equal to each other:

$$\tilde{p} = \frac{t_{in}\ (x_{in} - x_{out})}{h^2\ [1 - (x_{in} - x_{out})^2/h^2]}. \tag{A.18}$$

Equation (A.18) can be rewritten as a quadratic equation in terms of $x_{in} - x_{out}$:

$$\tilde{p}(x_{in} - x_{out})^2 + t_{in}(x_{in} - x_{out}) - \tilde{p}h^2 = 0. \tag{A.19}$$

Using the quadratic equation to solve for $x_{in} - x_{out}$ and taking the the positive sign in front of the square root gives

$$x_{in} - x_{out} = \frac{\sqrt{t_{in}^2 + 4\tilde{p}^2h^2} - t_{in}}{2\tilde{p}}.$$

The issue of taking either the positive or negative sign is simply an issue of whether the input point, or point of tangency, is to the right or left of the output point. Note that the above equation for $x_{in} - x_{out}$ is equation (2.44); by squaring both sides and dividing by h^2, we get

$$\frac{(x_{in} - x_{out})^2}{h^2} = \frac{t_{in}^2 + 2\tilde{p}^2h^2 - t_{in}\sqrt{t_{in}^2 + 4\tilde{p}^2h^2}}{2\tilde{p}^2h^2}. \tag{A.20}$$

The DMO ellipse, equation (2.43), can be rearranged as

$$\frac{(x_{in} - x_{out})^2}{h^2} = 1 - \left(\frac{t_{out}}{t_{in}}\right)^2.$$

Substituting this form of the DMO ellipse into the left-hand side equation (A.20) yields

$$1 - \left(\frac{t_{out}}{t_{in}}\right)^2 = \frac{t_{in}^2 + 2\tilde{p}^2h^2 - t_{in}\sqrt{t_{in}^2 + 4\tilde{p}^2h^2}}{2\tilde{p}^2h^2}. \tag{A.21}$$

Solving for t_{out} gives equation (2.47):

$$t_{out} = t_{in}\sqrt{\frac{t_{in}}{2\tilde{p}^2h^2}\left[\sqrt{t_{in}^2 + 4\tilde{p}^2h^2} - t_{in}\right]}.$$

Finally, we derive equation (2.51). To do so, we square both sides of the last equation, which we identified as equation (2.47), to get

$$\left(\frac{t_{out}}{t_{in}}\right)^2 = \frac{t_{in}}{2\tilde{p}^2h^2}\left[\sqrt{t_{in}^2 + 4\tilde{p}^2h^2} - t_{in}\right]. \tag{A.22}$$

After some algebraic manipulation, we solve for $\tilde{p}^2$ in equation (A.22), resulting in

$$\tilde{p}^2 = \frac{t_{in}^2}{h^2}\left(\frac{t_{in}}{t_{out}}\right)^2\left[\left(\frac{t_{in}}{t_{out}}\right)^2 - 1\right]. \tag{A.23}$$

From equations (A.13) and (A.15), we also know that

$$\tilde{p}^2 = \frac{p^2\left(t_{in}^2 + p^2h^2 + 4h^2\left[\frac{1}{v_{st}^2} - \frac{1}{v^2}\right]\right)}{t_{in}^2}. \tag{A.24}$$

Assuming that the stacking velocity is equal to the true velocity ($v_{st} = v$), equation (A.24) becomes

$$\tilde{p}^2 = \frac{p^2\left(t_{in}^2 + p^2h^2\right)}{t_{in}^2}. \tag{A.25}$$

Substituting equation (A.25) into equation (A.23) for $\tilde{p}$, we obtain a quadratic equation in terms of p^2:

$$p^4\frac{h^2}{t_{in}^2} + p^2 - \frac{t_{in}^2}{h^2}\left(\frac{t_{in}}{t_{out}}\right)^2\left[\left(\frac{t_{in}}{t_{out}}\right)^2 - 1\right] = 0. \tag{A.26}$$

Applying the quadratic equation to get a solution for p^2 yields

$$p^2 = \frac{\sqrt{1 + 4\left(\frac{t_{in}}{t_{out}}\right)^2\left[\left(\frac{t_{in}}{t_{out}}\right)^2 - 1\right]} - 1}{2h^2/t_{in}^2}. \tag{A.27}$$

The terms underneath the square root in equation (A.27) together comprise a squared term; as a result, we obtain

$$p^2 = \frac{\left[2\left(\frac{t_{in}}{t_{out}}\right)^2 - 1\right] - 1}{2h^2/t_{in}^2}. \tag{A.28}$$

Simplifying equation (A.28) gives

$$p^2 = \frac{t_{in}^2\left[\left(\frac{t_{in}}{t_{out}}\right)^2 - 1\right]}{h^2}, \tag{A.29}$$

which can in turn be solved for p:

$$p = \frac{t_{in}}{h}\sqrt{(t_{in}/t_{out})^2 - 1}.$$

This is equation (2.51).

Appendix B

Prestack time migration of a horizontal reflector

Having derived the three corrections for zero-offset migration, I now turn to the prestack migration response. For simplicity, I only consider a horizontal reflector. The prestack migration curve is the well-known double square root equation

$$t_{pre}(x) = \frac{1}{2}\sqrt{t_{out}^2 + \frac{4(x - x_{out} + h)^2}{v^2}} + \frac{1}{2}\sqrt{t_{out}^2 + \frac{4(x - x_{out} - h)^2}{v^2}}, \tag{B.1}$$

and the horizontal reflector is at the two-way time

$$t_{ref}(x) = \sqrt{t_{in}^2 + \frac{4h^2}{v^2}}. \tag{B.2}$$

where now the symbol h in this section refers to the half-offset. Note that, since the reflector is horizontal, there is technically no distinction between the input points and the output points ($x_{in} = x_{out}$ and $t_{in} = t_{out}$).

Using the same approach as outlined for zero-offset migration, the scaled transfer function is

$$I(\omega) = \int_{-\infty}^{\infty} e^{i\omega\Delta t(x)}dx, \tag{B.3}$$

where now the time delay, $\Delta t(x)$, refers to equations (B.1) and (B.2)

$$\Delta t(x) = t_{ref}(x) - t_{pre}(x). \tag{B.4}$$

To apply the stationary phase approximation to this integral, I need the second derivative of the phase function $\phi(x) = \omega\Delta t(x)$. It can be verified that the first derivative is zero at the input point. The value of the second derivative at the input point is

$$\frac{\partial^2\phi}{\partial x^2}\Big|_{x=x_{in}} = \frac{-4\omega}{v^2 t_{in}(1 + (4h^2/v^2 t_{in}^2))^{3/2}}. \tag{B.5}$$

Inserting equation (B.5) into the formula for the stationary phase approximation, equation (2.9), gives the prestack migration (non-zero offset) response

$$I(\omega) = \frac{\sqrt{2\pi}}{2}\frac{\exp(-i\pi/4)}{\sqrt{\omega}}v\sqrt{t_{in}}\left(1 + \frac{4h^2}{v^2 t_{in}^2}\right)^{3/4}. \tag{B.6}$$

This expression is equal to the result for zero-offset migration, equation (2.33), when $h = 0$. In equation (B.6), it is evident that the result of summation along the prestack migration curve needs to be multiplied by the *wavelet shaping factor*, $\exp(i\pi/4)\sqrt{\omega}$, and divided by the *geometric spreading factor*, $v\sqrt{t_{in}}$, in order to give the original waveform. An obliquity factor, such as the t_{in}/t_{out} term in equation (2.33), does not appear in equation (B.6) since the reflector I considered here is horizontal. However, there is one last term to be taken into account - the factor of $(1 + (4h^2/v^2t_{in}^2))^{3/4}$. This term is zero for the case of zero-offset and hence did not appear in the earlier analysis. Correcting for this factor requires multiplying the result of the summation by $(1 + (4h^2/v^2t_{in}^2))^{-3/4}$, thereby damping the far offsets. For $2h = vt_{in}$, or an offset to depth ratio of 1, this factor which I call the *offset-factor* is approximately 0.5946.

Appendix C

Modeling of a linear-slip interface

We chose SEM to simulate fault reflectivity for its ability to allow a free-form mesh and in order to include the possibility of slip at interfaces in our numerical models. As evidence of SEM's ability to handle challenging boundary conditions, it has recently been applied to wave propagation near a fluid-solid interface (Komatitsch *et al.*, 2000). However, interfacial slip had not yet, to our knowledge, been implemented in SEM. In fact, Komatitsch & Tromp (2003) claimed in the description of their SEM code that "at every internal boundary, both the displacement and the traction need to be continuous", in clear contradiction to slip.

For a normally incident *P*-wave, the linear-slip boundary condition can be expressed as Schoenberg (1980)

$$u_z^+ - u_z^- = \eta_N \sigma_{zz} \tag{C.1}$$

$$\sigma_{zz}^+ = \sigma_{zz}^- \tag{C.2}$$

where the superscript (-) refers to the side of the interface on which the wave is incident, (+) the other side of the interface, u_z is the displacement in the direction of propagation, and σ_{zz} is the normal stress. The parameter η_N is called the normal compliance and quantifies the degree of slip along the interface. For $\eta_N = 0$,the interface is welded, and for $\eta_N = \infty$, it is a free surface. The boundary condition described by equations (C.1) and (C.2) can be obtained in the limit of a thin, weak layer in welded contact with its surrounding rock. Linear-slip has been suggested as a good model for scattering from faults and fractures (Coates & Schoenberg, 1995). With this in mind, it is important not to confuse the slip model in equations (C.1) and (C.2) with slip that occurs along a fault during an earthquake. The linear-slip model entails some slipping at the interface that is the order of particle displacements during the passage of a seismic wave ($\sim 10^{-6}$ m). Active, earthquake-generating faults typically slip on a length scale 3 to 4 orders of magnitude larger ($\sim 10^{-3}$ - 10^{-2} m). Earthquake slip is also hysteretic, whereas interfaces undergoing linear-slip return to their equilibrium state after the seismic wave has moved on.

To implement the linear-slip model in SEM, the weak form of the equation of motion is needed

$$\int\int \rho \, \ddot{u} \, \phi + \int\int \nabla\phi : c : \nabla u - \int \tau \, \phi = 0, \tag{C.3}$$

where u is the displacement, ρ is the density, τ is the traction on the boundary of the computational domain, c is the elastic stiffness tensor, and ϕ is the test function. The semicolons in equation (C.3) represent tensor multiplication. After discretizing the displacement, equation (C.3) can be written as a matrix equation

$$M\ddot{u} = -Ku + B\tau, \tag{C.4}$$

with M and K the mass and stiffness matrices, respectively. The last term is non-zero only on the part of the boundary where slip occurs; this is described by the matrix B. The essence of this implementation is that two separate meshes on either side of the slip discontinuity (let's call them mesh 1 and mesh 2) are put into communication via the last term in equation (C.4). To get linear-slip between the two meshes along a direction normal to their contact, we substitute equation (C.1) for the traction into equation (C.4) for meshes 1 and 2 to get two matrix equations

$$\begin{aligned} M_1\ddot{u}_1 &= -K_1 u_1 + \eta_N^{-1} B_1(u_1^z - u_2^z) \\ M_2\ddot{u}_2 &= -K_2 u_2 - \eta_N^{-1} B_2(u_1^z - u_2^z), \end{aligned} \tag{C.5}$$

where the asymmetry of the ±-signs between the two last terms is in accordance with Newton's third law and the superscript z means the normal component of the displacement. In the formulation we have outlined here, the slip law, equation (C.1), enters into the equation of motion by a substitution of the slip for the traction at the fault.

The SEM implementation of equation (C.5) utilizes an explicit Newmark scheme (Zienkiewicz & Taylor, 2000) whose algorithm consists of a predictor, a solver, and a corrector:

```
for n=1:N

PREDICTOR
$u_1$(n+1) = $u_1$(n) + $\frac{1}{2}\Delta$t $v_1$(n)
$u_2$(n+1) = $u_2$(n) + $\frac{1}{2}\Delta$t $v_2$(n)
$v_1$(n+1) = $v_1$(n)
$v_2$(n+1) = $v_2$(n)

SOLVER
solve both equations in (C.5) for $\ddot{u}$(n+1)
using predicted values of $u$(n+1) and $v$(n+1)
straightforward since $M_1$ and $M_2$ are diagonal

CORRECTOR
$u_1$(n+1) = $u_1$(n+1) + $\frac{1}{2}\Delta$t $v_1$(n) + $\frac{1}{2}\Delta$t$^2$ $\ddot{u}_1$(n+1)
$u_2$(n+1) = $u_2$(n+1) + $\frac{1}{2}\Delta$t $v_2$(n) + $\frac{1}{2}\Delta$t$^2$ $\ddot{u}_2$(n+1)
$v_1$(n+1) = $v_1$(n+1) + $\Delta$t $\ddot{u}_1$(n+1)
$v_2$(n+1) = $v_2$(n+1) + $\Delta$t $\ddot{u}_2$(n+1)

end
```

where, in the above algorithm, n stands for the previous time step, $\ddot{u}$ is the acceleration,

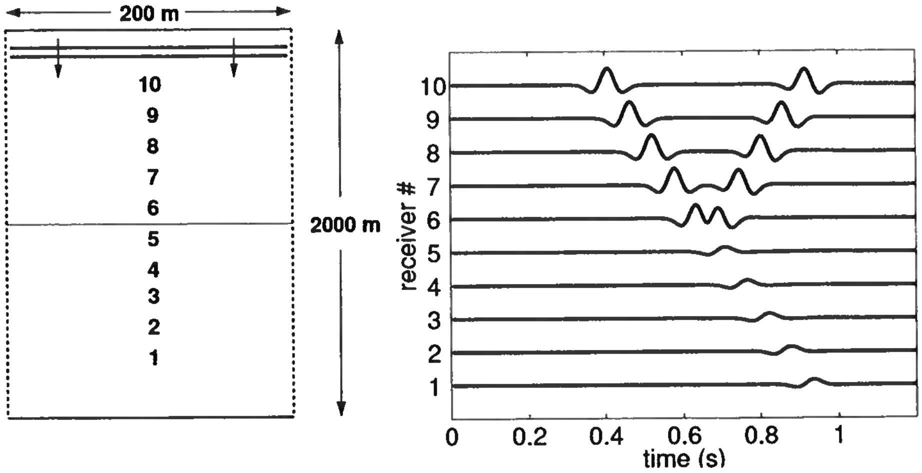

Figure C.1. Numerical simulation of a normally incident P-wave scattering from a linear-slip interface. On the top is the model, showing ten numbered receiver locations and a plane wave incident from the upper end of the model. The linear-slip interface is between the receivers 5 and 6. On the bottom are seismograms taken at each of the receivers. At $t = 6$ s, the incident wave reflects from the linear-slip interface. The media above and below the linear-slip interface are identical and, therefore, no reflection would occur had there been no slip.

Δt is the time step increment, and v is the velocity.

Waveforms computed with this implementation are displayed in Fig. C.1. Our model is an elongated 2D block, whose side boundaries, shown as dashed in Fig. C.1, are periodic and whose upper and lower boundaries are absorbing. Consistent with the periodic boundary condition, we excite a unidirectional plane P-wave from the base of the block. In front of the plane wave, we measure the wavefield with ten receivers. A slip interface cuts through the center of the block, between receivers 5 and 6, which is characterized by a normal compliance of 2.2×10^{-8} m/Pa. The slip interface has also a shear compliance, but the P-wave is incident normally and excites no shear. The media on either side of the slip interface are identical with density, P-velocity, and S-velocity of 2300 kg/m^3, 2000 m/s, and 1000 m/s, respectively. The plane wave source waveform is a Ricker wavelet with a dominant frequency of 10 Hz.

We plot the resulting wavefield in the left portion of Figure C.1. For the value of slip used in this example, the slip interface virtually acts as a stress-free surface, almost totally reflecting the incident wave. As a result, only a small fraction of the energy transmits through the interface. From the analytic expressions for the frequency-dependent reflection and transmission coefficients at such a slip interface (Chaisri & Krebes, 2000), we find R_{PP} = 0.95 and T_{PP} = 0.30 for an incident frequency of 10 Hz. These values are qualitatively in agreement with the displayed waveforms in Figure C.1.

Appendix D

Stability of a split node

To obtain a typical stability condition for a split node, we consider the simple case of a finite-element implementation of the 1D scalar wave equation. This case can be thought of as that of a normally incident SH-wave on a fracture. The linear basis functions ϕ used here are given as

$$\phi_K(z) = \begin{cases} (z - z_{K-1})/h & \text{if } z_{K-1} \leq z \leq z_K, \\ (z_{K+1} - z)/h & \text{if } z_K \leq z \leq z_{K+1}, \\ 0 & \text{otherwise,} \end{cases} \tag{D.1}$$

where h is the grid spacing. After applying the weak formulation to the 1D wave equation and integrating in space, the resulting matrix equation to be solved in time is

$$M\ddot{\vec{u}} = -c^2 K\vec{u}, \tag{D.2}$$

where M and K are the mass and stiffness matrices, $c^2 = \mu/\rho$ is the squared wavespeed (assumed to be constant here), and u is the (out of plane) displacement field ($u = u_y$). For the linear basis functions used here, the entries of these matrices can be calculated exactly. For the (consistent) mass matrix, $M_{J,K}$, the non-zero entries are

$$\int_0^L \phi_K \phi_J dz = 2h/3 \qquad \text{for } J = K \tag{D.3}$$

$$\int_0^L \phi_K \phi_J dz = h/6 \qquad \text{for } J = K+1, J = K-1. \tag{D.4}$$

where h is the spatial grid spacing (assumed to be constant). This means that M is symmetric and tridiagonal. Similarly, the stiffness matrix, $S_{J,K}$, is also symmetric tridiagonal and the non-zero entries are

$$\int_0^L \frac{\partial \phi_K}{\partial z}\frac{\partial \phi_J}{\partial z} dz = 2/h \qquad \text{for } J = K \tag{D.5}$$

$$\int_0^L \frac{\partial \phi_K}{\partial z}\frac{\partial \phi_J}{\partial z}dz = -1/h \qquad \text{for } J = K+1, J = K-1. \tag{D.6}$$

For a single split node, the matrices M and K have some structure. In fact, the left hand side of equation (D.2) is

$$\begin{bmatrix}
\ddots & \ddots & & & & & & \\
\ddots & 2h/3 & h/6 & & & & & \\
 & h/6 & 2h/3 & h/6 & & & & \\
 & & h/6 & h/3 & 0 & & & \\
 & & & 0 & h/3 & h/6 & & \\
 & & & & h/6 & 2h/3 & h/6 & \\
 & & & & & h/6 & 2h/3 & \ddots \\
 & & & & & & \ddots & \ddots
\end{bmatrix}
\begin{bmatrix}
\vdots \\ \ddot{u}_{m-2} \\ \ddot{u}_{m-1} \\ \ddot{u}_{m} \\ \ddot{u}_{m+1} \\ \ddot{u}_{m+2} \\ \ddot{u}_{m+3} \\ \vdots
\end{bmatrix} \tag{D.7}$$

where the spatial location on the grid is indicated by the subscripts $m-1$, m, etc. In equation (D.7), the split node is located between the gridpoints m and $m+1$. Similarly, the right hand side of equation (D.2) is

$$-c^2\begin{bmatrix}
\ddots & \ddots & & & & & & \\
\ddots & 2/h & -1/h & & & & & \\
 & -1/h & 2/h & -1/h & & & & \\
 & & -1/h & 1/h & 0 & & & \\
 & & & 0 & 1/h & -1/h & & \\
 & & & & -1/h & 2/h & -1/h & \\
 & & & & & -1/h & 2/h & \ddots \\
 & & & & & & \ddots & \ddots
\end{bmatrix}
\begin{bmatrix}
\vdots \\ u_{m-2} \\ u_{m-1} \\ u_{m} \\ u_{m+1} \\ u_{m+2} \\ u_{m+3} \\ \vdots
\end{bmatrix} \tag{D.8}$$

We use the expressions in equations (D.7) and (D.8) to find the stability criterion for a split node. To further simplify the calculation, we lump the mass matrix shown in equation (D.7) so that the left hand side of equation (D.2) is instead

$$\begin{bmatrix} \ddots & \ddots & & & & & & \\ \ddots & h & 0 & & & & & \\ & 0 & h & 0 & & & & \\ & & 0 & h/2 & 0 & & & \\ & & & 0 & h/2 & 0 & & \\ & & & & 0 & h & 0 & \\ & & & & & 0 & h & \ddots \\ & & & & & & \ddots & \ddots \end{bmatrix} \begin{bmatrix} \vdots \\ \ddot{u}_{m-2} \\ \ddot{u}_{m-1} \\ \ddot{u}_m \\ \ddot{u}_{m+1} \\ \ddot{u}_{m+2} \\ \ddot{u}_{m+3} \\ \vdots \end{bmatrix} \tag{D.9}$$

The lumping is accomplished by summing the rows and placing the result on the main diagonal. This essentially reduces the finite-element scheme into a finite-difference scheme. The difference is that care has been taken with the inclusion of a split-node and, as seen in the next paragraph, the boundary condition at the split-node can be accounted for in an entirely straightforward manner. This is in contrast to the "fictitious lines" in Alterman & Loewenthal (1970) and Kelly *et al.* (1976).

Setting the m-th rows of the matrix/vector multiplications depicted in equations (D.8) and (D.9) equal to each other, in accordance with the equation of motion, equation (D.2), gives the spatially discretized equation of motion at the split node

$$\frac{h}{2}\ddot{u}_m = \frac{c^2}{h}u_{m-1} - \frac{c^2}{h}u_m. \tag{D.10}$$

Note that there is currently no communication across the split node, between the gridpoint at m and at $m+1$. Interaction between these gridpoints is accomplished by including the traction σ_{yz} between the nodes with the slip law

$$u_{m+1} - u_m = \eta\sigma_{yz}, \tag{D.11}$$

where the coupling is described by the free parameter η (the compliance). Note that $\eta = 0$ is a welded contact and $\eta = \infty$ is a stress-free boundary. Using the slip law and Hooke's Law $\mu\ \partial u/\partial z = \sigma_{yz}$, the traction at the split node can be included into equation (D.10)

$$\frac{h}{2}\ddot{u}_m = \frac{c^2}{h}u_{m-1} - \frac{c^2}{h}u_m + \frac{c^2}{\mu\eta}(u_{m+1} - u_m). \tag{D.12}$$

A time integration scheme must be chosen for equation (D.12). An explicit scheme is obtained by evaluating all the u-terms on the right hand side at the previous timestep, denoted n. For notational purposes, we show u_{m-1} evaluated at timestep n by $u_{m-1,n}$. For the left hand side, we choose the second difference approximation to $\ddot{u}_m$ centered at timestep n

$$\ddot{u}_m = \frac{u_{m,n+1} - 2u_{m,n} + u_{m,n-1}}{\Delta t^2}, \tag{D.13}$$

where Δt is the time spacing. The algorithm outlined here is to be solved for $u_{m,n+1}$ in equation (D.13) by knowing the displacements at timesteps n and $n-1$. Such a multistep algorithm can be seen as equivalent to a single-step algorithm with prediction.

Inserting equation (D.13) into equation (D.12) results in the complete finite-element stencil

$$\frac{h}{2\Delta t^2}u_{m,n+1} - \frac{h}{\Delta t^2}u_{m,n} + \frac{h}{2\Delta t^2}u_{m,n-1} = \frac{c^2}{h}u_{m-1,n} - \frac{c^2}{h}u_{m,n} + \frac{c^2}{\mu\eta}(u_{m+1,n} - u_{m,n}). \quad (D.14)$$

To investigate the stability of this scheme, we study the exponential growth or decay of the odd eigenmodes of u. These eigenmodes are antisymmetric with respect to the slipping interface. We chose the odd eigenmodes since the symmetric modes have no slip. If there wasn't a slipping interface and the medium was homogeneous, harmonic functions would be inserted for both the spatial and temporal variation of u; for the case of slipping interface, care has to be taken in treating the spatial variation since the medium is not homogeneous. This extra care amounts to determining an additional free parameter at the interface, as demonstrated shortly.

An odd eigenmode for a single linear-slip interface located at the depth z_s is

$$\begin{aligned} u(z,t) &= \tilde{U}(z)e^{i\omega t} \\ \tilde{U}(z) &= \operatorname{sgn}(z-z_s)\sin(k|z-z_s|+\phi), \end{aligned} \quad (D.15)$$

where $\tilde{U}(z)$ is the spatial variation of the odd eigenmode, ϕ is a free parameter determined from the linear-slip boundary condition of equation (D.11), k is the wavenumber, and ω is the frequency. As stated above, the slip interface is between the m and $m+1$ gridpoints, which are both located at the depth z_s. To be precise, the m gridpoint is obtained in the limit $z \rightarrow z_s$ for values $z < z_s$. Similarly, the $m+1$ gridpoint is obtained in the limit $z \rightarrow z_s$ for values $z > z_s$. Mathematically, this is the difference between a left-hand and right-hand limit. It matters in the context of equation (D.15) since the signum function is discontinuous at $z = z_s$.

Taking the proper limits, the spatial components of an odd eigenmode at the m and $m+1$ gridpoints are

$$\begin{aligned} \tilde{U}_m &= -\sin\phi, \\ \tilde{U}_{m+1} &= \sin\phi. \end{aligned} \quad (D.16)$$

From these equations, it can be seen that ϕ drives the magnitude of the slip discontinuity. We now use the relationships in equation (D.16) to determine ϕ from the linear-slip boundary condition of equation (D.11). For this, we need the shear stress component σ_{yz}, which by Hooke's Law is equal to $\mu\ \partial u/\partial z$. In other words, we need the value of the derivative of u at z_s. From equation (D.15)

$$\frac{\partial \tilde{U}}{\partial z} = k\cos(k|z-z_s|+\phi). \quad (D.17)$$

Therefore, at z_s, $\sigma_{yz} = \mu k \cos\phi$. Inserting this expression for σ_{yz} and the relationships in equation (D.16) into the boundary condition of equation (D.11) yields

$$\tan\phi = \frac{\eta\mu k}{2}. \tag{D.18}$$

From this equation, $\sin\phi$ and $\cos\phi$ can be found

$$\begin{aligned}\sin\phi &= \frac{\pm\eta\mu k}{\sqrt{\eta^2\mu^2k^2+4}}\\ \cos\phi &= \frac{\pm 2}{\sqrt{\eta^2\mu^2k^2+4}}.\end{aligned} \tag{D.19}$$

Since it does not matter, we take the postive sign in equation (D.19).

We are now in a position to write down the discrete forms of the antisymmetric eigenmodes at the gridpoints $m-1$, m, and $m+1$ using equation (D.15)

$$\begin{aligned}u_{m+1,n} &= \sin\phi\; e^{i\omega n\Delta t}\\ u_{m,n} &= -\sin\phi\; e^{i\omega n\Delta t}\\ u_{m-1,n} &= -\sin(kh+\phi) = -(\sin kh\cos\phi + \cos kh\sin\phi)\; e^{i\omega n\Delta t},\end{aligned} \tag{D.20}$$

where the time t is discretized by timestep n and time spacing Δt. Using equation (D.19) and the substitution

$$\zeta^n = e^{i\omega n\Delta t}, \tag{D.21}$$

equation (D.20) can be written finally as

$$\begin{aligned}u_{m+1,n} &= \frac{\eta\mu k}{\sqrt{\eta^2\mu^2k^2+4}}\;\zeta^n\\ u_{m,n} &= \frac{-\eta\mu k}{\sqrt{\eta^2\mu^2k^2+4}}\;\zeta^n\\ u_{m-1,n} &= -\frac{2\sin kh + \eta\mu k\cos kh}{\sqrt{\eta^2\mu^2k^2+4}}\;\zeta^n.\end{aligned} \tag{D.22}$$

In equation (D.22), the variation with timestep n is trivial, requiring only a change in the exponent of ζ. Taking the information in equation (D.20), using it in equation (D.14), and organizing terms yields

$$\begin{aligned}0 \;=\; & \left[\frac{h\eta\mu k}{2\Delta t^2}\zeta^2 + \frac{c^2}{h}(\eta\mu k - 2\sin kh - \eta\mu k\cos kh)\zeta\right.\\ & \left. -\frac{h\eta\mu k}{\Delta t^2}\zeta + 2c^2k\zeta + \frac{h\eta\mu k}{2\Delta t^2}\right]\zeta^{n-1}.\end{aligned} \tag{D.23}$$

In order to have non-trivial solutions, the terms inside the brackets in equation (D.23) must equal zero.

Dividing equation (D.23) by the coefficient of the ζ^2 term and setting the terms inside the brackets to zero gives

$$0 = \zeta^2 - 2[1 - \frac{\Delta t^2 c^2}{h^2 \eta \mu k}(\eta \mu k - \eta \mu k \cos kh - 2 \sin kh) - \frac{2\Delta t^2 c^2}{\mu \eta h}]\zeta + 1. \tag{D.24}$$

For the numerical scheme to be stable, the two roots of equation (D.24) should have magnitudes less than or equal to 1. This means that solutions are not exponentially growing in time. Let's find the conditions such that this is the case.

Note that equation (D.24) has the general form

$$0 = \zeta^2 - v\zeta + 1, \tag{D.25}$$

where the coefficient v is a complex number. Denote the two (possibly complex) roots of equation (D.25) ζ_1 and ζ_2. From the quadratic formula, it is known that for any v

$$\begin{aligned} \zeta_1 + \zeta_2 &= v \\ \zeta_1 \zeta_2 &= 1. \end{aligned} \tag{D.26}$$

These equalities are a particular example of what are known as Viète's formula's and are analogous to the trace of a matrix being equal to the sum of its eigenvalues and the determinant being equal to the product of its eigenvalues. With help of the triangle inequality, the two equalities in equation (D.26) can be recast in terms of the magnitudes of ζ_1 and ζ_2, shown as $|\zeta_1|$ and $|\zeta_2|$. For the first equality of equation (D.26)

$$|\zeta_1| + |\zeta_2| \geq |\zeta_1 + \zeta_2| = |v|. \tag{D.27}$$

And, for the second equality

$$|\zeta_1|\,|\zeta_2| = |\zeta_1 \zeta_2| = |1| = 1. \tag{D.28}$$

This is necessary since it is the magnitude of the roots of equation (D.24) that determine the stability of the algorithm. Since we need both $|\zeta_1| \leq 1$ and $|\zeta_2| \leq 1$ for stability, equation (D.28) tells us that

$$|\zeta_1| = 1 \quad \text{and} \quad |\zeta_2| = 1. \tag{D.29}$$

This makes sense because we are solving a wave equation whose solutions should not decay with time. Using this information together with equation (D.27) gives

$$2 = |\zeta_1| + |\zeta_2| \geq |v| \tag{D.30}$$

or in other words,

$$|\frac{v}{2}| \leq 1. \tag{D.31}$$

Applying this stability criterion, valid for the general quadratic form of equation (D.25), to the expression describing the roots in equation (D.24) gives

$$|1-\frac{\Delta t^2c^2}{h^2\eta\mu k}(\eta\mu k-\eta\mu k\cos kh-2\sin kh)-\frac{2\Delta t^2c^2}{\mu\eta h}|\le 1. \tag{D.32}$$

From this expression, note that in the limit of low frequencies $kh \rightarrow 0$ (which corresponds to waves that are well sampled by the grid), this stability criterion is always satisfied. Typically we look for instabilities to occur for waves that are near the spatial Nyquist frequency ($kh = \pi$). For this frequency, equation (D.32) becomes

$$|1-\frac{2\Delta t^2c^2}{h^2}-\frac{2\Delta t^2c^2}{\mu\eta h}|\le 1. \tag{D.33}$$

The term inside the absolute value on the left hand side of equation (D.33) is real-valued; therefore, the inequality may be rewritten as two simultaneous inequalities

$$-1\le 1-\frac{2\Delta t^2c^2}{h^2}-\frac{2\Delta t^2c^2}{\mu\eta h}\le 1. \tag{D.34}$$

Since the terms being subtracted from 1 in the middle of equation (D.34) are both positive, the right hand inequality is always satisfied and may be ignored. The other inequality is meaningful

$$\begin{aligned}
-1 &\le 1-\frac{2\Delta t^2c^2}{h^2}-\frac{2\Delta t^2c^2}{\mu\eta h}\\
\frac{2\Delta t^2c^2}{h^2}+\frac{2\Delta t^2c^2}{\mu\eta h} &\le 2\\
\frac{\Delta t^2c^2}{h^2}\left(1+\frac{h}{\mu\eta}\right) &\le 1\\
\frac{c\Delta t}{h}\sqrt{1+\frac{h}{\mu\eta}} &\le 1\\
c\Delta t &\le \frac{h}{\sqrt{1+(h/\mu\eta)}}
\end{aligned} \tag{D.35}$$

This stability criterion has the same general form as that for a regular node that is not split ($c\Delta t \le h$). However, the compliance of the split node η does enter into the stability criterion uniquely in the inverse square root appearing on the right hand side. For a free surface, $\eta = \infty$ and the factor with the compliance vanishes and the stability criterion can be met. As the compliance approaches zero, though, the denominator becomes large and the stability criterion becomes harder to satisfy. For given values of c, h, μ, and Δt, there is a lower value for compliance η_{min} past which the algorithm becomes unstable at the split node. This precludes the possibility of a welded interface ($\eta = 0$), though for certain values of c, h, μ, and Δt, η_{min} may be so small that an effectively welded interface can be realized.

Appendix E

Linearized reflection coefficients from a fracture

As demonstrated in Groenenboom (1998), fractures act as an interface over which slip occurs during the passage of a seismic wave. Therefore, a good place to begin modeling fractures is with linear-slip theory. Schoenberg (1980) formally introduced the concept of a linear-slip interface to the exploration seismology community. The linear-slip interface is characterized by the following boundary condition for the SH case:

$$u_y^+ - u_y^- = k_T \sigma_{yz}, \tag{E.1}$$

$$\sigma_{yz}^+ = \sigma_{yz}^-, \tag{E.2}$$

where k_T is called the shear (or transverse) compliance of the linear-slip interface. In equations (E.1) and (E.2), the superscript (-) refers to the side of the interface on which the wave is incident, (+) the other side of the interface, u_y is the displacement out of the plane of wave propagation, and σ_{yz} is the shear stress. The shear compliance, k_T, quantifies the degree of slip along the interface. For $k_T = 0$, the interface is welded ($u_y^+ = u_y^-$), and for $k_T = \infty$, it is a free surface. Hence, a linear-slip interface is a general interface condition that includes the usual welded case. In a recent case study from the North Sea, Worthington & Hudson (2000) have modeled a fault zone as a series of closely spaced linear-slip interfaces.

A common tool to diagnose the elastic properties of a reflecting interface in exploration seismology is called amplitude-versus-offset, or AVO. Linearized expressions of reflection coefficients for small changes in the elastic properties across an interface have proven useful in linear AVO-inversion (Demirbag *et al.*, 1993). The linearized expressions provide a set of basis functions in terms of incidence/reflection angle that can be used in a standard least-squares inversion (as described in Chapter 15 of Press *et al.* (1992)). Here, we discuss the linearized approximation of the reflection coefficients for an interface which allows slip. The formulas can be seen as generalizations of existing expressions for welded (no-slip) interfaces.

E.1 Reflection of an SH-wave

The linearized reflection coefficient for an SH-wave at a planar interface between two isotropic halfspaces, obtained by enforcing equations (E.1) and (E.2) for a harmonic elastic disturbance and keeping first order terms in the elastic contrasts and the slip-discontinuity, is:

$$R_{SH} \approx -\frac{1}{2}\left(\frac{\Delta\rho}{\rho}+\frac{\Delta\beta}{\beta}\right)+\frac{1}{2}\frac{\Delta\beta}{\beta}\tan^2\theta - i\frac{\omega k_T \rho\beta}{2}\cos\theta, \tag{E.3}$$

where $\Delta\beta$ and $\Delta\rho$ are the changes in S-velocity and density at the interface, β and ρ are the average S-velocity and density of the two halfspaces, ω is the angular frequency of the incident wave, k_T is the shear compliance of the interface, and θ is the reflection/incidence angle. The approximation in equation (E.3) holds for small relative changes in the medium parameters ($\Delta\beta/\beta$, $\Delta\rho/\rho \ll 1$), small dimensionless compliance ($\omega k_T\rho\beta \ll 1$), and small angles of incidence (surely not greater than the critical angle). For a welded interface ($k_T = 0$), equation (E.3) agrees with Thomsen's expression (Thomsen, 1993) for the case of isotropic halfspaces. We do not show the lengthy derivation of equation (E.3); the technique for obtaining linearized reflection coefficients is outlined in (Wang, 1999).

Seismologists usually assume that interfaces are welded and, as a result, reflection coefficients are *real* and *frequency-independent*. As seen from equation (E.3), neither of these characteristics are true when slip occurs at the interface. The third term in equation (E.3) is the contribution to the reflection coefficient from slip. There is a factor of $i\omega$ in the third term since the linear-slip interface can be obtained in the limit of a thin, low shear strength bed (Schoenberg, 1980) whose reflection, as pointed out a long time ago by Widess (1973), is the derivative of the incident wave.

To overcome the complication of having a complex-valued reflection coefficient, it may be instructive to study the squared magnitude of equation (E.3)

$$\begin{aligned} |R_{SH}|^2 &\approx \frac{1}{4}\left(\frac{\Delta\rho}{\rho}+\frac{\Delta\beta}{\beta}\right)^2 - \frac{1}{4}\frac{\Delta\beta}{\beta}\left(\frac{\Delta\rho}{\rho}+\frac{\Delta\beta}{\beta}\right)\tan^2\theta + \frac{1}{4}\left(\frac{\Delta\beta}{\beta}\right)^2\tan^4\theta \\ &+\frac{\omega^2 k_T^2\rho^2\beta^2}{4}\cos^2\theta. \end{aligned} \tag{E.4}$$

The angle dependencies in equation (E.4) can be modified to reveal which terms are sensitive at zero-offset, near-offsets, and far-offsets. This is the approach taken by Shuey (1985). To highlight the angle dependencies, we use the following identities:

$$\begin{aligned} \cos^2\theta &= 1-\sin^2\theta, \\ \tan^2\theta &= \sin^2\theta+\tan^2\theta\,\sin^2\theta, \\ \tan^4\theta &= \tan^2\theta\,\sin^2\theta+\tan^4\theta\,\sin^2\theta. \end{aligned}$$

Equation (E.4) can then be rewritten as:

$$\begin{aligned} |R_{SH}|^2 \approx\ & \frac{1}{4}\left[\left(\frac{\Delta\rho}{\rho}+\frac{\Delta\beta}{\beta}\right)^2+\omega^2 k_T^2\rho^2\beta^2\right] \\ & -\frac{1}{4}\left[\frac{\Delta\beta}{\beta}\left(\frac{\Delta\rho}{\rho}+\frac{\Delta\beta}{\beta}\right)+\omega^2 k_T^2\rho^2\beta^2\right]\sin^2\theta \\ & -\frac{1}{4}\frac{\Delta\beta}{\beta}\frac{\Delta\rho}{\rho}\tan^2\theta\,\sin^2\theta \\ & +\frac{1}{4}\left(\frac{\Delta\beta}{\beta}\right)^2\tan^4\theta\,\sin^2\theta. \end{aligned} \tag{E.5}$$

The first term in equation (E.5) dominates at zero offset ($\theta \approx 0$). At near-offsets ($0 < \theta < 35°$), the second term, proportional to $\sin^2\theta$, becomes important. The third and fourth terms in equation (E.5) are sensitive at far-offsets ($35° < \theta$). Since only the first two terms contain k_T, it can be said that far-offsets are not affected by slip at an interface for the *SH* case.

E.2 *PP*-reflection

For the *P-SV*-case, the linear-slip interface is described by the boundary conditions:

$$\begin{aligned} u_z^+ - u_z^- &= k_N\sigma_{zz}, \\ \sigma_{zz}^+ &= \sigma_{zz}^-, \\ u_x^+ - u_x^- &= k_T\sigma_{xz}, \\ \sigma_{xz}^+ &= \sigma_{xz}^-, \end{aligned}$$

where now two compliances, the normal (k_N) and shear (k_T) compliance, describe the linear-slip interface. The linearized *PP*-reflection coefficient at a planar interface between two isotropic halfspaces that results is:

$$\begin{aligned} R_{PP} \approx\ & \left[\frac{1}{2}-2\left(\frac{\beta}{\alpha}\right)^2\sin^2\theta\right]\frac{\Delta\rho}{\rho}+\frac{1}{2}\sec^2\theta\,\frac{\Delta\alpha}{\alpha}-4\left(\frac{\beta}{\alpha}\right)^2\sin^2\theta\,\frac{\Delta\beta}{\beta} \\ & +i\left[\frac{1}{2}-2\left(\frac{\beta}{\alpha}\right)^2\sin^2\theta\right]\sec\theta\;\omega k_N\rho\alpha \\ & -2i\left(\frac{\beta}{\alpha}\right)^3\cos\theta\,\sin^2\theta\;\omega k_T\rho\beta, \end{aligned} \tag{E.6}$$

where $\Delta\alpha$, $\Delta\beta$, and $\Delta\rho$ are the changes in *P*-velocity, *S*-velocity, and density of the two halfspaces, α, β, and ρ are the average *P*-velocity, *S*-velocity, and density of the two halfspaces, ω is the angular frequency of the incident wave, k_T and k_N are the shear and normal compliances of the interface, and θ is the reflection/incidence angle. The approximation in

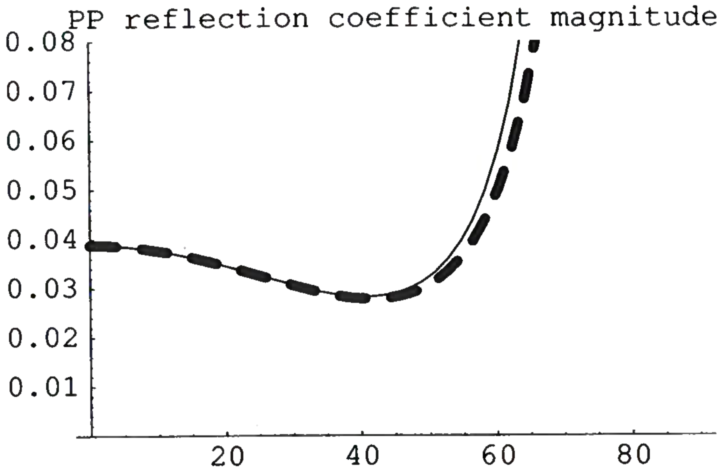

Figure E.1. The linearized reflection coefficient as a function of angle (thick, dashed line) and the exact reflection coefficient for a welded interface (k_T, $k_N = 0$).

equation (E.6) holds for small relative changes in the medium parameters ($\Delta\alpha/\alpha$, $\Delta\beta/\beta$, $\Delta\rho/\rho \ll 1$), small dimensionless shear compliance ($\omega k_T \rho\beta \ll 1$), small dimensionless normal compliance ($\omega k_N \rho\alpha$ sec $\theta \ll 1$), and small angles of incidence. Note that the condition for a small dimensionless normal compliance has an angular dependence. For a welded interface (k_T, $k_N = 0$), the imaginary terms in equation (E.6) vanish and the linearized PP-reflection coefficient agrees with equation 5.44 of Aki & Richards (1980). Again, we omit the lengthy derivation of equation (E.6), but it follows from Wang (1999).

In Figures 1 through 3, we compare the linearized PP-reflection coefficient to the exact PP-reflection coefficient for the parameters shown in Table II while varying the amount of slip (the value of the compliance) at the interface. Since the reflection coefficient for an interface with slip is frequency dependent, we set the frequency of the incident wave to 10 Hz for all the examples. The elastic contrasts resulting from the parameters listed in Table II are sufficiently small to expect agreement between the linearized approximation and the exact reflection coefficient at small incidence/reflection angles. The formulas for the exact PP-reflection coefficient, including possible slip, can be found in Chaisri & Krebes (2000).

Shown in Figure (E.1) is the magnitude of the exact PP-reflection coefficient as a function of angle for a welded interface (with elastic contrasts from Table II) and its linearized approximation. Figure (E.1) is the typical case assumed in AVO studies, that of a welded interface, and the approximation is seen to be in good agreement for angles out to about 50°. In Figure (E.2), we plot the same linearized reflection coefficient as in Figure (E.1), assuming a welded interface; however, for the exact reflection coefficient, we include a small amount of slip by using non-zero values for the compliances: $k_T = 5.0 \times 10^{-10}$ m/Pa and $k_N = 2.5 \times 10^{-10}$ m/Pa. By small, we mean that the dimensionless compliances, $\omega k_T \rho\beta$ and $\omega k_N \rho\alpha$ secθ, are much less than one. Without the contribution of slip at the interface,

elastic property	value
density of incident medium	2300 kg/m^3
P-velocity of incident medium	2800 m/s
S-velocity of incident medium	1400 m/s
density of reflecting medium	2400 kg/m^3
P-velocity of reflecting medium	2900 m/s
S-velocity of reflecting medium	1450 m/s

Table E.1. The earth model used to compute the reflection coefficients.

the linearized reflection coefficient underestimates the exact reflection coefficient.

Using equation (E.6), the magnitude of the linearized reflection coefficient for an interface with slip can be compared to the exact reflection coefficient. The comparison is shown in Figure (E.3). The inclusion of slip in the expression for the linearized reflection coefficient has resulted in better agreement with the exact reflection coefficient (good agreement up to 45°). Qualitatively, from looking at Figure (E.2), the presence of non-weldedness at an interface causes the AVO intercept to increase (magnitude at zero-offset is greater) and the AVO gradient to increase (the curve steepens with increasing angle) from their values for the case of no slip.

The linearized reflection coefficients for an interface with slip give some insight into the influence of the various elastic contrasts and compliances that is unavailable from the complicated exact expressions. Also, the linearized formulas should be useful in a least-squares, linear inversion of AVO for rock and fracture properties. Some unanswered questions include: (a) whether, in addition to the PP-reflection, the PS-reflection is necessary to uniquely determine all the parameters from a general linear-slip interface in the presence of random noise, (b) how to deal with the frequency dependence of the reflection in the inversion procedure, (c) how time-lapse measurements can be incorporated into the AVO analysis, and (d) whether, in the P-SV case, a dry fracture ($k_N/k_T = 1$) can be discriminated from a wet fracture ($k_N/k_T = 0$).

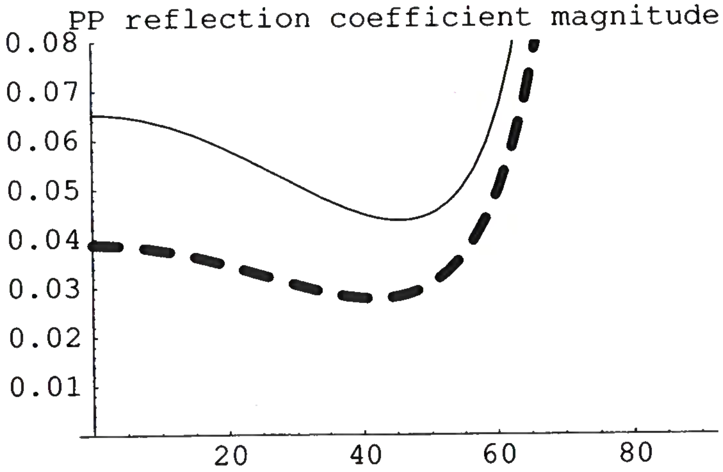

Figure E.2. The linearized reflection coefficient as a function of angle (thick, dashed line) for a welded interface (k_T, k_N = 0) and the exact reflection coefficient for an interface with the same elastic contrasts, but with some slip ($k_T = 5.0 \times 10^{-10}$ m/Pa and $k_N = 2.5 \times 10^{-10}$ m/Pa). By not including slip in linearized reflection coefficient, it underestimates the magnitude of the exact reflection coefficient.

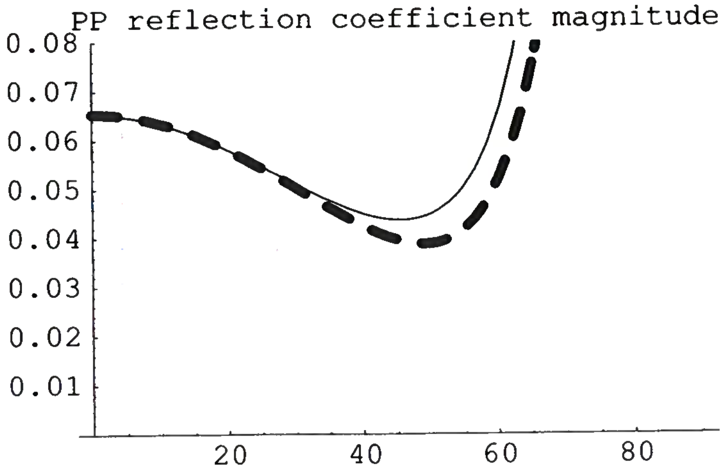

Figure E.3. The linearized reflection coefficient as a function of angle (thick, dashed line) for an interface with the elastic contrasts from Table I and having linear-slip behavior ($k_T = 5.0 \times 10^{-10}$ m/Pa and $k_N = 2.5 \times 10^{-10}$ m/Pa). The expression for the linearized reflection coefficient including slip is taken from equation (E.6). The exact reflection coefficient for the same interface is also shown. By including slip in the linearized reflection coefficient, the approximation agrees well with the exact solution up to about 45°.